ALMA MATER STUDIORUM - UNIVERSITÀ DI BOLOGNA

SECONDA FACOLTA' DI INGEGNERIA
CON SEDE A CESENA

CORSO DI LAUREA

IN INGEGNERIA AEROSPAZIALE
Classe 8197

Sede di Forlì

TESI DI LAUREA

In Strutture e Materiali Aerospaziali LM

Structural design, manufacturing and testing of a new wing for the CSIR's Modular UAS in composite materials

CANDIDATO

Francesco Perini

RELATORE

Ing. Enrico Troiani

CONTRORELATORE

Ing. Gerardus Janszen

CSIR SUPERVISOR

Ing. John Monk

Anno Accademico 2011/2012

Sessione II

"...does anyone have a hammer?"
J.C.

Abstract

The purpose of this work was to design, manufacture and test a new optimized wing structure for the CSIR's Modular UAS. It was needed to increase the current wing span from 4 m to 6, maintaining the weight of the half wing below 4.5 kg. The project started studying the flight envelope of the Modular UAS with its possible load critical conditions (following the regulations RAI-V.EL) using Matlab as calculation platform. XFLR5 was later used to further verify the mathematical result of the critical load study. Then, carbon fiber laminate were studied and tested in order to identify the best layup configuration to resist the ultimate loads. A primary concept of the wing structure was generated with Rhinoceros 4.0 and analyzed with the semi-monocoque theory. The results were corrected with the FEM analysis using MSC Patran/Nastran2010 and the displacement at the tip, under the loads, was predicted. The wing was manufactured completely in the CSIR's UAV Lab in several phases, then assembled. The structural static test was carried out with the whiffletree in the UAV Lab, and the wing was successfully tested to 6.7 g so far. Eventually, the new wing was ready to be painted and prepared, with servos, to be mounted on the Modular UAS.

Contents

List of Figures

List of Tables

Chapter 1

Introduction

1.1 Introduction

Combination of different materials which result in superior products started in antiquity and has been in continuous use down to the present day. Even if a general recognized statement of composite material doesn't exist yet, it can be simply defined as a material consisting of several parts, or constituents. At the atomic level, materials such as certain metal alloys and polymeric materials could be said composite materials since they are made up of different and distinct groups of atoms. Structurally (from 10^{-4} cm to 10^{-2} cm) a metallic alloy as a low carbon steel containing ferrite and perlite may be defined as composite, since the ferrite and perlite are distinctly identifiable microscopically constituents. At a macro-structural level (10^{-2} cm or more) a plastic material reinforced with glass fibers, in which the fibers themselves can be separately identified, could be considered a composite. It is clear that the difficulty in defining a composite material consists in the limitations on the size that one requires for the constituents that make up the material.
For the purpose of this discussion, the composite definition is as follows: a *composite material* is a material composed from a mixture or combination of two or more micro or macro constituents which differ in form and composition, essentially insoluble in each other. The importance of a composite material technology lies in the fact that two or more distinct materials are combined together to form a material that has the best properties, or somehow significant, compared to the properties of the constituents, and the choice of technological process and training are crucial to get parameters of resistance, cost and production speed desired.
For this reason, and for the importance of saving weight through the use of high performance materials, the military and civil aeronautical industry

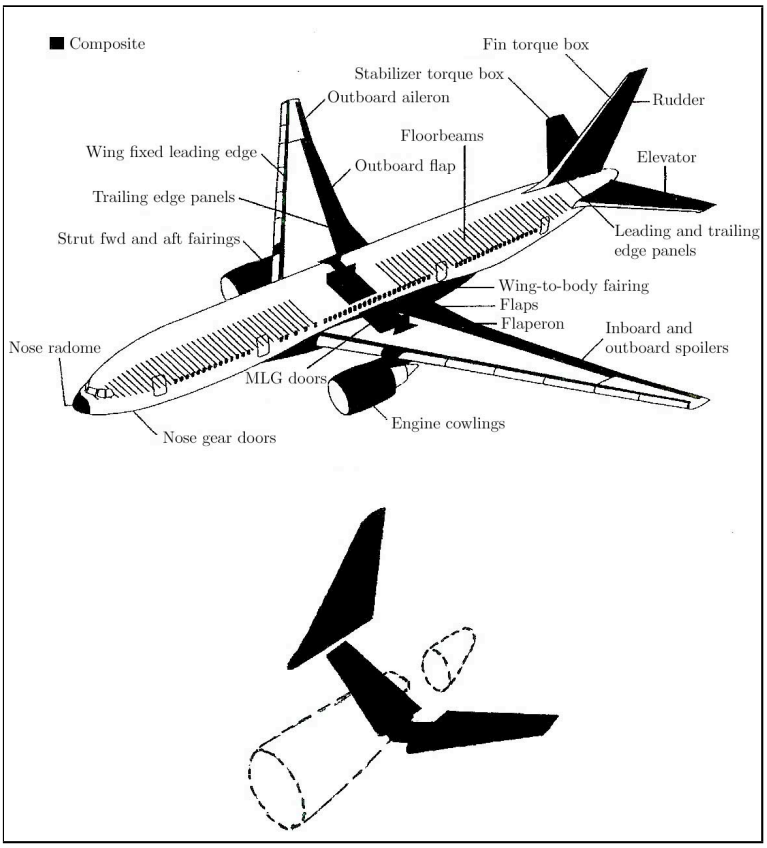

Figure 1.1 – *Boeing 777 composite parts [9].*

has been interested in development of these materials since the beginning [9].

1.2 Use of composite in aviation

Caution regarding the use of composite materials, however, was justified by the expectation of the experimental results of flight of new aircrafts both in terms of fatigue resistance, both in relation to atmospheric agents such as humidity, rain and lightning. The impulse for the massive spread of high-strength fibers in the field of commercial aviation came from an irreversible increase in the cost of oil which imposed the need to achieve a significant reduction in fuel consumption. The beginning of 1980s marked

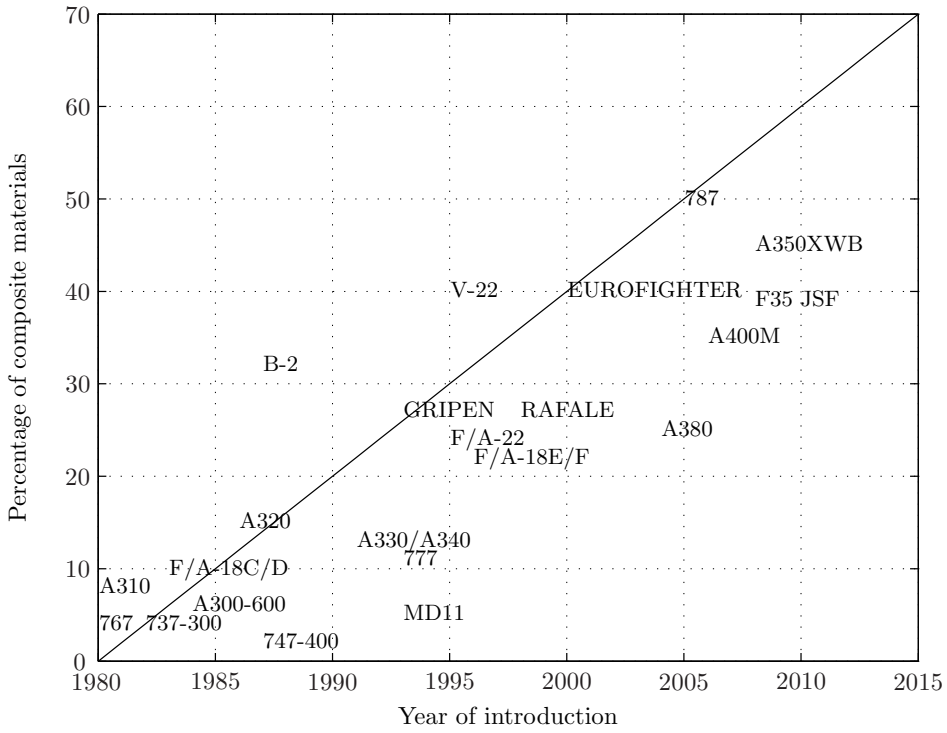

Figure 1.2 – *Percentage of composite materials in civil and military aviation.*

the entry into service of civil aircraft that incorporated significant amounts of advanced composite materials also in significant structural parts, as it was for example for the *Boeing 767*, which had all the movable surfaces of the wing and rudder made in this way, and for the next evolutionary version *777* (Figure 1.1). In Italy, the civil aircraft *ATR 42* for regional transport, was built with similar criteria. Military aircrafts such as the *AV-8B Harrier II* have wings made entirely of composite. Composites are today increasingly widespread use, with an increase of use faster in the military, as can be seen from Figure 1.2. Looking at the constructive level, it has to be said that for non-structural applications are used aramid and glass, while for structurally critical components such as movable control surfaces and vertical empennage, carbon is preferred. The weight savings achieved hovers around 25 percent, a remarkable value if one considers that in a commercial aircraft, each kilogram spared allows, during 15 years of operating life of the plane itself, a lower fuel consumption of 3200 liters. It is natural to wonder then why the technology of advanced composite materials hasn't been extended in the past to primary structures such as fuselage and wing body [10]. Such reticence is motivated by the fact that,

being quite recent, composites still lacked an exhaustive database on their secondary characteristics and variation of their strength over the years. Accurate studies were carried out on bonding between fiber and matrix, essential base for proper stress distribution, while it generated still concerns the gradual increase of fragility of the matrix due to moisture absorption and prolonged contact with hydrocarbon vapors. The gap between military and commercial sector has been definitely considerable: in 2000 a military aircraft was formed by 50% of advanced composite material, by 30-40% of aluminum alloys and for the remaining part of titanium and steel, while the share of fibers in the structure of a commercial airliner did not exceed the 25-30%; a beautiful specimen of airframe built almost entirely of composite materials is the *Voyager*, the lightweight experimental plane that in Dec '86 was the first non-stop flight around the world in aviation history, 43000 miles without refueling, in nine days of flight. This aircraft is capable of carrying up to 5 times its own weight of 900 kg and is equipped with 17 tanks which feed two engines of 110 HP each, able to ensure a cruising speed of 200 km/h. The most striking example, recently built, a symbol of effective large-scale distribution of these innovative materials, is the *Boeing 787 Dreamliner*, the first airliner to be made in carbon fiber (at 50%) [19]. The novelty lies in the fact that the fuselage is entirely made of graphite fiber with titanium parts to reinforce the structure. The use of this material is allowed to save about 15-20% of weight compared to a traditional aircraft of equal dimension, in aluminum alloy. Also the deterioration of the fuselage, usually due to corrosion, is considerably lower than alloy aircrafts, which it is translated to the airliner in high maintenance savings, both ordinary and extraordinary. Thanks to high resistance ensured by carbon fiber, it has been possible to raise the internal pressure, leading to a cabin altitude of 1800 meters above sea level, compared to 2400 meters of a traditional aircraft, thereby increasing the comfort for passengers. In addition, it was possible to increase the humidity, arriving at 15% providing better livableness, especially in long distance. The carbon composite is not a good conductor, and for this reason it creates the problem of isolating the area from electrocution. To do this it is needed to install, in the outermost layer of the fuselage, a layer of copper fibers in order to achieve a Faraday cage. An additional and special feature is the production process: the "skin" of the fuselage is manufactured in only five pieces (called one piece barrel) then joined together; a normal aluminum plane, however, is assembled into many pieces. The decrease of weight, jointed to an excellent aerodynamics and new engines, allows the Boeing 787 high fuel savings compared to a conventional airliner in aluminum alloy, which is why the major companies have chosen, for the renewal of its fleet, the 787 [19]. On the same line of Boeing, the European

Airbus started few years ago to design their new *A350* in order to not remain behind in the airplanes market in terms of fuel efficiency and operating costs. Advanced composite materials are also widely used in space field, with a few limitations due to the environmental conditions in which they must operate. If current construction trends remain unchanged, it is expected in the coming years that these materials will almost completely replace the metal alloys as well as in the '30s these replaced wood [9].

1.3 CSIR - Defence, Peace, Safety and Security

The *Council for Scientific and Industrial Research* (*CSIR*) is South Africa's central and premier scientific research and development organization. It was established by an act of parliament in 1945 and is situated on its own campus in the city of Pretoria. It is the largest research and development (R&D) organization in Africa and accounts for about 10% of the entire African R&D budget. It has a staff of approximately 3000 technical and scientific researchers, often working in multi-disciplinary teams. At the CSIR, science and technology (S&T) is hard at work for a peaceful, safe and prosperous South Africa. The organisation has developed strong S&T capabilities through its associations with key players in defence, safety and security-related fields, thereby also contributing to the country's international competitiveness. The CSIR - through its expertise in defence, peace, safety and security - serves as the 'in-house' S&T capability of key government departments and agencies in defence, peace, safety and security. CSIR Defence, Peace, Safety and Security provides a national defence S&T capability: supplying knowledge, advice and solutions in defence and matters of national security. Specifically, it aims to provide a defence evaluation and research institute capability for the *Department of Defense*. CSIR Defence, Peace, Safety and Security also:

- partners with the local defence and aerospace industries to improve strategic capabilities and international competitiveness;

- collaborates and undertakes joint projects with selected international and local organizations and laboratories;

- develops and maintains national research facilities and infrastructure;

- contributes to national science, engineering and technology themes,

industry development initiatives and to a new generation of scientists and engineers in the defense, aerospace and security fields;

- contributes to an improved understanding of crime, violence and conflict through the application of innovative S&T solutions.

The CSIR's expertise in the defence, peace, safety and security domain covers numerous areas, with focused research groupings contributing to these areas like:

- Aeronautic Systems;
- Landwards Sciences;
- Optronic Sensor Systems;
- Radar and Electronic Warfare Systems;
- Command, Control and Information Warfare;
- Technology for Special Operation.

In particular *Aeronautic Systems Competency* (*ASC*), a competency area within *DPSS*, includes the aerostructures research group, led by John Monk, and consists of engineers and scientists with a diverse range of skills. The core areas of expertise of the group are in aero-elasticity (flutter prediction technologies), aircraft and mission modelling and simulation, non-destructive technology (NDT) research, vibration measurement, helicopter-related technologies, structures-related technologies and unmanned aerial systems design and development [20].

1.4 Internship at the CSIR - Structural design of a UAS wing

The ASC provides aeronautical services to the industry at large and particularly supports the research requirements of the Department of Defence (*DoD*). ASC has, in the past, developed a number of prototype airframes ranging from small unmanned aircraft systems (UAS) up to an all carbon fibre turboprop military trainer. Currently ASC has a number of research UAS, the largest of these being a 4 meters span airframe called the Modular UAS (MUAS). A longer duration version of the MUAS is required and a

new wing has been aerodynamically designed. The goal for this internship, in general, is to design an optimised wing structure for the new wing, assist in the manufacture and conduct the structural testing of the wing in the CSIR test rig. The following tasks have been assigned:

- predict the maximum expected loads at the edge of the flight envelope;
- develop an optimised composite lay-up scheme for the new wing that is structurally capable of withstanding the predicted aerodynamic loads;
- predict the bending and torsional stiffness;
- assist with the manufacture of the wing from wing moulds;
- develop and conduct the structural testing program.

The idea was to split this project in six phases, i.e.:

1. study and choose composite materials and manufacturing processes;
2. determine the flight envelope and calculate the maximum loads;
3. compare some wing structural solution using a primary design approach;
4. develop FEM optimization of the wing structure chosen with composite material;
5. follow the manufacturing process of the new wing in composite material;
6. conduct the structural testing programme.

Chapter 2

Flight condition and loads of the Modular UAS

2.1 The CSIR's Modular UAS

2.1.1 Introduction

The *Modular UAS* was developed with funding from the *Department of Science and Technology* (DST) and has been made available as a UAV test bed to be used by researchers, universities and other tertiary educational institutions. There are currently eleven research projects at four tertiary educational institutes under way directly related to the current system.The design was conceptualised with a number of the potential research topics in mind including those of autopilot algorithm development, detect and avoid technologies, non-linear flight control, variable stability, structural optimisation, piezoelectric actuators. Even a solar powered configuration has been considered during the design process. A modular design concept was chosen to allow for changes to wing span and to fuselage length and number to be easily made, altering the UAV's performance and handling characteristics to suit specific research payloads. Each of the two fuselages is capable of being functionally independent of each other, each consisting of brushless electric motors, speed controllers, batteries and flight control systems. Redundancy in the flight controls and propulsion systems is envisaged to enable longer term research on reconfigurable autopilots [John Monk].

Figure 2.1 – *The CSIR's Modular UAS in the current configuration (photo courtesy of John Monk).*

With funding from the CSIR the *Stellenbosch University's Engineering Systems Laboratory* has further developed their autopilot technology previously developed for the CSIR *Sekwa* variable stability mini-UAV [John Monk].

MODULAR UAS PERFORMANCE SPECIFICATIONS	
Wing span $[m]$	4.0
Payload capability $[Kg]$	10.0
Stall speed $[m/s]$	15.0
Dive speed $[m/s]$	33.4
Engine power $[kW]$	6.0
Endurance $[min]$	45.0
Flight duration (reduced payload) $[min]$	90.0

Table 2.1 – *Modular UAS performance specifications (data courtesy of John Monk).*

2.1.2 The task of the new Modular UAS configuration

A new version of the Modular UAS is required for boarder safety guarding. Thus the task for the new project is basically an extended endurance version of the Modular UAS to 8 hours operating. To obtain this the Rerearch Group of John Monk has designed a new wing geometry, 6 m span, in order to:

- carry 10 kg more fuel (petrol, diesel or fuel cells) in order to recharge the batteries with two small combustion engines during the flight;
- have an higher aerodynamic efficiency E.

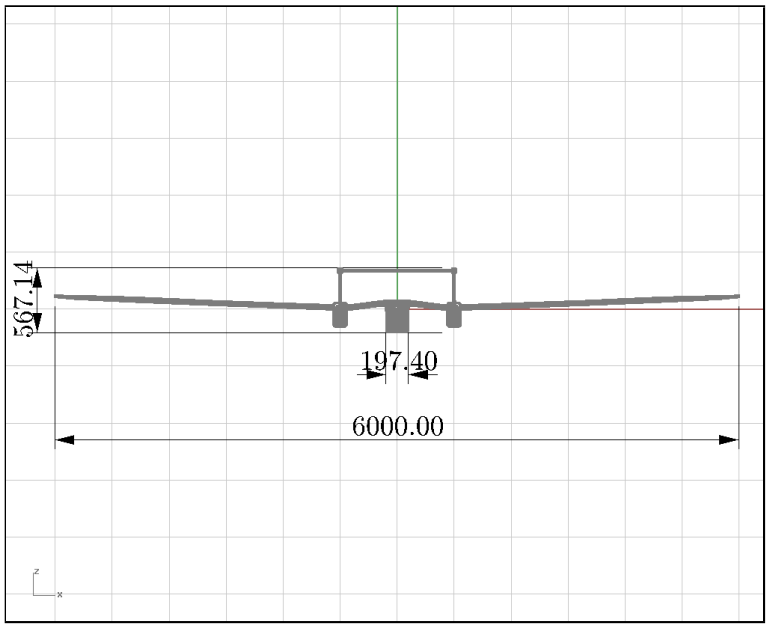

Figure 2.2 – *Front view of the CSIR's Modular UAS (dimensions in millimeters).*

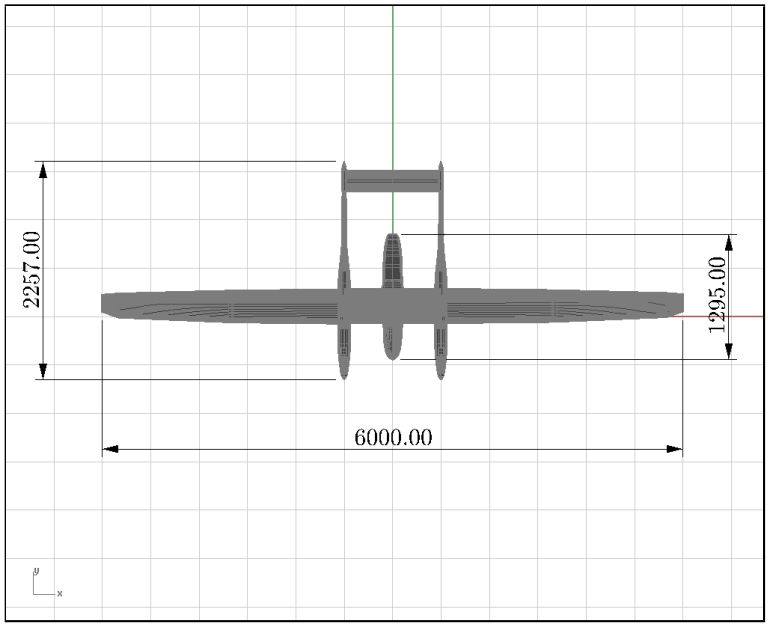

Figure 2.3 – *Top view of the CSIR's Modular UAS (dimensions in millimeters).*

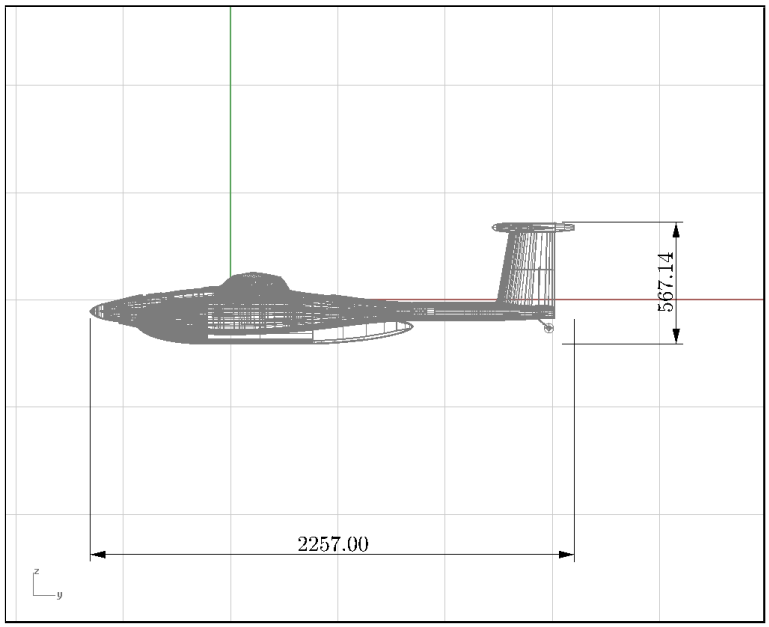

Figure 2.4 – *Side view of the CSIR's Modular UAS (dimensions in millimeters).*

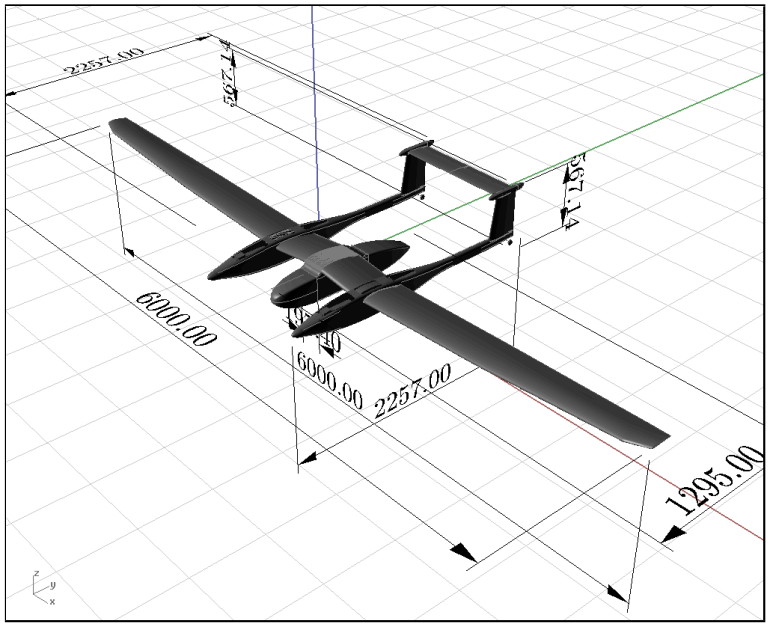

Figure 2.5 – *ISO view of the CSIR's Modular UAS (dimensions in millimeters).*

A CAD (courtesy of Neall Moore) preview of the new version of the Modular UAS is shown above, with the dimensions expressed in millimeters.

2.2 The V-n diagram of the Modular UAS

In order to define the final configuration of the airplane, the applied loads during its operational life i.e. flight and ground conditions, need to be known. It is not feasible to get all the real load conditions that an airplane could meet, so it is common practice to investigate only those cases that the experience has shown as critical [16]. The design of an airplane is a result of successive approximations and performing comparisons with different configurations; the same principle is also applied to the study of loads on the aircraft, starting with simple theoretical considerations to get, by approximations, the actual loading condition with the aid of experimental tests.

2.2.1 Load factor diagram

An airplane has three limits over which its safety is not guaranteed i.e. the aerodynamic limit given by the maximum lift coefficient $C_{L_{max}}$, the structural limit given by maximum load factor n_{max}, and the aeroelastic limit given by the maximum speed V_{max}. These three limits are shown in the *load factor diagram*, where every point represents the load condition of the airplane during maneuvering at the correspondent true air speed (TAS). Within the bounds of the load factor diagram one gets the safety flight conditions specified by the designer [16]. The aerodynamic limit imposes restrictions on flight attitude with regards to the stall condition, and this limit is given by the parabola, which is defined for positive aircraft velocities [3]:

$$n = \frac{\frac{1}{2}\rho S C_{L_{max}} V^2}{W} \tag{2.1}$$

The structural limit imposes restrictions on the maneuvers such that the airplane doesn't exceed the maximum load factor specified by the designer or, more generally, by the *Federal Aviation Regulations* depending on the

class of the airplane; for the case of the Modular UAS, the acrobatic class will be considered [1]:

$$n = n_{max} = 6 \tag{2.2}$$

$$n = n_{min} = -3 \tag{2.3}$$

The aeroelastic limit imposes restrictions on the maximum speed, with regards to the flutter or others structural dynamic phenomena of the airplane [16]:

$$V = V_{max} \tag{2.4}$$

Table 2.2 below contains Modular UAS data necessary to build the load factor diagram. The data were sourced from the original design specifications of the airplane and from discussions with John Monk (Aeronautic System Competency, Research Group Leader, chief designer of Modular UAS) and Neall Moore (Aeronautic System Competency, Researcher):

AIRPLANE AND FLIGHT CONDITIONS DATA		
Air density $[kg/m^3]$	ρ	1.225
Max take-off weight $[N]$	W_{to}	490.500
Max lift coefficient	$C_{L_{max}}$	1.676
Min lift coefficient	$C_{L_{min}}$	0.400
Lift curve slope $[rad^{-1}]$	C_{L_α}	5.500
Wing span $[m]$	b	6.000
Wing surface $[m^2]$	S	1.911
Aspect ratio	AR	18.838
Mean geometric chord $[m]$	c	0.330
Osvald's coefficient	e	0.970
Wing loading $[N/m^2]$	W/S	256.672

Table 2.2 – *Airplane and flight conditions data required to define the V-n diagram.*

To start constructing the V-n diagram, it is necessary to say that the aerodynamic loads are proportional to the dynamic pressure depending on

the altitude (through the density), so this means that the equivalent airspeed *EAS* should be used instead of the *TAS*. But, if the airplane operates at low speed and height, in conditions which could be considered as *incompressible flow*, the use of the equivalent airspeed makes the diagram independent of the altitude. The diagram considers the symmetric maneuvering in normal and inverted flight; the first characteristic speed is the stall speed V_{st} when the load factor $n = 1$:

$$V_{st_+} = \sqrt{\frac{2W}{\rho S C_{L_{max}}}} = 15.81 \ m/s \tag{2.5}$$

And for the inverted flight, when the load factor $n = -1$, is given by:

$$V_{st_-} = \sqrt{\frac{2W}{\rho S C_{L_{min}}}} = 32.37 \ m/s \tag{2.6}$$

The *maneuvering speed*, denoted V_A, represents the maximum velocity at which the airplane can perform a maneuver, without compromising the structural safety of the airplane. This is an interesting velocity for fighter pilots because flying at speeds less then V_A it is not possible to structurally damage the airplane due to generation of load factor less than n_{max} [3]:

$$V_A = \sqrt{\frac{2n_{max}W}{\rho S C_{L_{max}}}} = V_{st_+}\sqrt{n_{max}} = 38.74 \ m/s \tag{2.7}$$

And for the maximum negative g:

$$V_G = \sqrt{\frac{2n_{min}W}{\rho S C_{L_{min}}}} = V_{st_-}\sqrt{n_{min}} = 56.06 \ m/s \tag{2.8}$$

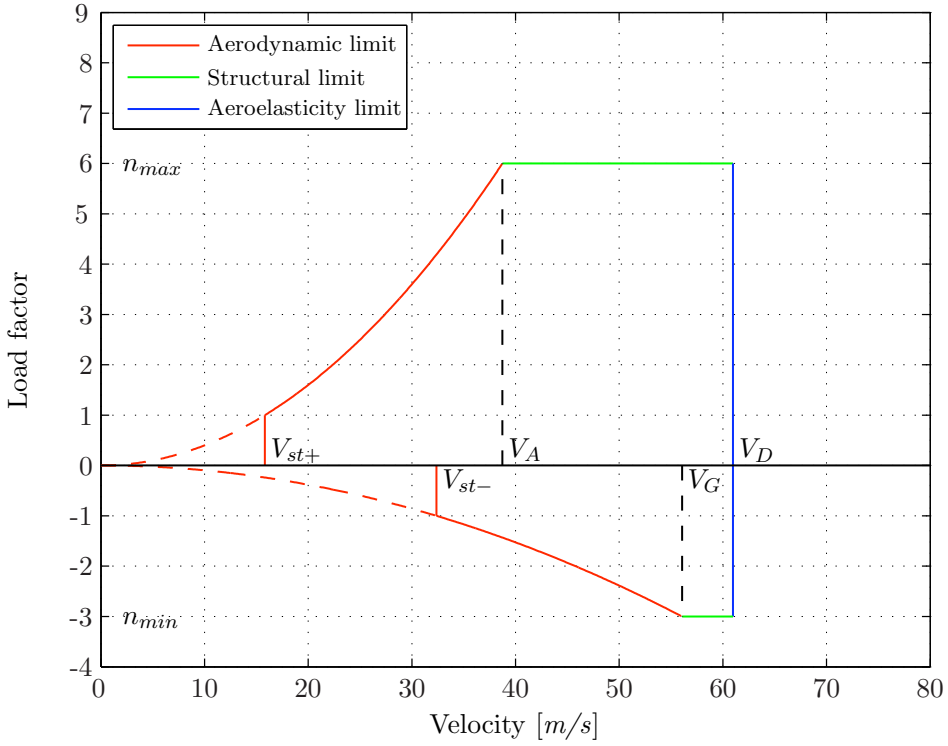

Figure 2.6 – *V-n diagram for maneuvering limits.*

The other two characteristic speeds are the *cruise speed* V_C and the *dive speed* V_D, both taken from the *FAR Part 23* as a function of the wing loading [1], paying attention to the fact that the *Federal Aviation Resulations* are written using British Imperial units:

$$V_C = 33\sqrt{\frac{W}{S}} = 39.34 \ m/s \tag{2.9}$$

$$V_D = 1.55 V_C = 60.98 \ m/s \tag{2.10}$$

As said before, speeds above the dive speed may result in structural damage, or failure, or disintegration of the aircraft due to destructive phenomena such as flutter, aileron reversal and wing divergence. The dive speed is usually greater than the maximum speed, which is obviously much higher than the cruise speed. As result of Matlab calculations, available in Appendix A,

a plot of the velocity and the load factor is showed in Figure 2.6, indicating every characteristic speed.

2.2.2 Wind gust diagram

The *wind gust diagram* corrects the load factor diagram, because it takes into account the possibility of external actions (wind gusts) which can increase the stress condition acting on the aircraft. The wind gusts are movements of ascending air, perpendicular to the ground, which change the incidence and the relative speed of the aircraft. Changing the lift causes additional loading, called gust loads, and this can be seen as an increase of the load factor; for this reason it is necessary to define a new field of safety, represented by the wind gust diagram. The variation of the angle of attack, in the case of perpendicular gusting is given by:

$$\Delta\alpha = \tan^{-1}\left(\frac{V_g}{V}\right) \cong \frac{V_g}{V} \tag{2.11}$$

And the variation of lift is given by:

$$\Delta L = \frac{1}{2}\rho S \frac{\partial C_L}{\partial \alpha}\Delta\alpha V^2 \tag{2.12}$$

The change in lift will create a change in load factor expressed by:

$$n = \frac{L + \Delta L}{W} = 1 + \frac{\frac{1}{2}\rho S \frac{\partial C_L}{\partial \alpha}\frac{V_g}{V}V^2}{W} = 1 + k_g\left(\frac{\frac{1}{2}\rho S C_{L_\alpha} V_g V}{W}\right) \tag{2.13}$$

which considers a corrective factor k_g called the *gust alleviation factor*. This factor is always less than 1 and takes into account some effects such as the inertia of the aircraft and a gradual rather than an instantaneous gusting. To define it, it is first necessary to express the term *airplane mass ratio* [16]:

$$\mu_g = \frac{2W}{\rho \bar{c} S C_{L_\alpha} g} = 23.54 \tag{2.14}$$

and the corrective factor results [16]:

$$k_g = \frac{0.88\mu_g}{5.3 + \mu_g} = 0.72 \tag{2.15}$$

Running the Matlab code for equation 2.13, considering $V_g = 50ft/s$ for the cruise speed V_C and $V_g = 25ft/s$ for the dive speed V_D[1], the wind gust load diagram results:

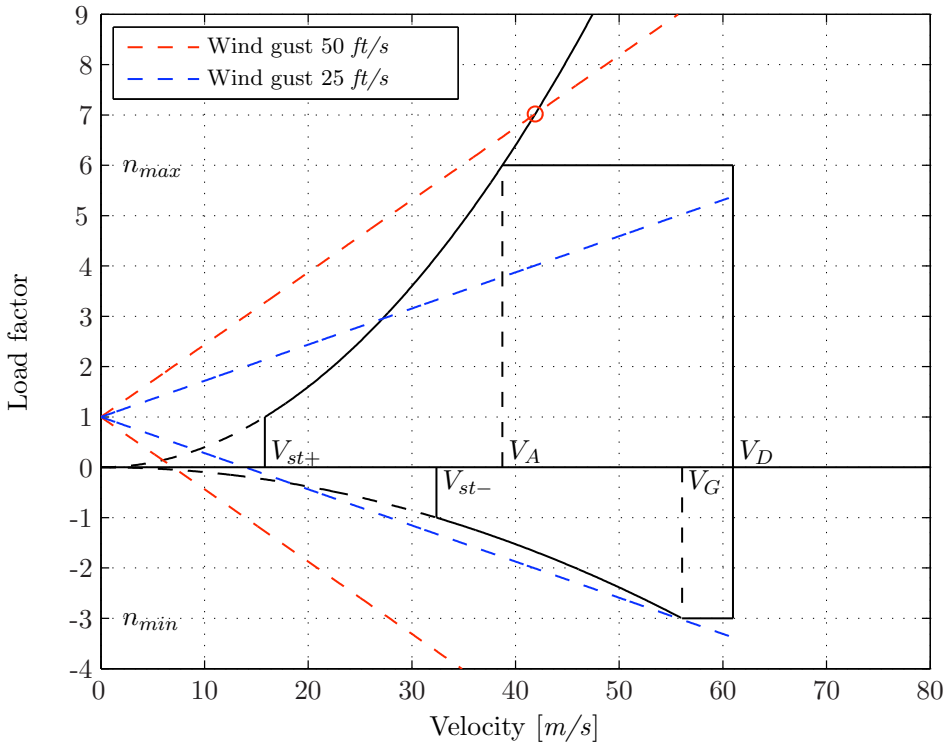

Figure 2.7 – *V-n diagram for gust loads.*

2.2.3 Complete flight envelope diagram

The *complete flight envelope diagram*, also called *V-n diagram*, is built by superimposing the maneuvering diagram and the wind gust diagram [3]. This diagram is used to delineate the proper field in which the accordingly

Modular UAS can fly to design the structure. The characteristic data emerging from this diagram are used for the next step of the load determination, as shown below:

DATA	VELOCITY $[m/s]$	LOAD FACTOR	LIFT $[N]$
V_{st_+}	15.81	1.00	490.5
V_{st_-}	32.37	−1.00	−490.5
V_A	38.74	6.00	2943.0
V_C	41.89	7.02	3443.31
V_D	60.98	6.00	2943.0
V_G	56.06	−3.00	−1471.5

Table 2.3 – *Characteristic data emerging from the complete V-n diagram running the MATLAB code available in Appendix A.*

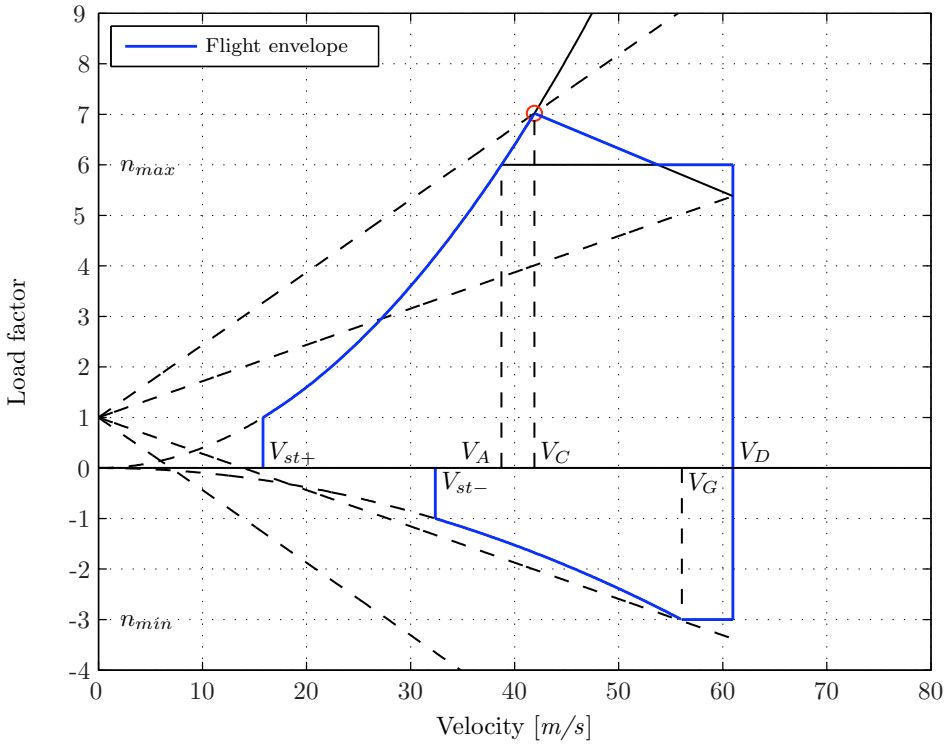

Figure 2.8 – *Complete flight envelope for the aircraft Modular UAS.*

2.2.4 Critical load condition from the V-n diagram

For the first design of the wing structure lift and weight are considered as the only loads acting on the wing itself. The weight is directed in the opposite direction of the lift so it relieves the resistant structure of a part of the load, so don't consider it could be too much conservative, getting an oversized structure. The condition in which the lift is calculated is the most critical, identified by the complete flight envelope diagram of the Modular UAS in Figure **??** considering the point highlighted by the red circle, which is the maximum load condition:

$$V_C = 41.89 \ m/s \tag{2.16}$$

$$n_{max} = 7.02 \tag{2.17}$$

$$L = \frac{1}{2}\rho S C_{L_{max}} V_C^2 n_{max} = 3443.31 \ N \tag{2.18}$$

This data will be used as comparison with the XFLR5 simulations in the next chapter, necessary to get the applied load on the wing structure in terms of shear force, bending moment and torque moment.

Chapter 3

Wing geometry and loads

3.1 Modular UAS's wing geometry

The wing geometry data shown in Table 3.1 has been kindly provided by John Monk and has been used to design the CAD of the wing and for the analysis with XFLR5 to get the lift distribution on the wing itself:

WING GEOMETRY DATA		
Airfoil [%]	SD7062	14.000
Wing span $[m]$	b	6.000
Wing surface $[m^2]$	S	1.911
Aspect ratio	AR	18.838
Root chord $[m]$	c_r	0.360
Tip chord $[m]$	c_t	0.160
Taper ratio	λ	0.444
Mean aerodynamic chord $[m]$	MAC	0.324
Mean geometric chord $[m]$	c	0.330
Quarter chord sweep [°]	Λ	1.720
Dihedral angle [°]	Γ	2.000

Table 3.1 – *Wing geometry data kindly provided by John Monk.*

The CAD of the wing shown in the following pictures has been generated with the software Rhinoceros 4.0 using the geometry listed in Table 3.1 following the specifications of John Monk, in particular keeping the top surface of the spar straight, to get a simpler and more precise handmade building phase. The dihedral angle is given at the wing junction with the fuselage,

so the mold manufacturer Lightweight Structures Technology L.t.d., based in Pretoria doesn't need to consider the dihedral angle of the wing.

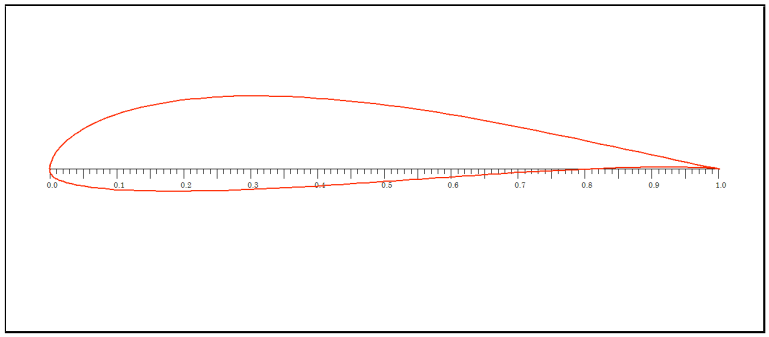

Figure 3.1 – *SD7062 14% profile used for the Modular UAS's new wing.*

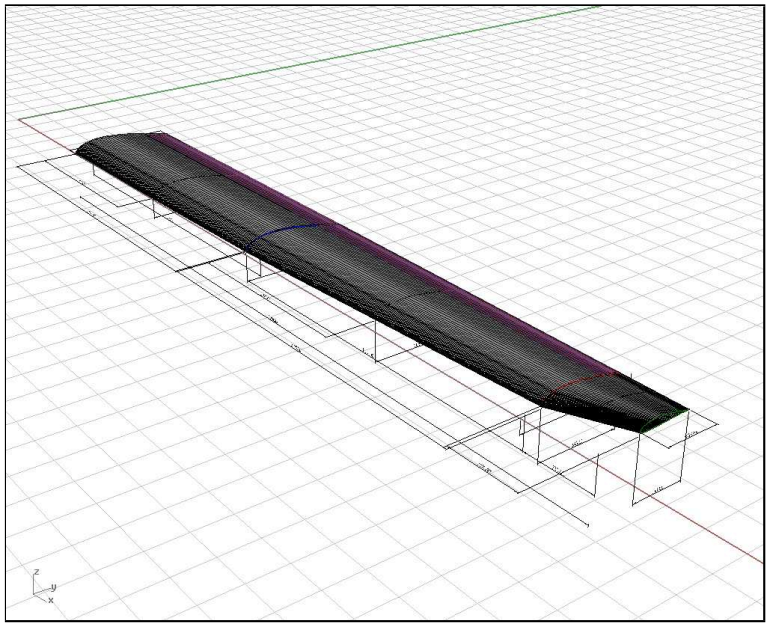

Figure 3.2 – *View generated with Rhinoceros 4.0 (dimensions in millimeters).*

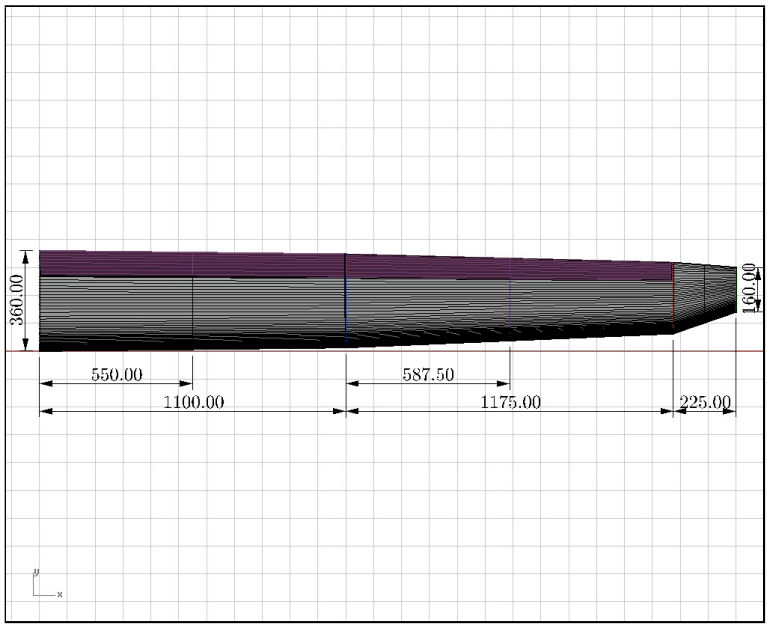

Figure 3.3 – *Top view generated with Rhinoceros 4.0 (dimensions in millimeters).*

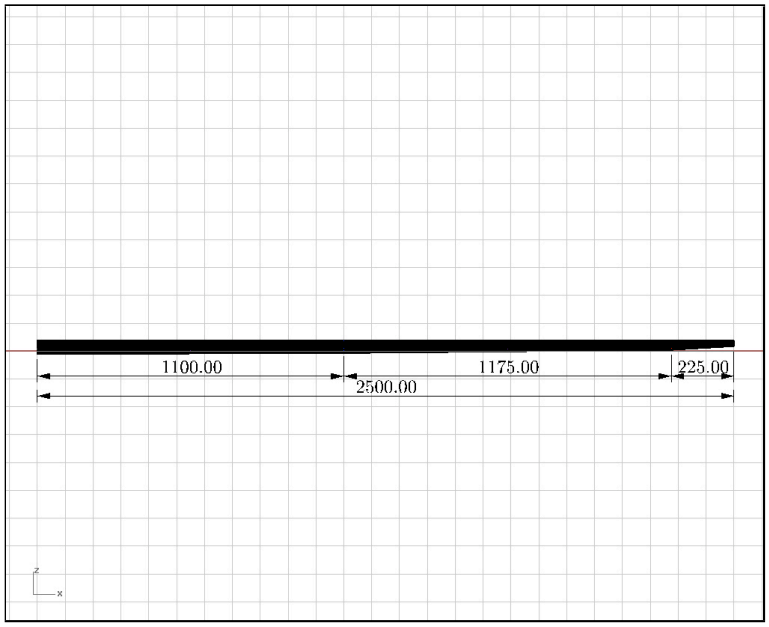

Figure 3.4 – *Front view generated with Rhinoceros 4.0 (dimensions in millimeters).*

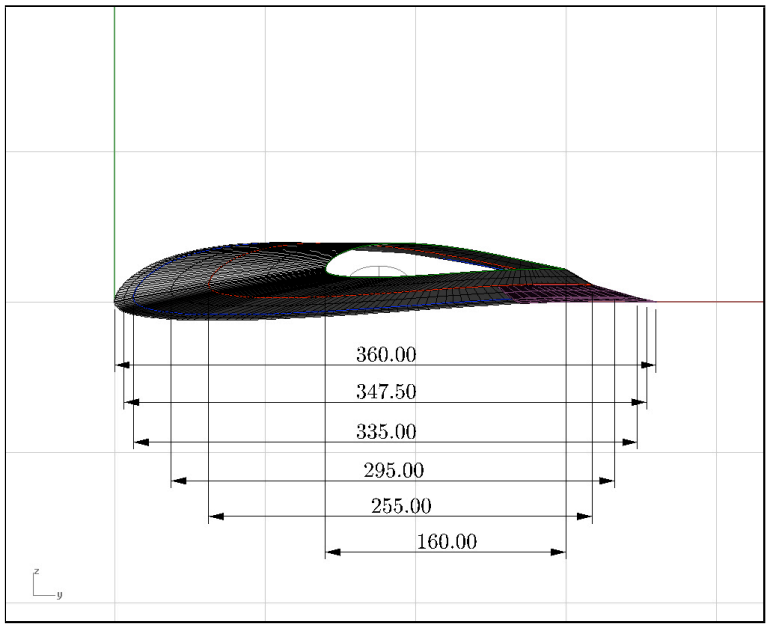

Figure 3.5 – *Right view generated with Rhinoceros 4.0 (dimensions in millimeters).*

3.2 Aileron and flap design

3.2.1 Introduction

The wing trailing edge in a conventional aircraft is the location for two control surfaces; one primary (i.e. aileron), and one secondary (i.e. trailing edge high lift device such as flap). As the aileron and the flap are next to each other along the wing trailing edge, they impose a span limit to each other. The balance between aileron span b_a and flap span b_f is a function of the priority of roll control over the take-off/landing performance. To improve the roll control power, the ailerons are to be placed on the outboard and the flap on the inboard part of the wing sections. The application of high lift device applies another constraint on the aileron design which must be dealt with in the aircraft design process [3].

3.2.2 Aileron effectiveness verification

Following the regulation *Standard RAI-V.EL*, the aircraft must achieve a bank angle from -30° to 30° in less than 4 seconds at V_{app} [2], defined below.

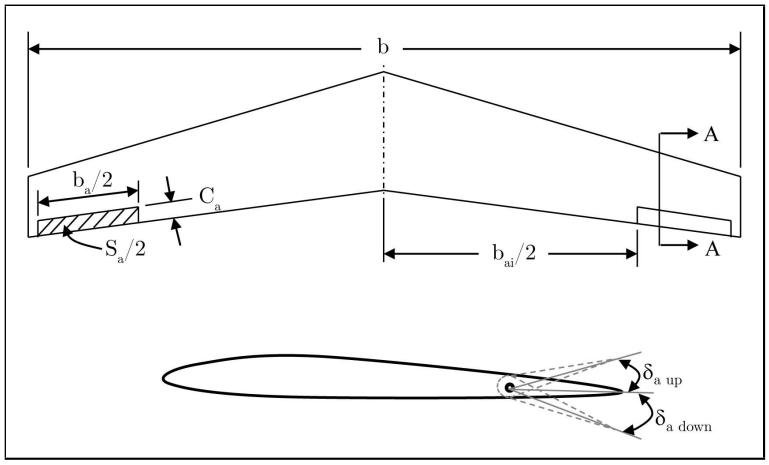

Figure 3.6 – *Top and side view of the wing and the aileron to identify the variables [3].*

Considering a simpler construction solution, the first idea is to consider the flap placement at the inboard linear section from 0 m to 1.1 m and the aileron placement at the outboard linear section from 1.1 m to 2.275 m using the root as center of the reference axis. This implies the least number of possible ribs and a straight hinge line for the control surfaces. Following the general rules, i.e. the typical values for some guideline parameters [3]:

$$\frac{S_a}{S} = \frac{0.1773}{1.91} = 0.09 \quad [0.05 - 0.1] \tag{3.1}$$

$$\frac{b_a}{b} = \frac{2.35}{6} = 0.392 \quad [0.2 - 0.3] \tag{3.2}$$

$$\frac{b_{a_i}}{b} = \frac{3.2}{6} = 0.53 \quad [0.6 - 0.8] \tag{3.3}$$

$$\frac{c_a}{c} = 0.25 \quad [0.15 - 0.25] \tag{3.4}$$

$$\delta_{a_{max}} = \pm 20^\circ \quad [\pm 30^\circ] \tag{3.5}$$

The non-dimensional control derivative $C_{L_{\delta_a}}$ is a measure of the roll control power of the aileron; it represents the change in rolling moment per unit change of aileron deflection. The larger $C_{L_{\delta_a}}$, the more effective the aileron is in creating a rolling moment. This control derivative may be calculated using the method introduced in [3]:

$$C_{L_{\delta_a}} = \frac{2C_{L_\alpha}\tau c_r}{Sb}\left[\frac{y_o^2}{2} + \frac{2}{3}\left(\frac{\lambda - 1}{b}\right)y_o^3\right]_{y_i}^{y_o} = 0.2442 \ rad^{-1} \tag{3.6}$$

where τ is the aileron effectiveness parameter and is obtained from Figure 3.7, given the ratio between aileron-chord and wing-chord. Figure 3.7 is a general representation of the control surface effectiveness:

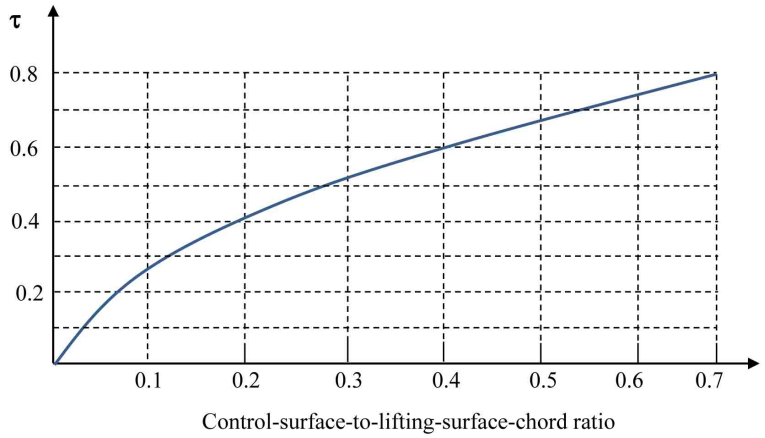

Figure 3.7 – *Control surface angle of attack effectiveness parameter [3].*

The section lift coefficient C_L on the sections containing the aileron may be written as:

$$C_L = C_{L_{\delta_a}}\delta_a = 0.08524 \tag{3.7}$$

The flight condition considered is at V_{app}, approach speed, given by the *Standard RAI-V.EL*:

$$V_{app} = 1.3V_{st_+} = 20.558 \ m/s \tag{3.8}$$

Corresponding, the rolling moment contribution of the ailerons is:

$$L_a = \frac{1}{2}\rho V_{app}^2 S C_L b = 252.75 \ Nm \tag{3.9}$$

using as drag reference center distance as 40% of the wing half span.

$$y_D = 0.4\frac{b}{2} = 1.2 \ m \tag{3.10}$$

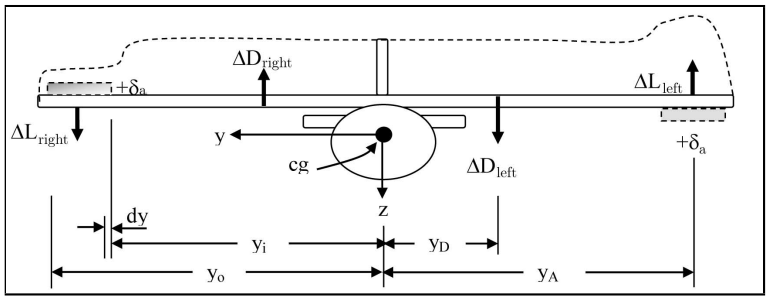

Figure 3.8 – *Incremental change in lift and drag in generating a rolling moment [3].*

Solving for the steady-state roll rate P_{ss} results in:

$$P_{ss} = \sqrt{\frac{2L_a}{\rho(S_w + S_{ht} + S_{vt})C_{D_r}y_D^3}} = 9.28 \ rad/s \tag{3.11}$$

To calculate the bank angle Φ_1 at which the aircraft achieves the steady roll rate the following equation is used:

$$\Phi_1 = \frac{I_{xx} \ln P_{ss}}{\rho(S_w + S_{ht} + S_{vt})C_{D_r}y_D^3} = 57.975 \ rad \tag{3.12}$$

It is assumed that the aircraft is initially at a level flight condition (i.e. $P_0 = 0$) and the new roll rate is the steady-state roll rate (i.e. $P_1 = P_{ss}$). Thus:

$$\dot{P} = \frac{P_{ss}^2}{2\Phi_1} = 0.743 \ rad/s^2 \tag{3.13}$$

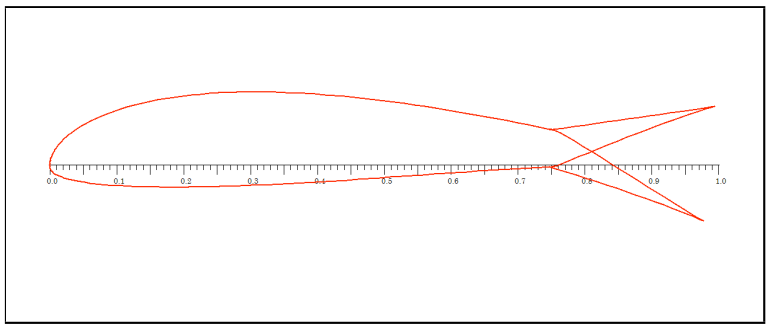

Figure 3.9 – *SD7062 14% profile with full positive and negative aileron deflection used for the Modular UAS's new wing.*

Therefore, the duration required t_{req} to achieve a desired bank angle Φ_{req} (from -30° to 30°) will be determined as follows [3]:

$$t_{req} = \sqrt{\frac{2\Phi_{req}}{\dot{P}}} = 1.6785 \ s \tag{3.14}$$

which is under the limit of the UAS italian regulation [2]. As a confirmation of the result, the method shown in [4] is also used:

$$\frac{pb}{2V} = \frac{C_{L_{\delta_a}} \tau \delta_a}{\tau 114.6 C_{L_p}} = 0.0735 \tag{3.15}$$

where C_{L_p} is taken from the graph of Perkins and Hage, pg. 357 [4] considering the AR and the taper ratio of the Modular UAS's wing.

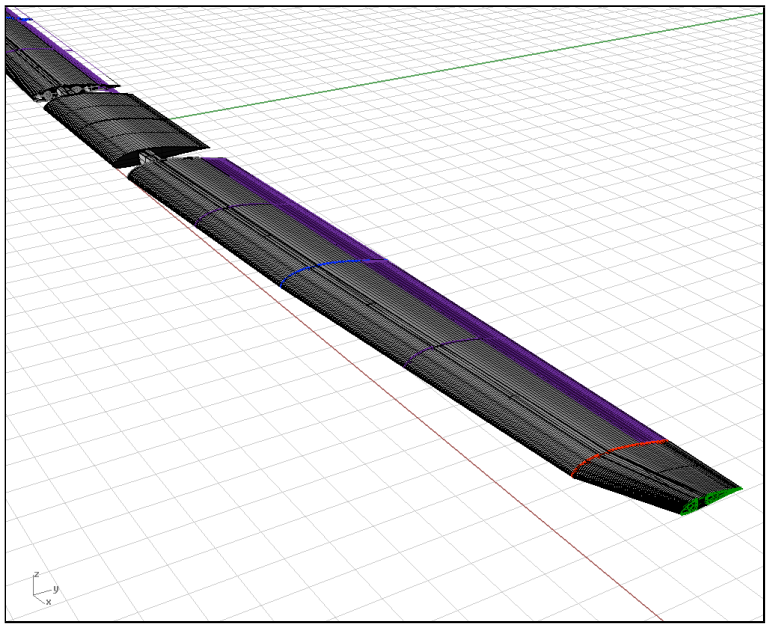

Figure 3.10 – *Modular UAS's ailerons view generated with Rhinoceros 4.0.*

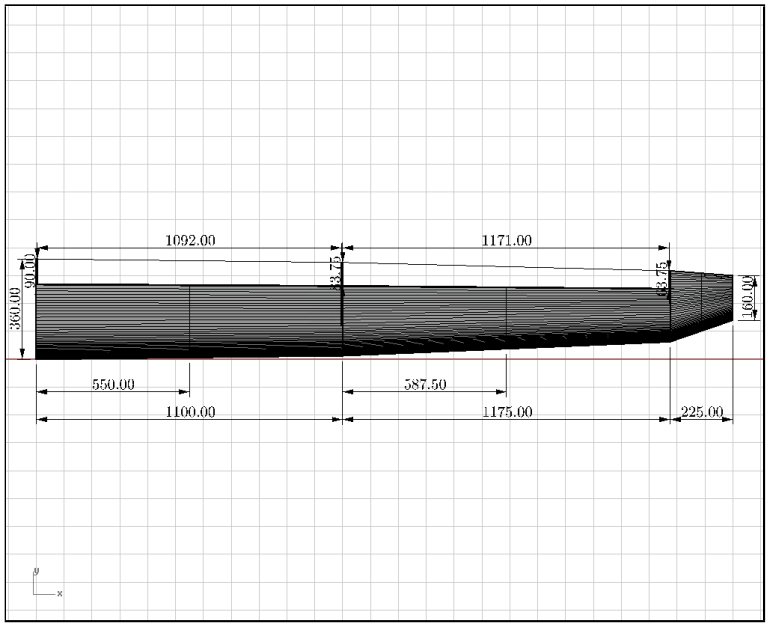

Figure 3.11 – *Top view generated with Rhinoceros 4.0 (dimensions in millimeters).*

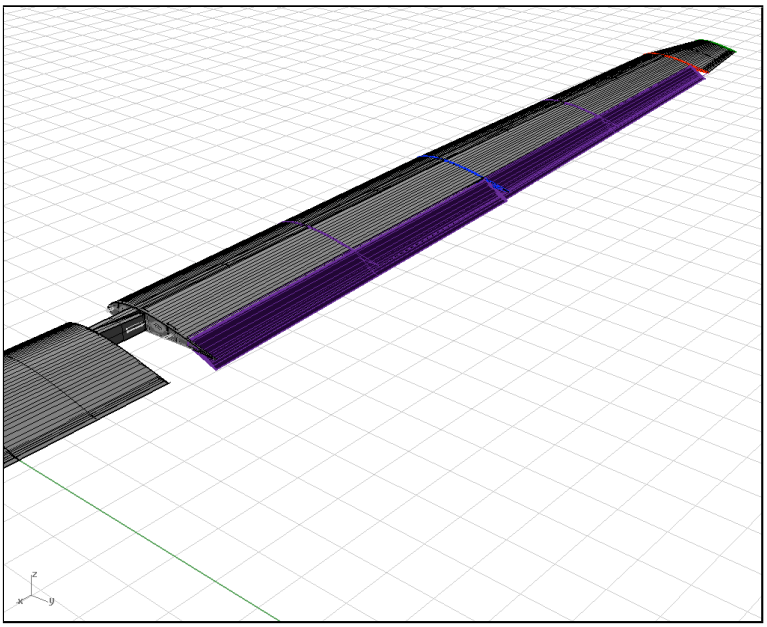

Figure 3.12 – *Modular UAS's ailerons back view generated with Rhinoceros 4.0.*

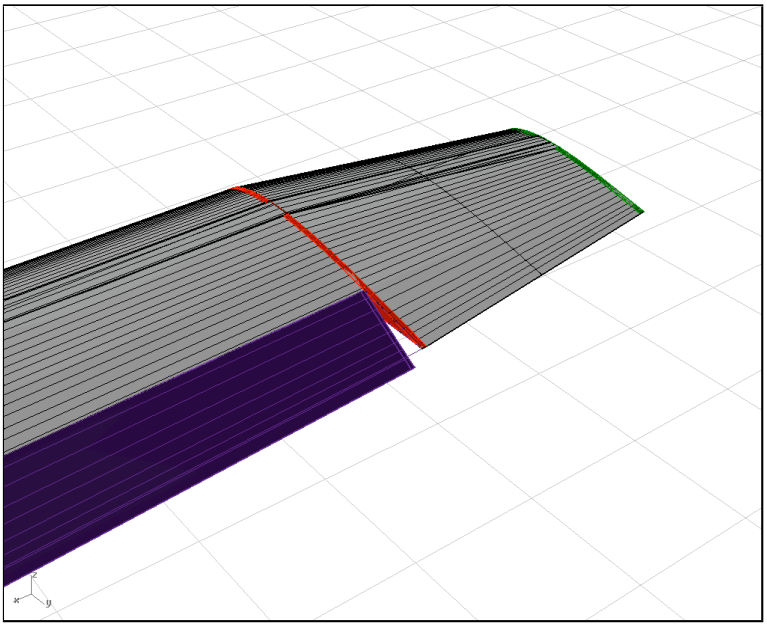

Figure 3.13 – *Modular UAS's ailerons zoomed view generated with Rhinoceros 4.0.*

As a comparison two different cases, i.e. the cargo and bombardment types and the fighter types, are shown:

$$\begin{aligned} \frac{pb}{2V} &= 0.07 \quad [cargo] \\ \frac{pb}{2V} &= 0.09 \quad [fighter] \end{aligned} \tag{3.16}$$

which confirms the previous result in the equation 3.15. The airfoil and the size of the ailerons can now be shown within the wing CAD in Figure 3.10

3.2.3 Flap effectiveness verification

The spanwise extent of the aileron depends on the amount of span required for the trailing edge high lift devices. In general, the outer limit of the flap is at the spanwise station where the aileron begins. The exact span needed for the ailerons primarily depends on the roll control requirements. A low speed aircraft usually utilizes about 40% of the total wing semispan for ailerons. This means that flaps can start at the side of the fuselage and extend to the 60% semispan station. However, with the application of spoilers, the ailerons are generally reduced in size, and the flaps may extend to about 75% of the wing semi-span. Furthermore, if a small inboard aileron is provided for gentle maneuvers, the effective span of the flaps is reduced [3]. In this case, considering the flap already placed in the central wing, the total extension of the flap will be 47%. The change must be verified in terms of V_{st_+}. An initial analysis is made with XFLR5 on the airfoil with the new $C_{l_{max}}$ given by the flap with the maximum extension of 20° down. The simplest flap, i.e. the plain flap, has been considered.

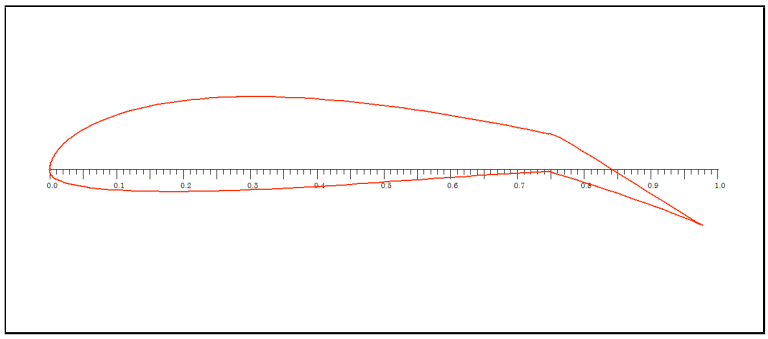

Figure 3.14 – *SD7062 14% profile with flap used for the Modular UAS's new wing.*

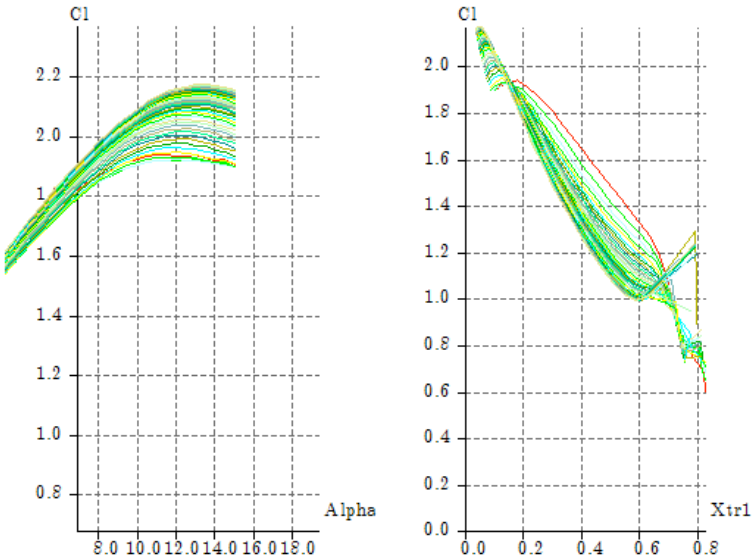

Figure 3.15 – *C_l/α and $C_l/Xtrl$ graph of the SD7062 14% profile with flap extended 20°.*

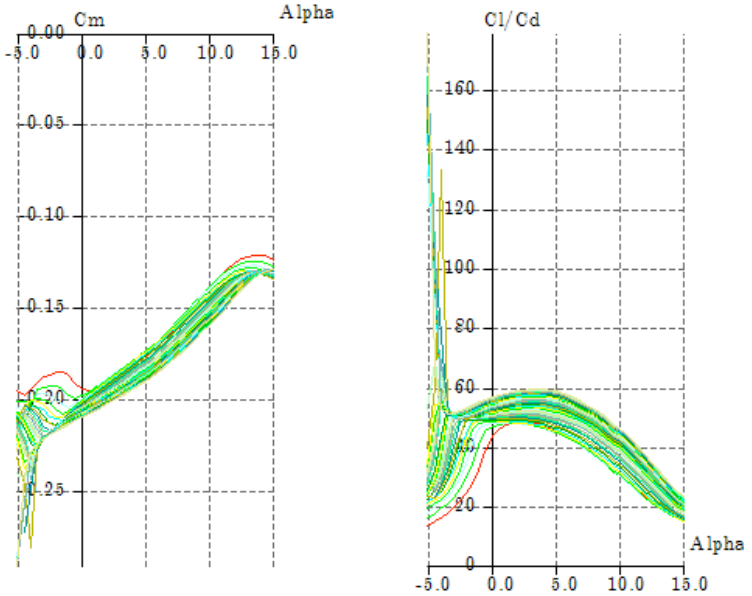

Figure 3.16 – *C_m/α and $C_l C_d/\alpha$ graph of the SD7062 14% profile with flap extended 20°.*

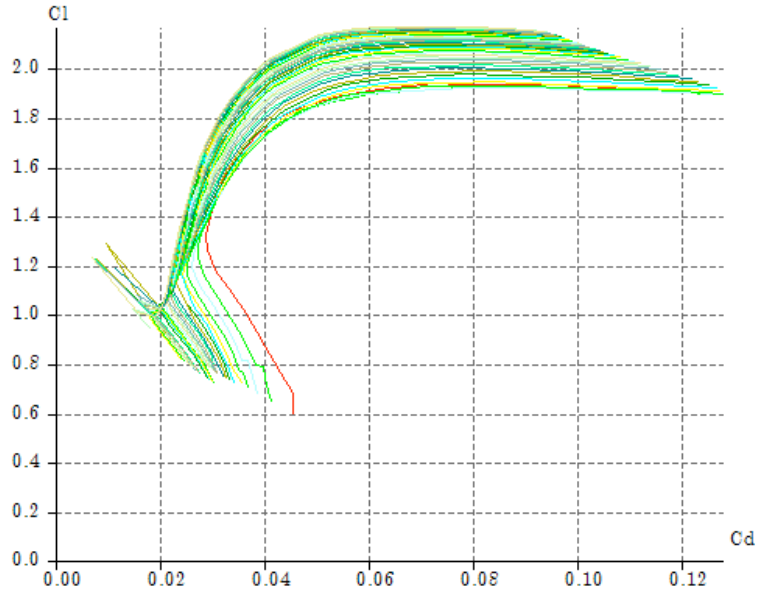

Figure 3.17 – *C_l/C_d graph of the SD7062 14% profile with flap extended 20°.*

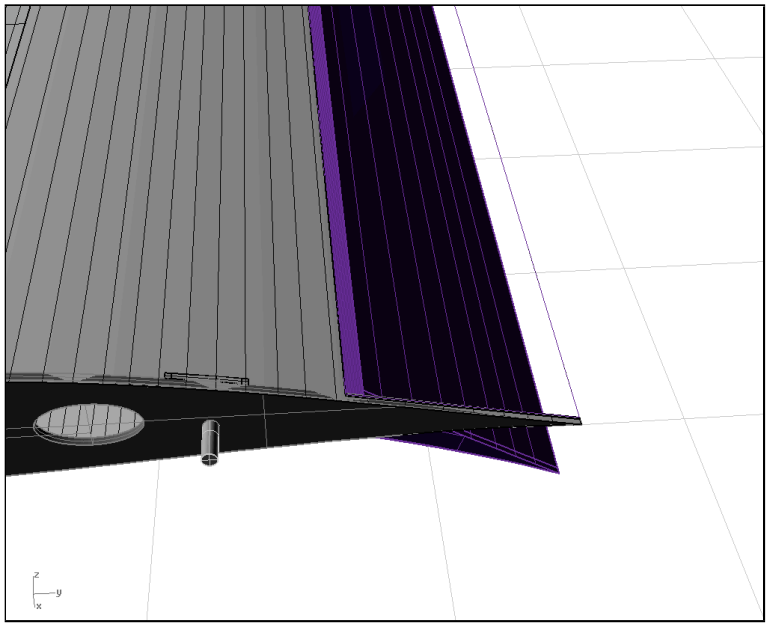

Figure 3.18 – *Modular UAS's flap zoomed view generated with Rhinoceros 4.0.*

The previous graphs were the result of the XFLR5 simulation considering the Reynold's number between 200000 and 2000000. From Figure 3.15 it is possible to read the new value of $C_{L_{max}}$ for the wing; this gives a new stall speed V_{st_+} which will be a new minimum speed for the Modular UAS [16]:

$$V_{st_+} = \sqrt{\frac{2W}{\rho S C_{L_{max}}}} = 14.47 \ m/s \tag{3.17}$$

3.3 Critical load conditions

3.3.1 Introduction

The resulting geometric design was done in collaboration with Neall Moore using the software XFLR5. The airfoil data was taken from the airfoil database of *UIUC Applied Aerodynamics Group*, and it is shown in the next figure:

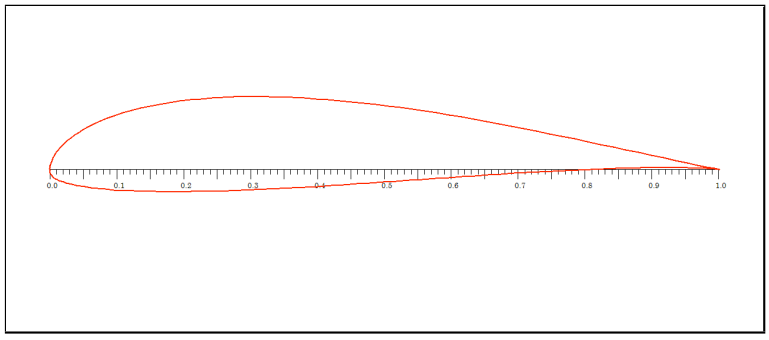

Figure 3.19 – *SD7062 14% airfoil used for the Modular UAS's new wing.*

The analysis in XFLR5 was done considering the flight conditions between two extreme speeds of the Modular UAS, i.e. the stall speed and the dive speed. The polars of the SD7062 profile are shown it the following figures:

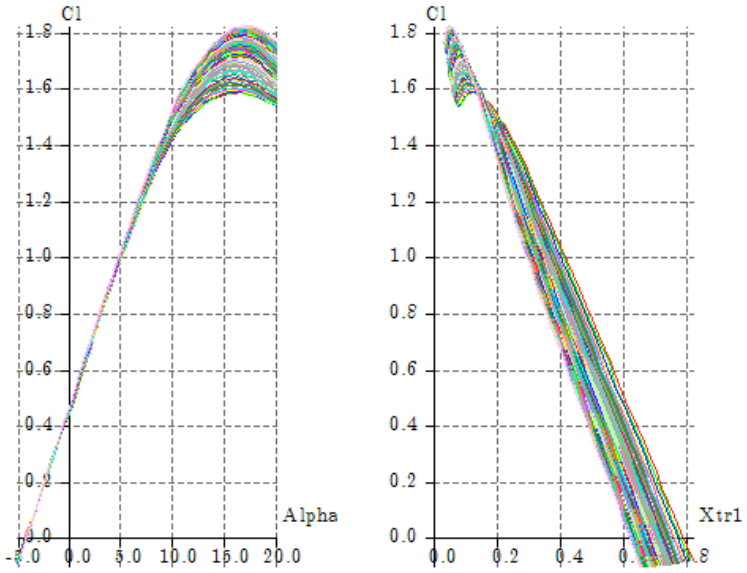

Figure 3.20 – *C_l/α and $C_l/Xtrl$ graph of the SD7062 14% profile.*

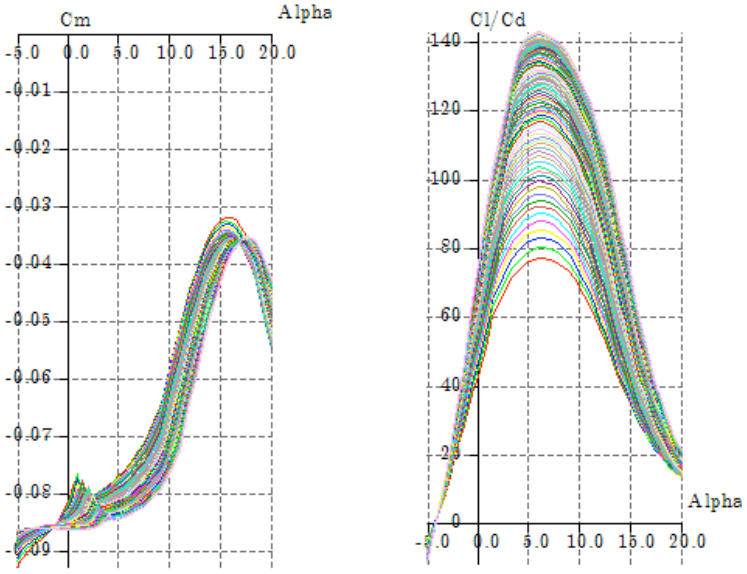

Figure 3.21 – *C_m/α and $C_l C_d/\alpha$ graph of the SD7062 14% profile.*

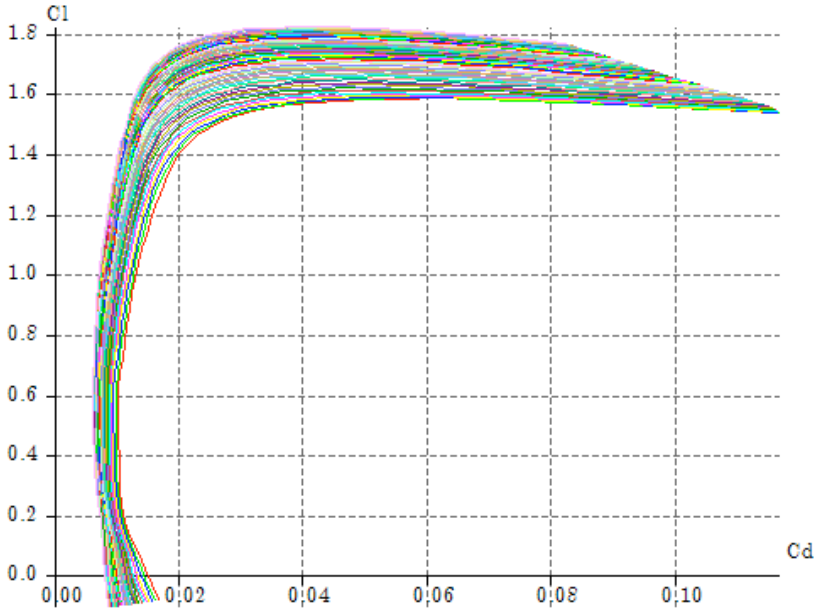

Figure 3.22 – *C_l/C_d graph of the SD7062 14% profile.*

Thus, considering the speed range of the Modular, the Reynol's number considered for the previous analysis was between 200000 to 2000000.

3.3.2 A mathematical study of the 41.89 m/s - 7.02 g condition and validation with XFLR5 (A)

Considering Figure **??** it is possible to identify the following maximum load condition [16]:

$$L = \frac{1}{2}\rho S C_{L_{max}} V_C^2 n_{max} = 3443.31 \ N \tag{3.18}$$

flying at an angle of attack of 14° which results in a $C_{L_{max}}$ of 1.676. It is assumed, for the purpose of the analysis, that the wing semi-span has a length of 2.5 m i.e. only the length from the junction with the fuselage to the wing tip is considered. This means that the load on the wing is spread equally between the two external parts of the wing and the already manufactured central part. The dimensions of the central part are 0.36 m for the constant chord and 1 m for the span. So the resulting area under

the effect of the aerodynamic loads is:

$$S_w = \frac{S - S_{cw}}{2} = 0.775 \ m^2 \tag{3.19}$$

Thus, the loads on the separate sections of the wing are:

$$\begin{aligned} L_{cw} &= \frac{1}{2}\rho S_{sw} C_{L_{max}} V_C^2 n_{max} = 648.49 \ N \\ L_w &= \frac{1}{2}\rho S_w C_{L_{max}} V_C^2 n_{max} = 1396.055 \ N \end{aligned} \tag{3.20}$$

To consider a proportional distribution of the lift between the two parts is a conservative hypothesis compared to the real lift distribution, especially at the tip, so the part of the wing designed for this work will carry less load than the one shown in the previous equation. The function of the chord along the wing span is described as following:

$$\begin{cases} c_1 = 0.16 + 0.422222y \\ c_2 = 0.255 + 0.068085y \\ c_3 = 0.335 + 0.022727y \end{cases}$$

The expected total weight of the wing is 11 kg, divided in 2 kg for the central section and 4.5 kg for each half wing. Assuming that the distributed loads given by the lift and the mass of the wing are proportional to the chord [16], the resulting equation gives:

$$\begin{aligned} p(y) = l(y) - gm(y) &= \frac{9.81 n_{max}(m - m_w)}{S} c(y) \\ &= 1406.168 \ c(y) \ N/m^2 \end{aligned} \tag{3.21}$$

The Matlab code available in Appendix A.2.1 was generated to calculate the distributed loads on the half wing considering the C_l of the airfoil constant along the wing span. This hypothesis is conservative because it considers a small additive contribute of the lift coefficient at the wing tip, which is smaller in the true situation because of the lower Reynold's number where the chord of the airfoil is smaller. From Figure **??** it is possible to note that this approximation is almost negligible due to the main constant part of the C_l. Thus, the result of the Matlab script is:

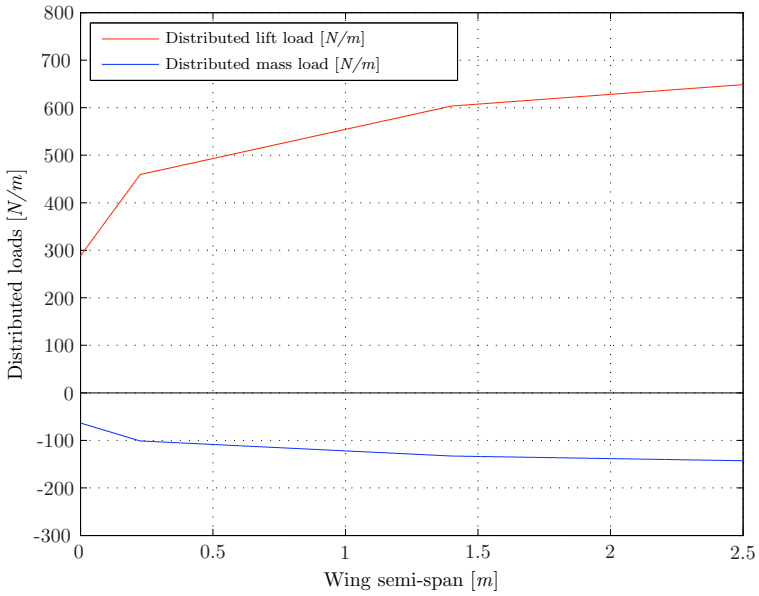

Figure 3.23 – *Matlab plot of the lift and mass loads at the flight condition V_C and 7.02 g.*

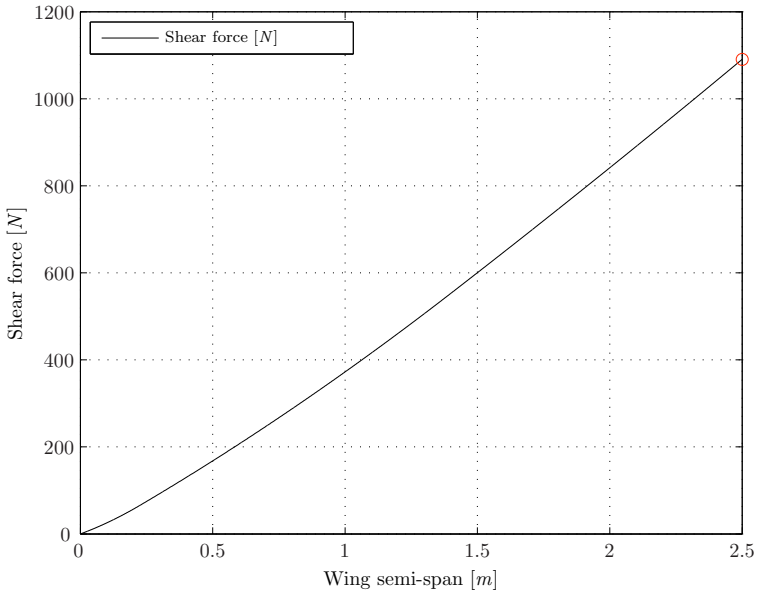

Figure 3.24 – *Matlab plot of the shear force at the flight condition V_C and 7.02 g.*

Thus, using the root as ref point, the equation that describes the internal shear loads is [16]:

$$\begin{aligned} T(y) + dT(y) - T(y) &= p(y)dy \\ \implies \int \frac{dT(y)}{dy}\, dy &= \int p(y)\, dy \\ \implies T(y) &= \int_0^y p(y)\, dy \end{aligned} \tag{3.22}$$

and the bending moment [16]:

$$\begin{aligned} M(y) + dM(y) - M(y) + T(y)dy &= p(y)dy^2 \\ \implies \int \frac{dM(y)}{dy}\, dy &= -\int T(y)\, dy \\ \implies M(y) &= -\int_0^y T(y)\, dy \end{aligned} \tag{3.23}$$

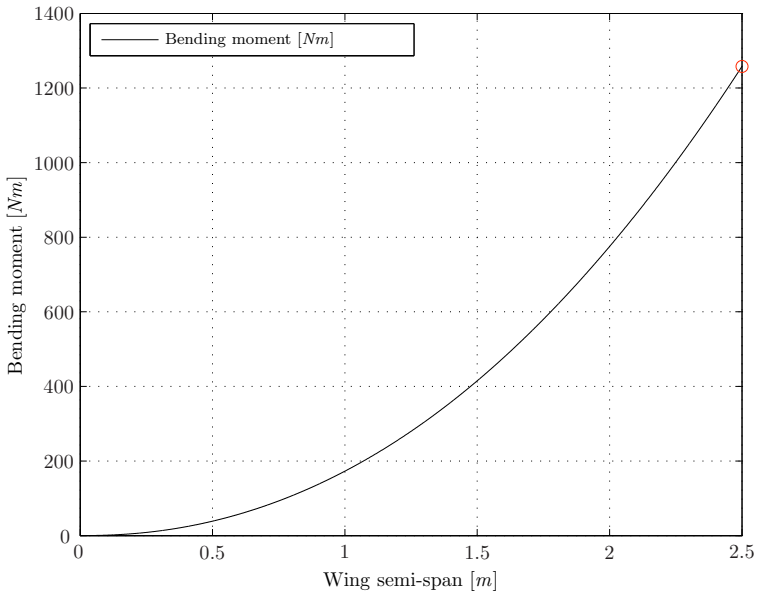

Figure 3.25 – *Matlab plot of the bending moment at the flight condition V_C and 7.02 g.*

The maximum bending moment acting at the root section is highlighted with a red circle. A validation of these result has been done by running a simulation with XFLR5 at the same flight condition. The resulting C_l, C_m and C_p distributions are shown in the next figures. The graph of the pressure coefficient for the flight condition studied shows how the area of the airfoil more affected by the aerodynamic loads remains the leading edge. Thus, in the design, this will be taken into account, particularly with respect to the rigidity of the leading edge itself. From Figure **??**, the resulting bending moment at the root (2.5 m from the tip, 0.5 m from the center of the wing) is approximately 1250 Nm, which is the same result generated with the Matlab analysis. The torque moment was calculated with the results from the XFLR5 simulation, using the data from the Figure **??**. The integration of every airfoil torque contribution along the wing span gives the torque distribution as following [6]:

$$m = \frac{1}{2}\rho V_C^2 c(y)^2 c_{m_{airfoil}} \implies M_t = \int_0^y m\, dy \tag{3.24}$$

and the resulting plot for the torque moment generated with Matlab (script available in Appendix A.2.2) is shown in Figure **??**.

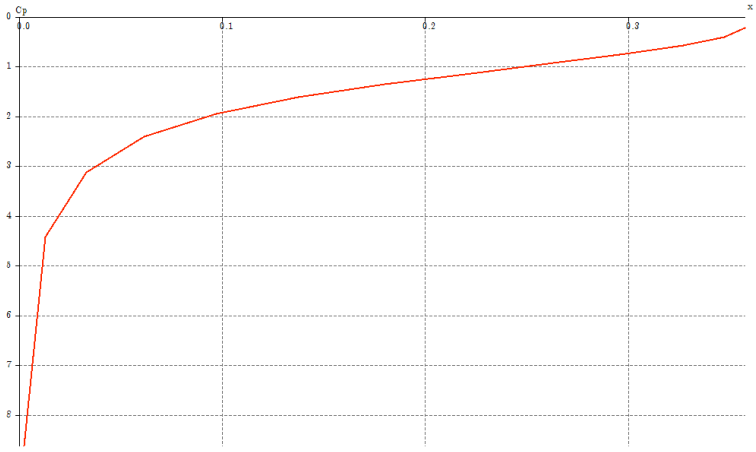

Figure 3.26 – *Coefficient of pressure distribution of the airfoil at the flight condition V_C and 7.02 g.*

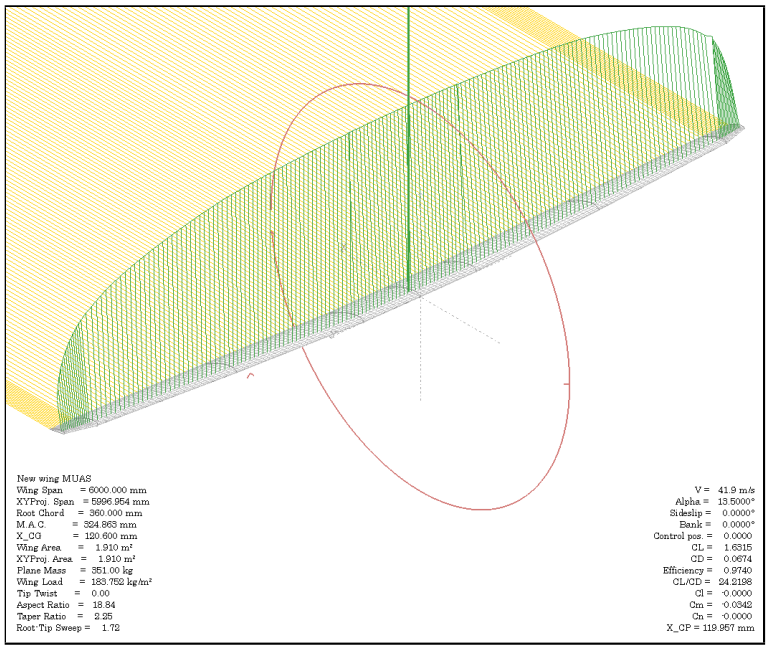

Figure 3.27 – *Lift distribution (in green) of the wing at the flight condition V_C and 7.02 g.*

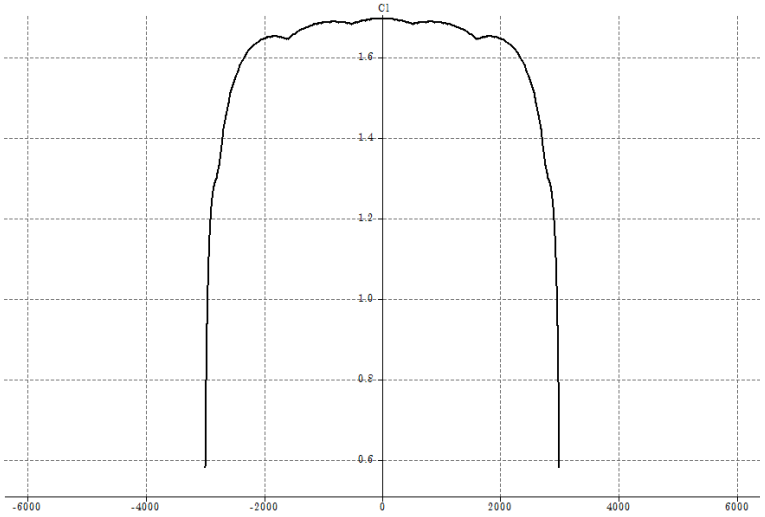

Figure 3.28 – *Lift coefficient distribution of the wing at the flight condition V_C and 7.02 g.*

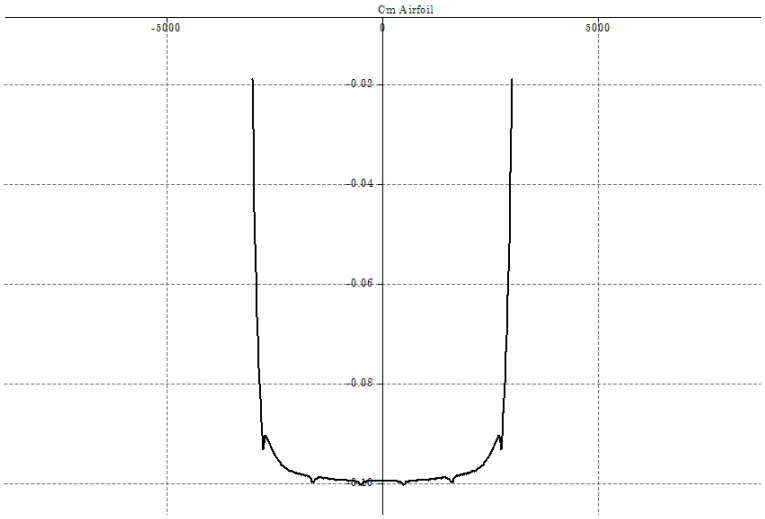

Figure 3.29 – *Moment coefficient distribution of the wing at the flight condition V_C and 7.02 g.*

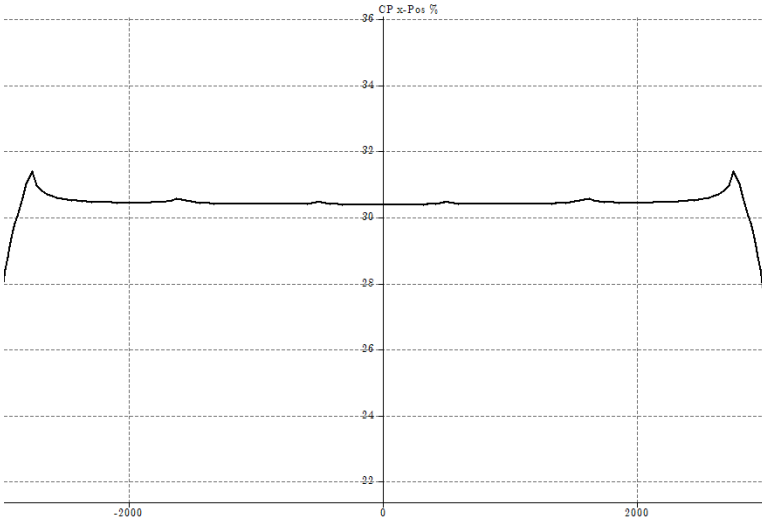

Figure 3.30 – *Center of pressure distribution of the wing at the flight condition V_C and 7.02 g.*

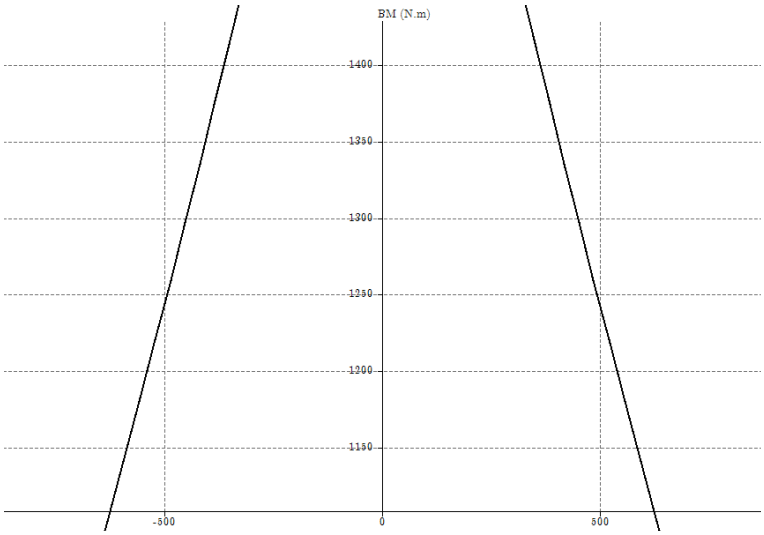

Figure 3.31 – *XFLR5 simulation of the bending moment at the flight condition V_C and 7.02 g.*

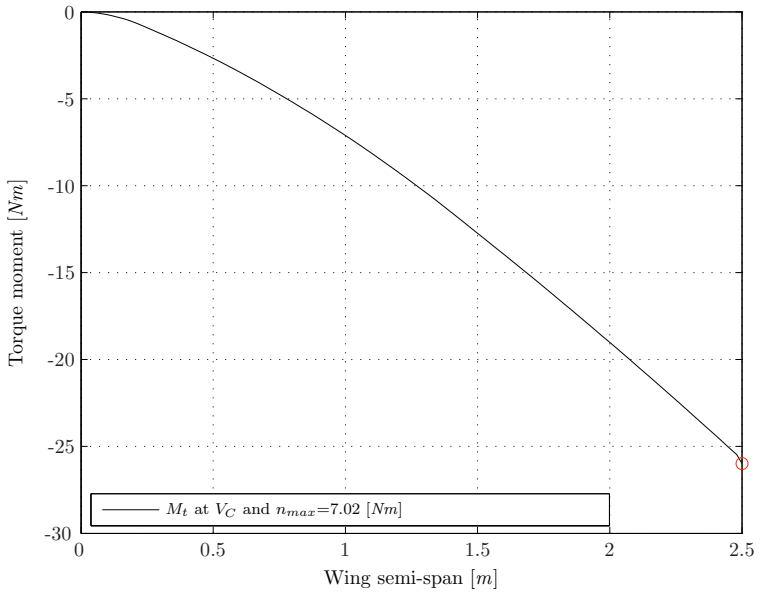

Figure 3.32 – *Matlab plot of the torque moment at the flight condition V_C and 7.02 g.*

Thus, the resulting internal loads for the wing sections at which critical

or possible ribs positions are expected, are shown in the Table below; the most critical section is at the root:

y $[m]$	T $[N]$	M_b $[Nm]$	M_t $[Nm]$
0.0000	0000.0000	0000.0000	-00.0000
0.2250	0021.6218	0024.0667	-00.6862
0.8125	0281.8274	0112.6648	-05.4898
1.4000	0553.0636	0357.3741	-11.7511
1.9500	0816.9839	0733.6940	-18.6035
2.5000	1090.6000	1257.8000	-25.9822

Table 3.2 – *Internal loads, at the flight condition V_C and 7.02 g, of the wing sections at which critical or possible ribs positions are expected.*

3.3.3 XFLR5 analysis of the 60.98 m/s - 6 g condition (B)

The other possible critical load condition during the flight is the one regarding the maximum speed. Thus, looking the fourth boundary of the flight envelope diagram, i.e., the right side, which indicates the aircraft maximum speed limit, or dive speed it is possible to read also the corresponding maximum load factor. This speed limit, set by the manufacturer, may be the result of structural, aircraft control, engine operation or some other considerations. In the case of the Modular UAS it was preferred to follow the FAR indications regarding the dive speed [**?**] and reported in Chapter 2. From Figure **??** it is possible to identify the following dive speed load condition [16]:

$$L = \frac{1}{2}\rho S C_L V_D^2 n = 2943 \ N \tag{3.25}$$

corresponding to an angle of attack of 3° and a resulting C_L equal to 0.676. At this lift condition the distributed load will be less than the previous condition (A) with a resulting lifting force equals to 3443.31 N, so it can be correct to keep the previous condition (A) as the worst in terms of shear force and bending moment. Thus, this condition (B) has been considered only with regards to the torque moment with the same Equation 3.24 [6]. In the following figure the torque moment distribution is given:

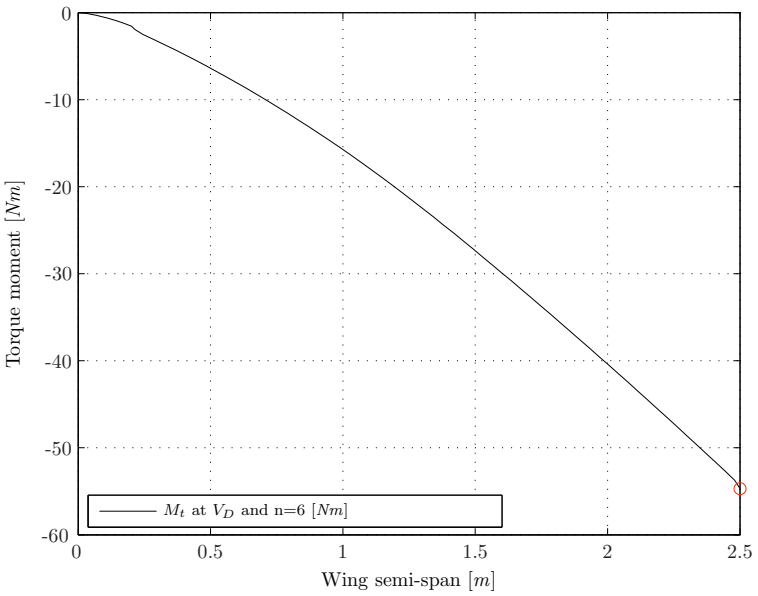

Figure 3.33 – *Matlab plot of the torque moment at the flight condition V_D and 6 g.*

3.3.4 XFLR5 analysis of the 20.558 *m/s* - 1.69 *g* condition with 20° flap and 20° aileron deflection (C)

The asymmetric maneuver has been studied following the *Standard RAI-V.EL* [2] for a UAS. The first important condition is considering the simultaneous full deflection of flap and aileron at the approach speed, defined by the Equation 3.26 [2].

$$V_{app} = 1.3V_{st_+} = 20.558 \ m/s \tag{3.26}$$

At this speed the maximum load factor, given by the aerodynamic limit, is:

$$n = \frac{\frac{1}{2}\rho S V_{app}^2 C_{L_{max}}}{W} = 1.69 \tag{3.27}$$

at an angle of attack of 5.5° and a resulting C_L equal to 1.36, in order to stay within the flight envelope. The lift distribution is shown in Figure **??**.

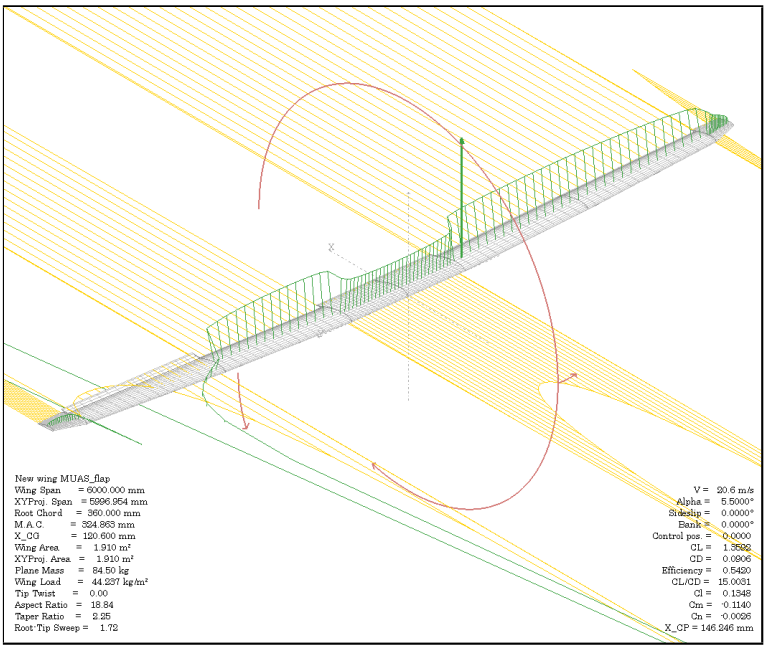

Figure 3.34 – *Lift distribution (in green) of the wing at the flight condition V_{app} and 1.69 g with 20° flap and 20° aileron deflection.*

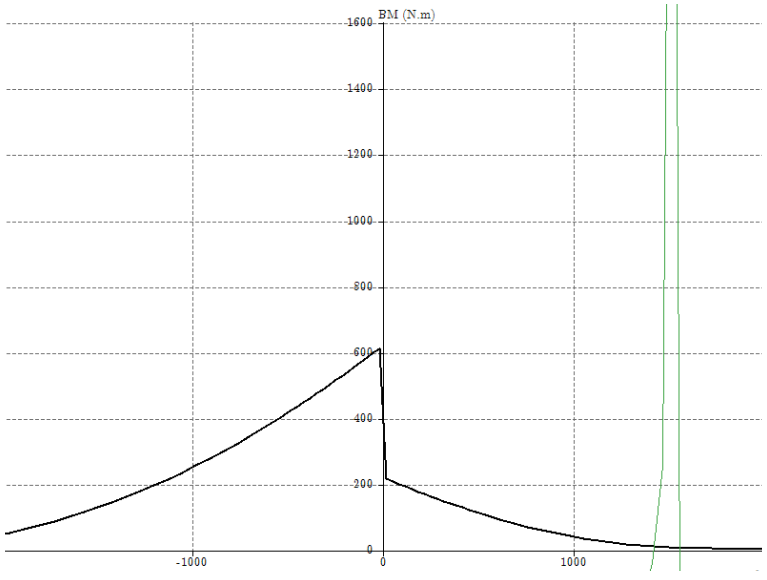

Figure 3.35 – *XFLR5 simulation of the bending moment at the flight condition V_{app} and 1.69 g with 20° flap and 20° aileron deflection.*

As can be noticed, the resulting bending moment on the wing is less than the first case (A). The resulting torque moment has been calculated with the same Equation 3.24 [6] and its distribution is shown in the following figure:

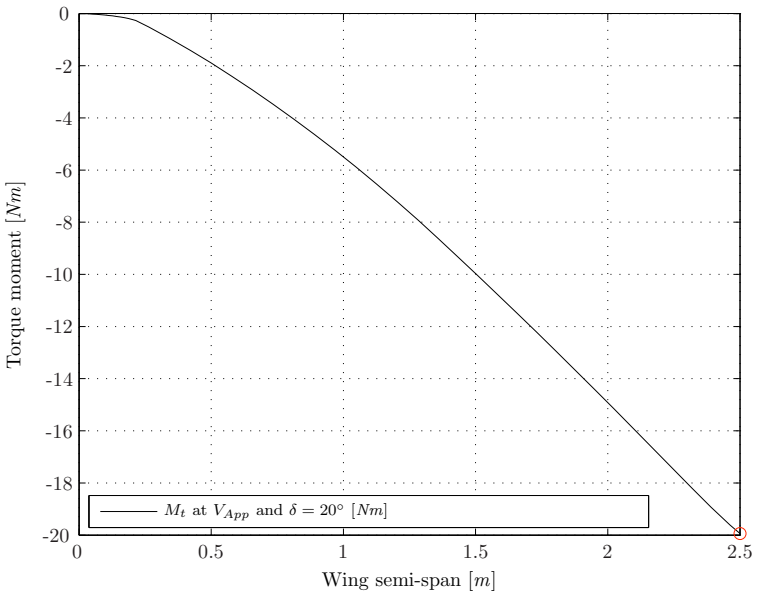

Figure 3.36 – *Matlab plot of the torque moment at the flight condition V_{app} and 1.69 g with 20° flap and 20° aileron deflection.*

3.3.5 XFLR5 analysis of the 41.89 m/s - 7.02 g condition with 20° aileron deflection (D)

The section RAI-V.EL 347(b) of [2] describes how to consider the load condition at maneuver speed, which for the Modular UAS will be V_C, in case of an asymmetric maneuver. In essence RAI-V.EL 347(b) of [2] states that 75% of the load for each wing semi-span should be considered, whilst still accounting for the total torque given by the full deflection of the aileron. The analysis was done at an angle of attack of 8.5° and a resulting C_L equal to 1.174, in order to stay within the flight envelope. As seen in Figure **??**, 75% of the maximum bending moment of 1702.36 Nm at the wing root equals 1276.77 Nm, which is still reasonably close to the value of 1257.8, calculated from the first flight condition studied (V_C -7.02 g).

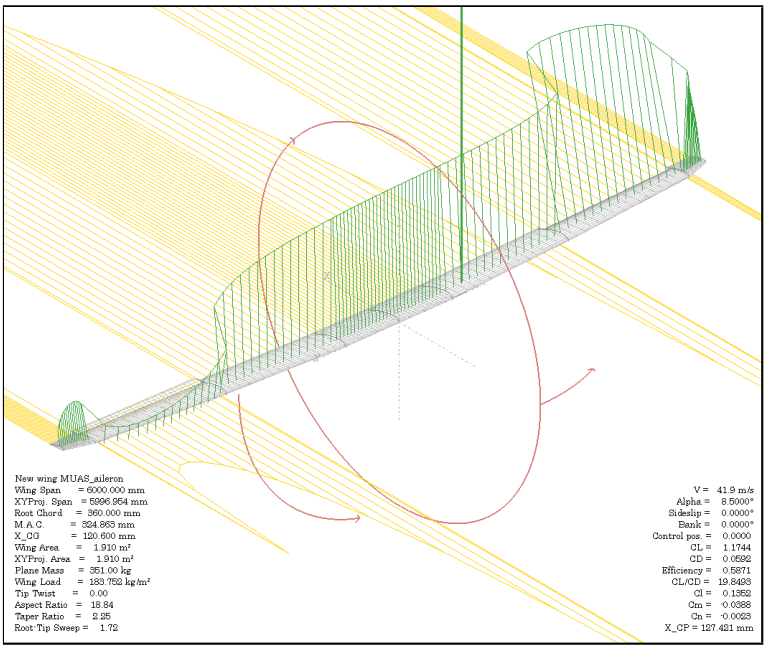

Figure 3.37 – *Lift distribution (in green) of the wing at the flight condition V_C and 7.02 g with 20° aileron deflection.*

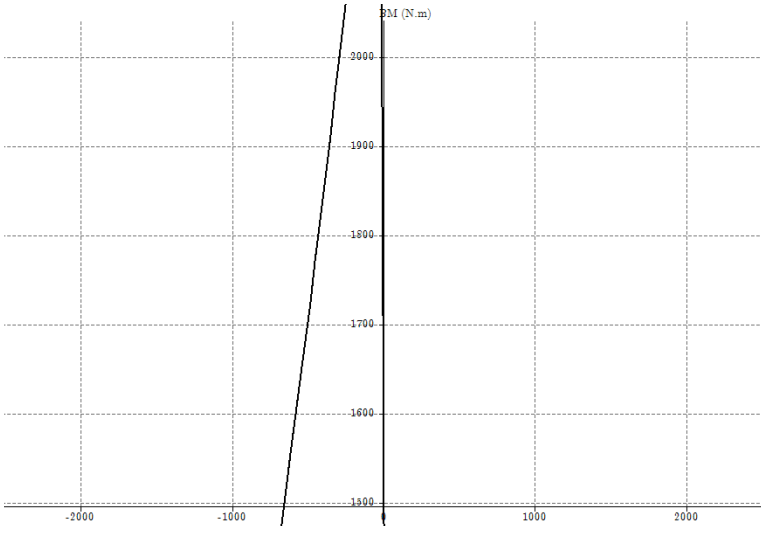

Figure 3.38 – *XFLR5 simulation of the bending moment at the flight condition V_C and 7.02 g with 20° aileron deflection.*

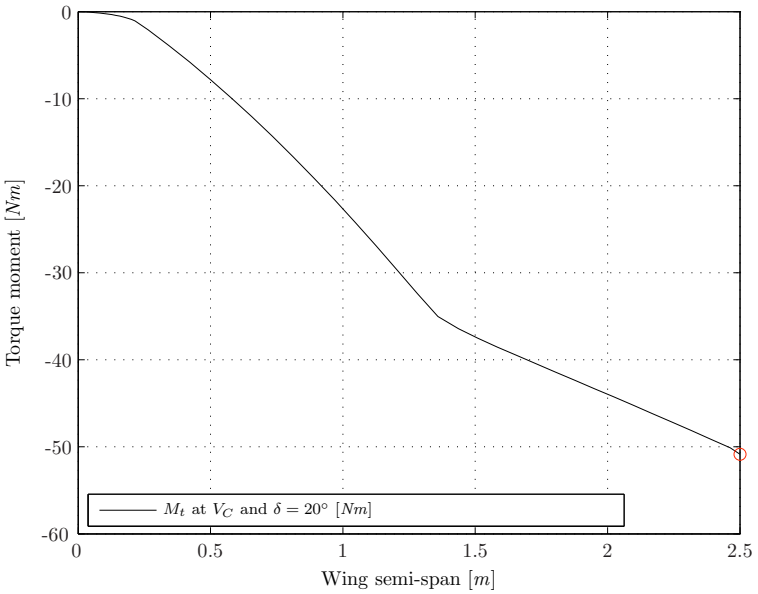

Figure 3.39 – *Matlab plot of the torque moment at the flight condition V_C and 7.02 g with 20° aileron deflection.*

It is possible to notice the higher negative gradient of the curve due to the higher value of c_m of the airfoil in the wing section close to the tip, given by the aileron deflection.

3.3.6 XFLR5 analysis of the 60.98 *m/s* - 6 *g* condition with 7° aileron deflection (E)

The section RAI-V.EL 347(b) of [2] describes how to consider the load condition at dive speed, which for the Modular UAS will be V_D, in case of an asymmetric maneuver. In essence RAI-V.EL 347(b) of [2] states that 75% of the load for each wing semi-span should be considered, whilst still accounting for the total torque given by the 1/3 deflection of the aileron which means 7° of ailerons deflection in the Modular UAS analysis. This is necessary to still have some of the control of the aircraft even in the extreme condition of dive speed. The analysis was done at an angle of attack of 3° and a resulting C_L equal to 0.664, in order to stay within the flight envelope. As seen in Figure **??**, 75% of the maximum bending moment of 1709.8 *Nm* at the wing root equals 1282.35 *Nm*, which is still reasonably close to the value of 1257.8 *Nm*, calculated from the first flight condition studied without the aileron deflection (V_C -7.02 *g*).

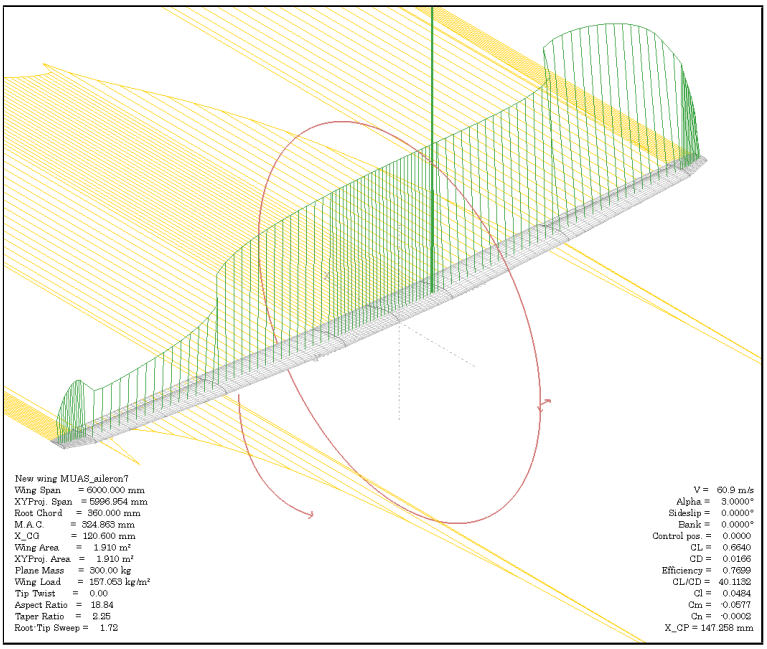

Figure 3.40 – *Lift distribution (in green) of the wing at the flight condition V_D and 6 g with 7° aileron deflection.*

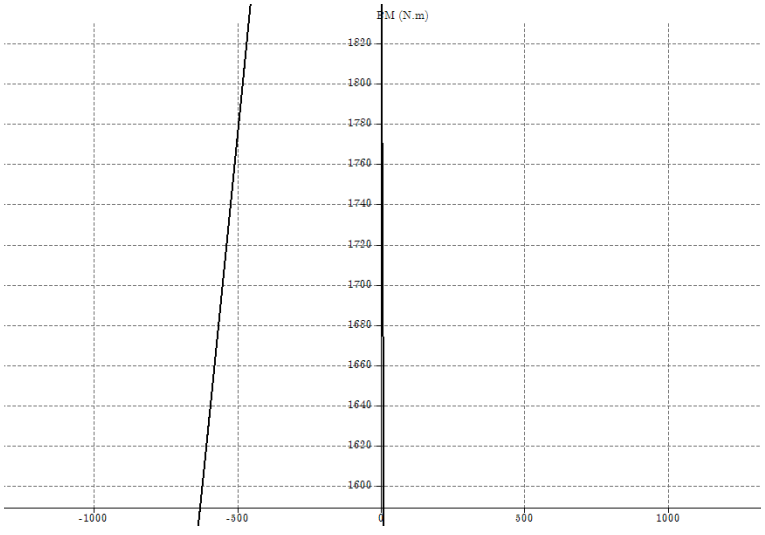

Figure 3.41 – *XFLR5 simulation of the bending moment at the flight condition V_D and 6 g with 7° aileron deflection.*

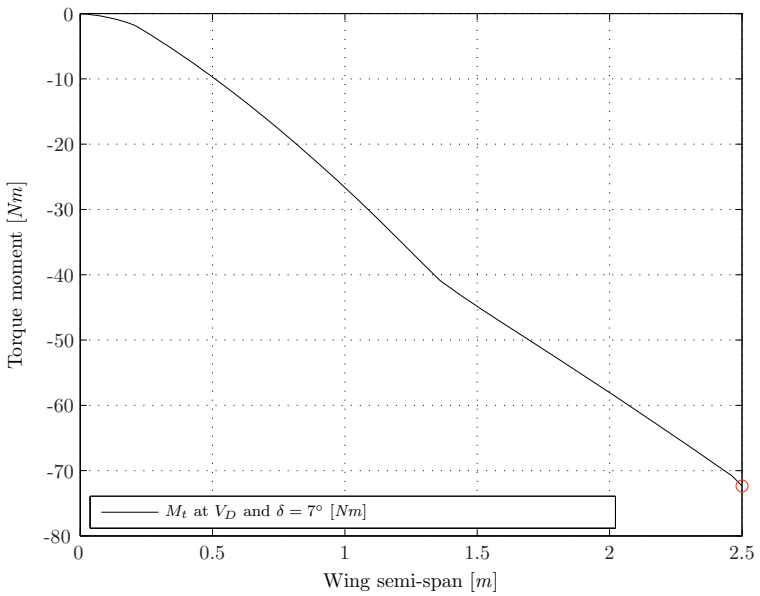

Figure 3.42 – *Matlab plot of the torque moment at the flight condition V_D and 6 g with 7° aileron deflection.*

It is possible to notice the higher negative gradient of the curve due to the higher value of c_m of the airfoil in the wing section close to the tip, given by the aileron deflection. As conclusion of this analysis will be shown the polars of the wing for every case studied.

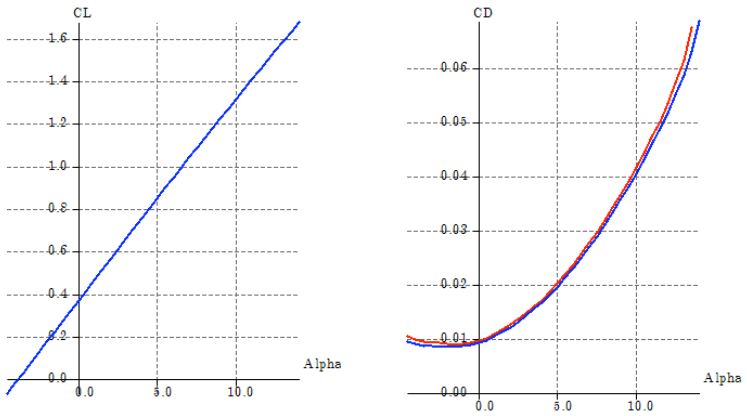

Figure 3.43 – *Polars of the wing at the flight conditions A (in red) and B (in blue) studied.*

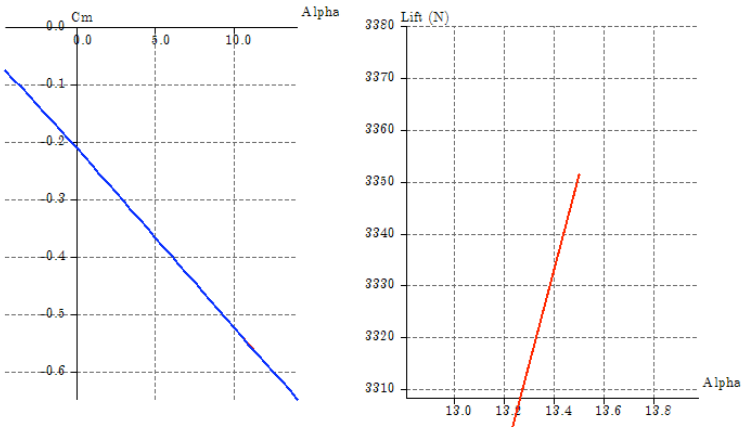

Figure 3.44 – *Polars of the wing at the flight conditions A (in red) and B (in blue) studied.*

From this graphs, made with XFLR5, it is possible to read all the informations used for the several possible critical flight conditions studied. In particular, the lift-to-alpha graph case (A) confirms also the initial hypothesis of maximum resulting load applied of 3443.31 N, flying at an angle of attack of 14° which results in a $C_{L_{max}}$ of 1.676.

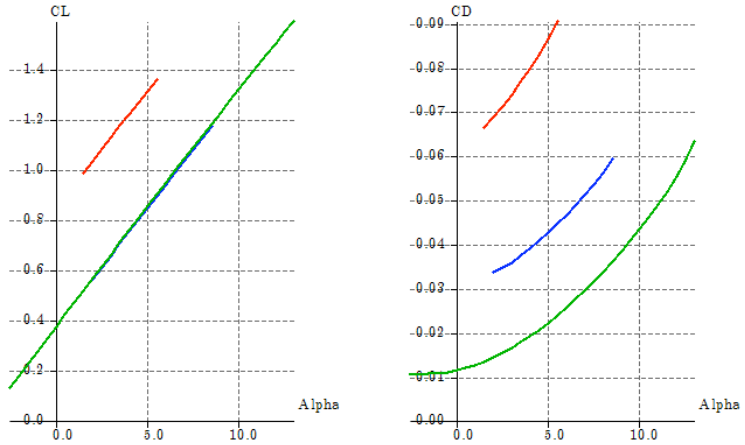

Figure 3.45 – *Polars of the wing at the flight conditions C (in red),D (in blue) and E (in green) studied.*

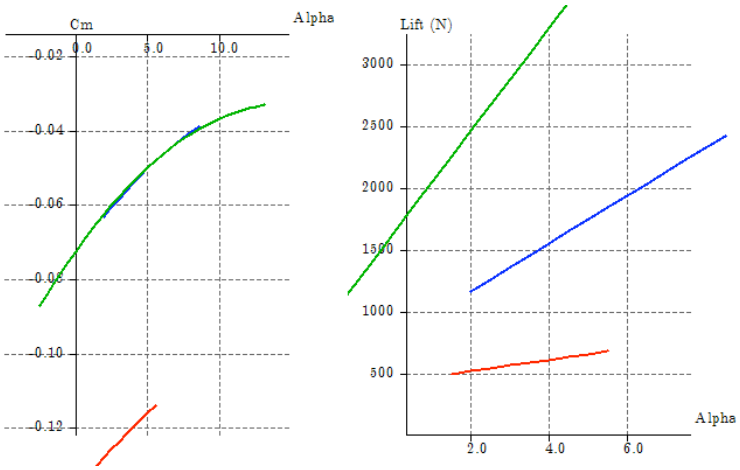

Figure 3.46 – *Polars of the wing at the flight conditions C (in red),D (in blue) and E (in green) studied.*

3.3.7 Comparison between the different torque conditions and final maximum load condition

To find out the maximum, i.e. worst, torque condition for each section a direct comparison between all the cases is reported in the following Table 3.3:

y $[m]$	$\mathbf{M}_{t_A}$ $[Nm]$	$\mathbf{M}_{t_B}$ $[Nm]$	$\mathbf{M}_{t_C}$ $[Nm]$	$\mathbf{M}_{t_D}$ $[Nm]$	$\mathbf{M}_{t_E}$ $[Nm]$
0.0000	-00.0000	-00.0000	-00.0000	-00.0000	-00.0000
0.2250	-00.6862	-01.9538	-00.2666	-01.0676	-01.9865
0.8125	-05.4898	-12.3412	-04.0436	-16.6800	-19.8113
1.4000	-11.7511	-25.3167	-09.3656	-36.4306	-43.1314
1.9500	-18.6035	-39.5284	-14.4095	-43.3101	-56.7196
2.5000	-25.9822	-54.6885	-19.9398	-50.8538	-72.3728

Table 3.3 – *Torque moments of the wing sections at which critical or possible ribs positions are expected for all cases.*

Thus, the final most critical condition considered to size the parts of the structure is the one considering the shear force and the bending moment at V_C and maximum load factor, and the torque moment given by the V_D

with 1/3 of aileron deflection. This can be considered conservative, also because the different elements that constitute the wings are going to work separately; the spar will be affected by the of bending moment at cruise speed and maximum load factor, and the junction web of the wing with the fuselage will be affected by the torque moment at dive speed with 1/3 of aileron deflection. The results are shown below:

y $[m]$	**T** $[N]$	$\mathbf{M}_b$ $[Nm]$	$\mathbf{M}_t$ $[Nm]$
0.0000	0000.0000	0000.0000	-00.0000
0.2250	0021.6218	0024.0667	-01.9865
0.8125	0281.8274	0112.6648	-19.8113
1.4000	0553.0636	0357.3741	-43.1314
1.9500	0816.9839	0733.6940	-56.7196
2.5000	1090.6000	1257.8000	-72.3728

Table 3.4 – *Internal loads of the wing sections at which critical or possible ribs positions are expected.*

Following the regulation [2], the section RAI-V.EL 303 imposes to use a safety factor of 1.5 on the loads, and as suggested by John Monk also an extended 1.2 factor must be considered to take into account manufacturing defects that can affect the properties of the handmade composite structure. Thus, the final loads considered for the wing structure design are:

y $[m]$	**T** $[N]$	$\mathbf{M}_b$ $[Nm]$	$\mathbf{M}_t$ $[Nm]$
0.0000	0000.0000	0000.0000	-000.0000
0.2250	0038.9192	0043.3201	-003.5757
0.8125	0507.2893	0202.7966	-035.6603
1.4000	0995.5145	0643.2734	-077.6365
1.9500	1470.5710	1320.6492	-102.0953
2.5000	1963.0800	2264.0400	-130.2710

Table 3.5 – *Internal loads, include safety factors, of the wing sections at which critical or possible ribs positions are expected.*

3.4 Hinge moments of the flap and the aileron

3.4.1 Flap hinge moment at the 20.558 m/s - 1.69 g condition with 20° flap and 20° aileron deflection (C)

To know how much force is needed to control the plain flap with the servos, an hinge moment study is now done. In the following Table 3.6 are listed all the data necessary for this study; most of them are taken from the *DATCOM method* [7]:

FLAP DATA		
c_f/c [%]	Geometry	25.000
C_f $[m]$	Geometry	0.087
S_f $[m^2]$	Geometry	0.095
δ_a [°]	Paragraph 3.2.3	20.000
C_{l_α} $[rad^{-1}]$	XFLR5	5.500
$C_{l_{\alpha(theory)}}$ $[rad^{-1}]$	[7] Fig. 4.1.1.2-8	7.000
$C_{l_{\delta(theory)}}$ $[rad^{-1}]$	[7] Fig. 6.1.1.1-25a	4.200
$C_{l_\delta}/C_{l_{\delta(theory)}}$	[7] Fig. 6.1.1.1-25b	0.630
K'	[7] Fig. 6.1.1.1-26	0.850
$C_{h_{\alpha(theory)}}$ $[rad^{-1}]$	[7] Fig. 6.1.3.1-7a	−0.450
$C_{h_\alpha}/C_{h_{\alpha(theory)}}$	[7] Fig. 6.1.3.1-7b	0.280
$C_{h_{\delta_{theory}}}$ $[rad^{-1}]$	[7] Fig. 6.1.3.2-7a	−0.780
$C_{h_\delta}/C_{h_{\delta(theory)}}$	[7] Fig. 6.1.3.2-7b	0.850

Table 3.6 – *Flap data necessary for the hinge moment study.*

Thus, according with [7]:

$$\begin{aligned} \frac{C_{l_\alpha}}{C_{l_{\alpha(theory)}}} &= 0.786 \\ C_{l_\delta} &= 2.646\ rad^{-1} \\ C_{h_\alpha} &= -0.126\ rad^{-1} \\ C_{h_\delta} &= -0.663\ rad^{-1} \\ \frac{\Delta C_{L_\delta}}{\delta_f} = \frac{C_{l_\delta}}{C_{l_{\delta(theory)}}} C_{l_{\delta(theory)}} K' &= 2.249\ rad^{-1} \end{aligned} \tag{3.28}$$

The resulting hinge moment coefficient, considering an angle of attack equal to 5.5° and a deflection of 20°, is [7]:

$$C_{h_C} = C_{h_\alpha}\alpha + C_{h_\delta}\delta = -0.2435 \tag{3.29}$$

leading to the hinge moment:

$$HM_C = \frac{1}{2}\rho V_C^2 S_a C_a C_h = -0.5231 \ Nm \tag{3.30}$$

and to the force necessary to move the flap, considering a hinge distance of 0.025 m, is:

$$HF_C = \frac{HM}{d} = -20.901 \ N \tag{3.31}$$

3.4.2 Aileron hinge moment at the 41.89 m/s - 7.02 g condition with 20° aileron deflection (D)

To know how much force is needed to control the aileron with the servos, an hinge moment study is now done. In the following Table 3.7 are listed all the data necessary for this study; most of them are taken from the *DATCOM method* [7]. Thus, according with [7]:

$$\begin{gathered} \frac{C_{l_\alpha}}{C_{l_{\alpha(theory)}}} = 0.786 \\ C_{l_\delta} = 2.646 \ rad^{-1} \\ C_{h_\alpha} = -0.126 \ rad^{-1} \\ C_{h_\delta} = -0.663 \ rad^{-1} \\ \frac{\Delta C_{L_\delta}}{\delta_f} = \frac{C_{l_\delta}}{C_{l_{\delta(theory)}}} C_{l_{\delta(theory)}} K' = 2.249 \ rad^{-1} \end{gathered} \tag{3.32}$$

The resulting hinge moment coefficient, considering an angle of attack equals to 8.5° and a deflection of 20°, is [7]:

$$C_{h_D} = C_{h_\alpha}\alpha + C_{h_\delta}\delta = -0.2501 \tag{3.33}$$

AILERON DATA		
c_a/c [%]	Geometry	25.000
C_a $[m]$	Geometry	0.074
S_a $[m^2]$	Geometry	0.086
δ_a [°]	Paragraph 3.2.2	20.000
C_{l_α} $[rad^{-1}]$	XFLR5	5.500
$C_{l_{\alpha(theory)}}$ $[rad^{-1}]$	[7] Fig. 4.1.1.2-8	7.000
$C_{l_{\delta(theory)}}$ $[rad^{-1}]$	[7] Fig. 6.1.1.1-25a	4.200
$C_{l_\delta}/C_{l_{\delta(theory)}}$	[7] Fig. 6.1.1.1-25b	0.630
K'	[7] Fig. 6.1.1.1-26	0.850
$C_{h_{\alpha(theory)}}$ $[rad^{-1}]$	[7] Fig. 6.1.3.1-7a	−0.450
$C_{h_\alpha}/C_{h_{\alpha(theory)}}$	[7] Fig. 6.1.3.1-7b	0.280
$C_{h_{\delta_{theory}}}$ $[rad^{-1}]$	[7] Fig. 6.1.3.2-7a	−0.780
$C_{h_\delta}/C_{h_{\delta(theory)}}$	[7] Fig. 6.1.3.2-7b	0.850

Table 3.7 – *Aileron data necessary for the hinge moment study.*

leading to the hinge moment:

$$HM_D = \frac{1}{2}\rho V_C^2 S_a C_a C_h = -1.7108\ Nm \tag{3.34}$$

and to the force necessary to move the aileron, considering a hinge distance of 0.025 m, is:

$$HF_D = \frac{HM}{d} = -68.434\ N \tag{3.35}$$

3.4.3 Aileron hinge moment at the 60.98 m/s - 6 g condition with 7° aileron deflection (E)

For the flight condition E, the resulting hinge moment coefficient, considering an angle of attack equals to 3° and a deflection of 7°, is [7]:

$$C_{h_E} = C_{h_\alpha}\alpha + C_{h_\delta}\delta = -0.0876 \tag{3.36}$$

leading to the hinge moment:

$$HM_E = \frac{1}{2}\rho V_D^2 S_a C_a C_h = -1.2697 \ Nm \tag{3.37}$$

and to the force necessary to move the aileron, considering an hinge distance of 0.025 m, is:

$$HF_E = \frac{HM}{d} = -50.788 \ N \tag{3.38}$$

Chapter 4

Composite materials selection and test

4.1 The composite materials

4.1.1 Introduction

To motivate a complicated choice to use composite materials, one must compare them to other materials like the most common metals. The cost and weight are among the two most important variables that determine what type of material it is better to use, and usually there is an inverse correlation between the two. However, this relationship is not always true, in fact to the pure cost of material, must be added the costs of manufacture and tools needed. Manufacturing techniques of composite materials make it possible to obtain complex shapes in a single operation, reducing eventually the production costs compared for a similar structure in metal or wood, since these often require an assembly of many parts, by means of rivets, welding or nails. So, the final cost of a composite structure is usually minor but the material itself is more expensive. Moreover, forms with complex contours can be easily obtained and installed, which normally is hard to do with metal or wood, and this enables designers to conceive structures as close as possible to their specific needs. For example, usually in a finished alloy made aircraft there is a riveting junction between the surfaces, not present in the case of composite panels, which increases aerodynamic drag of a tense 10%, and a corresponding fuel consumption. This is also true in the case of composite rotors used in helicopters. As already highlighted in the case of the *Boeing 787*, an enticing advantage for airliners is the

reduction of maintenance on the metal parts, usually subject to corrosion, not present when using of composites. Last but perhaps most important, as incentive to develop application studies, were the results obtained in strength and rigidity of these materials in relation to their density, making it a winning point in an industry where the weight optimization is one of the first necessity [9]. Weight savings can be in the order of 30%. Another major difference between metals and composite lies in their macroscopic structure. The first are isotropic, i.e. the structural properties of the material are the same regardless of the direction, and so it will behave in the same way whatever the stress direction. This is not true for composites which are orthotropic, having a different behavior along the three directions, namely the fibers direction and the direction perpendicular to them. It is possible to overcome this problem, using a *laminate*, i.e. the result of layup methods that makes it possible to reach an "almost-isotropy". In the next Figure 4.1 is possible to notice the orthotropic behavior applying a longitudinal load to a ssmple plate [9].

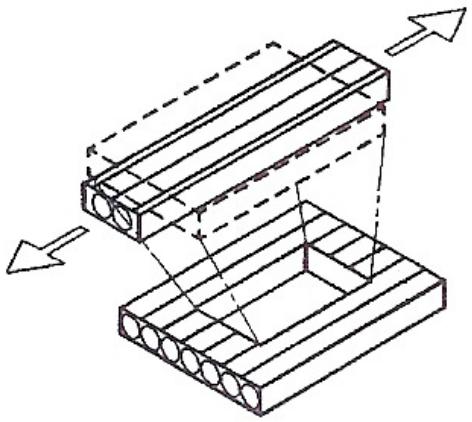

Figure 4.1 – *Example of the orthotropic behavior with 4 different elastic coefficients [9].*

Stressing a laminate of orthotropic material in its plan, it is possible to observe the effects of orthotropy in deformation of a body. For any orientation of the reinforcing fibers, one can notice that the single normal stress applied to isotropic and orthotropic plates, cause in both longitudinal expansion and transverse contraction and in addition, but just in the second one, an angular distortion. In the simple case of two dimensional stress condition (in the plane of the plate), one can obtain the elastic coefficients

that allow to tie the stresses applied to the deformation that they induce. Cutting out a unitary surface element, we can obtain independent relations from the scrollwork reference [9].

4.1.2 Mathematical model for composite materials

For an orthotropic material, cutting out a unitary surface element, it is possible to obtain the relationship between stresses and deformations, remembering that in this case the material properties are different in the two directions, so one gets E_x, E_y, ν_{yx} and ν_{xy} [15].

$$\begin{Bmatrix} \epsilon_x \\ \epsilon_y \\ \gamma_{xy} \end{Bmatrix} = \begin{bmatrix} 1/E_x & -\nu_{yx}/E_y & 0 \\ -\nu_{xy}/E_x & 1/E_y & 0 \\ 0 & 0 & 1/G_{xy} \end{bmatrix} \begin{Bmatrix} \sigma_x \\ \sigma_y \\ \tau_{xy} \end{Bmatrix}$$

In the coefficients matrix seems like asymmetric even if the structure is symmetric. The number of coefficient apparently distinct are five, i.e. [15]:

- two Young's moduli E_x and E_y;
- two Poisson's coefficients ν_{yx} and ν_{xy};
- one shear modulus G_{xy}

Actually, the number of distinct elastic coefficient are just four, i.e.:

- two Young's moduli E_x and E_y;
- one shear modulus G_{xy}
- a fourth elastic relation that can be written as a function of Poisson's coefficients.

$$\nu_{yx}E_x = \nu_{xy}Ey \tag{4.1}$$

To get the elastic moduli and Poisson's coefficients it is possible to use directly some samples taken from the considered laminate, and carry out tensile tests getting the curve σ-ϵ: with a sample cut out in y direction one will get E_y and ν_{xy}; with a sample cut out in x direction one will get E_x

and ν_{yx}; with a sample obtained from a 45° between x and y one will get G_{xy} [15]:

$$G_{xy} = \frac{E_{45^\circ}}{2(1 + \nu_{45^\circ})} \tag{4.2}$$

From the Theory of Lamination, the shear stress τ and the shear strain γ can be expressed by the normal stress, the longitudinal and transversal strain ϵ_x and ϵ_y using the following equations [15]:

$$\tau = \frac{\sigma}{2} \tag{4.3}$$

$$\gamma = |\epsilon_x| + |\epsilon_y| \tag{4.4}$$

4.2 Materials selection for the new wing

4.2.1 The epoxy resin

The large family of epoxy resins represents the group with the highest available properties nowadays. Epoxy resins are low molecular weight prepolymers able to be used in a variety of conditions. There are two major advantages of these resins than unsaturated polyester resins: the first is that the epoxy resins can be processed chemically and stored in this state, the latter is that they show a low shrinkage during the chemical process of curing. However, the viscosity of the most common epoxy resins is higher than polyester resins and they are also more expensive than the latter. The epoxy resins, after the chemical process, have high chemical and corrosion resistance, good mechanical and thermal properties, adhesive ability with multiple elements and good electrical properties, and so are one of the better types used for the production of aircraft parts. Their biggest limitations consist in the long time needed for the curing reaction and poor performance in applications with hot-humid environments.

Today there is a wide group of epoxy resins, ranging from the low-temperature resistant resins used in the construction industry, to the brittle epoxy resins very useful in the aerospace field. This wide range is due primarily to the availability of resins with different molecular structures and different molecular weights, which allow to get a broad range of products, from those with low molecular weight as liquids, to solids with a low melting point. The mechanical properties of epoxy resins depend on the chemical structure of the reagent introduced in the reaction, on the stoichiometric relationship between epoxides and amines, on the density of cross-links after the reaction, on the evaluation of temperature and on elongation percentage. The tensile strength and tensile modulus of epoxy are in the range of 40-130 MPa and 2-4.1 GPa respectively. Ultimate deformation lies in the range between 2% and 9%. Shrinking as a result of the curing reaction is low in these resins, roughly 1.5% and the specific weight is around 1.2-1.3 g/cm^3 [9]. The Ampreg 21 was chosen (provided by *Advanced Materials Composites L.t.d.*), which has been optimised for the manufacture of large composite structures using hand layup and vacuum bagging techniques [21].

EXOPY RESIN AMPREG 21 WORKING SPECIFICATIONS	
Initial mixed viscosity $[cP]$	537.00
Pot life $[h.min]$	0.33
Earliest time to apply vacuum $[h.min]$	2.10
Latest time to apply vacuum $[h.min]$	2.45
Earliest time to turn off vacuum $[h.min]$	4.38

Table 4.1 – *Working characteristics of the resin Ampreg 21 with standard hardener at 25 °C[21].*

The relatively low initial mixed viscosity of Ampreg 21 allows easy wet out of heavyweight reinforcements. The resin Ampreg 21 has been designed to give excellent mechanical and thermal properties from both ambient temperature cures, and moderate postcures temperature (50 $°C$). This system is available with a range of hardener speeds, from fast to extra slow. Due to the dimension of the wing and the possibility to layup one half wing per side the standard hardener was chosen. Ampreg 21 is optimised for a use between 18 $°C$ and 25 $°C$ and it is important that the resin and hardener components are measured out accurately in the ratio of 3 to 1. The two components must be mixed thoroughly and if mixing is done by hand particular attention should be paid to the side and bottom of the mixing vessel [21].

The system Ampreg 21 has been developed to provide good mechanical properties after cure at room temperature: the minimum recommended cure temperature is 18 $°C$. Excellent mechanical/thermal properties could be achieved after a post-cure at elevated temperature but it was not possible due to the wing dimensions and to the DPSS ASC's Composite Laboratory equipment. An initial cure of at least 48 hours (with slow hardener) or 16 hours (with fast hardener) at 18 $°C$ is recommended before demoulding.

4.2.2 The reinforcement fibers

In the field of advanced composites, carbon fibers are the most relevant reinforcement due to their high strength and high stiffness combined with low density. There are several types of carbon fibers depending on the diameter of the single fiber and the treatments. The *PAN* process can be optimized to produce high-strength (HS) or high-modulus (HM) fibers, with typical diameter of 8 μm. The two terms carbon and graphite are often used as synonyms, however they are different [9]. Advanced Composites Materials L.t.d. provides high-strength carbon fabric 200 g/m^2, twill weave. which is the most commonly used carbon fabric for cosmetic applications. It is suitable for use in wet-lay, vacuum bagging and resin infusion manufacture as well as for skinning objects with carbon. The twill weave offers exceptional drapability and will follow compound curvature. The weave is easily distorted however but the epoxy fixed (powder coated) version of this fabric, which is often more suitable for demanding cosmetic applications where weave distortion cannot be accepted, is not a valid solution for this purpose. Each ply of this carbon fabric, wet out with an equal mass of resin will be approximately 0.22 mm in thickness [21].

4.3 The characterization of the composite laminate with tensile tests

4.3.1 Introduction

The characterization of the laminate is any procedure, theoretical or experimental, which is necessary to establish all the mechanical character-

istics of the product. The theoretical method is based on the *Theory of Lamination* which provides a mathematical model of the laminate. From this, knowing the physical and mechanical characteristics of the matrix and of the various layers of reinforcement with their orientation in space, it is possible to predict with good approximation the mechanical characteristics of the laminate in all its directions. However, when possible, economically and technologically, the best method to characterize the laminate is the experimental one, because it analyzes the actual laminate with all the possible imperfections of manufacturing.
The success of the final product depends not only on the quality of the matrix and reinforcement, but also on external factors, such as: the environment, the equipment used and the skill of the operator. It is not uncommon that, due to one or more of these factors, the products may exhibit inferior mechanical characteristics to those declared by the manufacturers or those calculated with the theory of lamination.
For the reasons listed above, for the purpose of this work the experimental characterization to determine the performance of the composite material used was chosen. The materials considered are:

- Epoxy resin Ampreg 21 with standard hardener;
- Carbon fiber Unidirectional 300 GSM;
- Carbon fiber 2/2 TwillWeave 200 GSM.

Three samples of each kind of laminate (250 *mm* length and 25 *mm* width) were prepared following the *AMTS-SWP-0004-A-2008* regulations for manufacture of tensile test specimens kindly provided by Gary Corderley (CSIR researcher) and the tests were made by the technicians of the *CSIR's Materials Testing Building*, placed in the same campus of ASC using a certified pull test *Istron 25 kN model 1342* machine and two strain gauges of 6 *mm* for each sample. Tabs weren't necessary, according to the experience of the technicians at the Materials Testing Building, thanks to the high grip property of the cured resin.

4.3.2 Carbon fiber unidirectional 300 GSM with epoxy Ampreg 21

These laminate specimens were made with a layup of one layer of carbon fiber unidirectional fabric 0°, cured with a cycle of 5 hours in a vacuum bag and 24 hours in ambient conditions. Data were obtained from these tests

using strain gauges, processed subsequently in a Matlab script, to get the actual properties of the material. The following graphs show the curve σ-ϵ and ϵ_{long}-ϵ_{tras} of the samples.

LAMINATE UD300GSM/AMPREG21 PROPERTIES		
Tensile strength $[MPa]$	σ_{max}	1073.40
Young's modulus $[GPa]$	E_x	82.14
Poisson's ratio	ν_{yx}	0.28
Shear modulus $[GPa]$	G_{xy}	/

Table 4.2 – *Average mechanical properties resulting from three pull tests at 0° of the specimens UD300GSM/Ampreg21.*

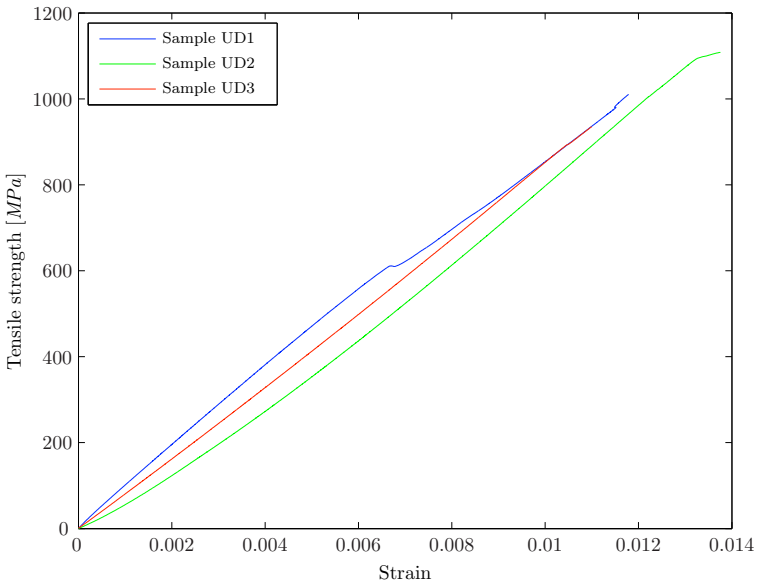

Figure 4.2 – *Matlab plot of the stress and strain curve for the three specimens UD300GSM/Ampreg21.*

The calculation of the Young's modulus and Poisson's coefficient were done following the *ASTM-D3039-00* using the average gradient of the curves in the range between 1000 $\mu\epsilon$ and 3000 $\mu\epsilon$.

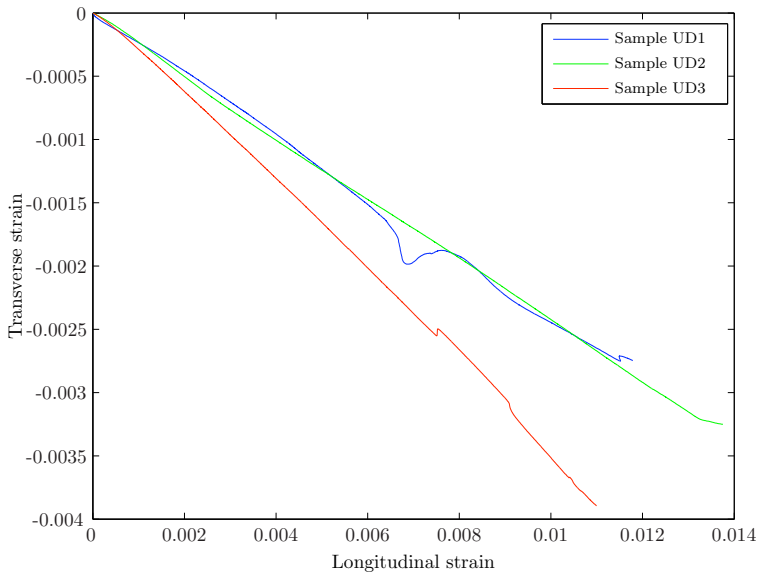

Figure 4.3 – *Matlab plot of the longitudinal strain and transversal strain curve for the three specimens UD300GSM/Ampreg21.*

Thus, elaborating these results with a mathematical average, it is possible to obtain the laminate properties as shown in the Table 4.2.

4.3.3 Carbon fiber fabric ±45 200 GSM TwillWeave with epoxy Ampreg 21

These laminate specimens were made with a layup of two layers of carbon fiber twill weave fabric ±45°, cured with a cycle of 5 hours in a vacuum bag and 24 hours in ambient conditions. Data were obtained from these tests using strain gauges, processed subsequently in a Matlab script, to get the actual properties of the material. The following graphs show the curve σ-ϵ and ϵ_{long}-ϵ_{tras} of the samples. The calculation of the Young's modulus and Poisson's coefficient were done following the *ASTM-D3039-00* using the average gradient of the curves in the range between 1000 $\mu\epsilon$ and 3000 $\mu\epsilon$.

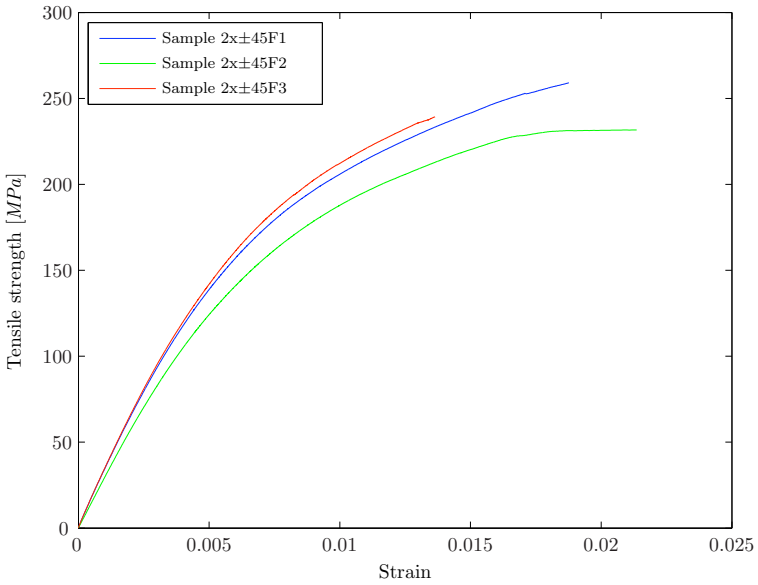

Figure 4.4 – *Matlab plot of the stress and strain curve for the three specimens ±45TW200GSM/Ampreg21.*

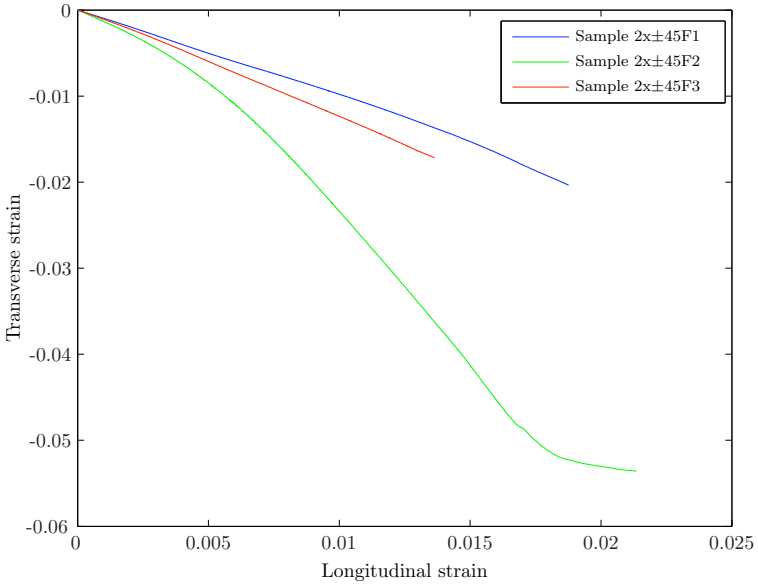

Figure 4.5 – *Matlab plot of the longitudinal strain and transversal strain curve for the three specimens ±45TW200GSM/Ampreg21.*

LAMINATE ±45TW200GSM/AMPREG21 PROPERTIES		
Tensile strength $[MPa]$	σ_{max}	249.76
Young's modulus $[GPa]$	E_x	28.65
Young's modulus $[GPa]$	E_y	28.65
Poisson's ratio	ν_{yx}	1.23
Poisson's ratio	ν_{xy}	1.23
Shear modulus $[GPa]$	G_{xy}	23.66

Table 4.3 – *Average mechanical properties resulting from three pull tests at 0° of the specimens ±45TW200GSM/Ampreg21.*

In the previous table the shear modulus was obtained using the data from the tensile test of the carbon fiber 090 200 GSM TwillWeave with epoxy Ampreg 21, due to the fact that the alignment of the fibers and the number of plies of this one corresponded to the sample cut at 45° of the ±45 200 GSM TwillWeave with epoxy Ampreg 21.

4.3.4 Carbon fiber fabric 090 200 GSM TwillWeave with epoxy Ampreg 21

These laminate specimens were made with a layup of two layers of the same previous carbon fiber twill weave fabric but at 0°/90°, cured with a cycle of 5 hours in a vacuum bag and 24 hours in ambient conditions. Data were obtained from these tests using strain gauges, processed subsequently in a Matlab script, to get the actual properties of the material. The following graphs show the curve σ-ϵ and ϵ_{long}-ϵ_{tras} of the samples.

LAMINATE 090TW200GSM/AMPREG21 PROPERTIES		
Tensile strength $[MPa]$	σ_{max}	464.22
Young's modulus $[GPa]$	E_x	48.94
Young's modulus $[GPa]$	E_y	48.94
Poisson's ratio	ν_{yx}	0.16
Poisson's ratio	ν_{xy}	0.16
Shear modulus $[GPa]$	G_{xy}	6.50

Table 4.4 – *Average mechanical properties resulting from two pull tests at 0° of the specimens 090TW200GSM/Ampreg21.*

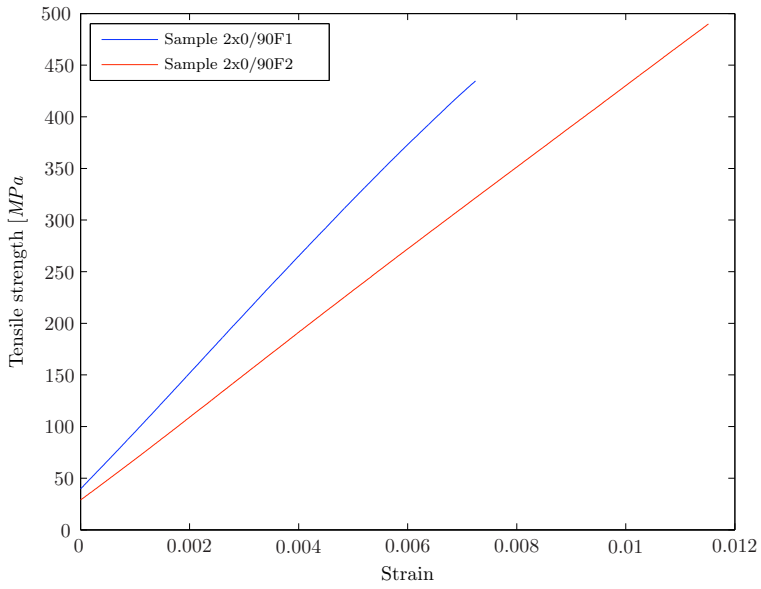

Figure 4.6 – *Matlab plot of the stress and strain curve for the two specimens 090TW200GSM/Ampreg21.*

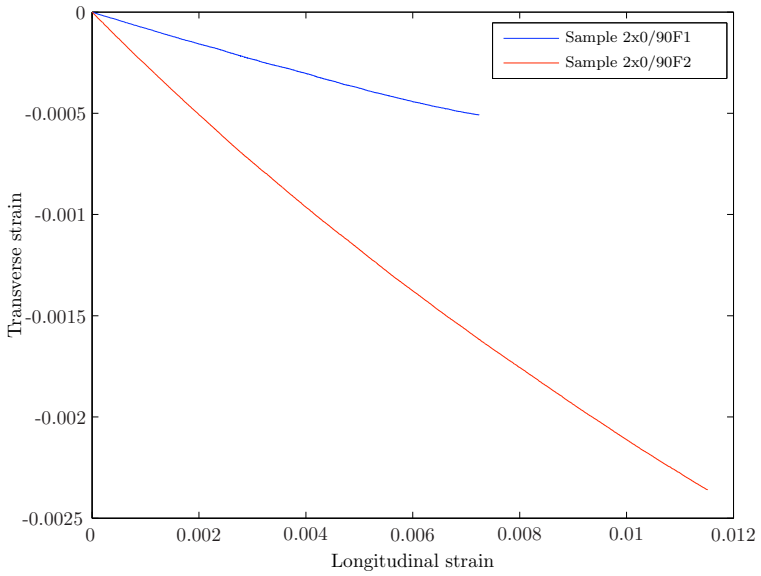

Figure 4.7 – *Matlab plot of the longitudinal strain and transversal strain curve for the two specimens 090TW200GSM/Ampreg21.*

The calculation of the Young's modulus and Poisson's coefficient were done following the *ASTM-D3039-00* using the average gradient of the curves in the range between 1000 $\mu\epsilon$ and 3000 $\mu\epsilon$. In the previous table the shear modulus was obtained using the data from the tensile test of the carbon fiber ±45 200 GSM TwillWeave with epoxy Ampreg 21, due to the fact that the alignment of the fibers and the number of plies of this one corresponded to the sample cut at 45° of the 090 200 GSM TwillWeave with epoxy Ampreg 21.

4.3.5 Carbon fiber fabric $[\pm 45/090]_2$ 200 GSM TwillWeave with epoxy Ampreg 21

These laminate specimens were made with a layup of four layers of the same previous carbon fiber twill weave fabric with a ±45° ply, two 0°/90° plies and a ±45° ply, cured with a cycle of 5 hours in a vacuum bag and 24 hours in ambient conditions. Data were obtained from these tests using strain gauges, processed subsequently in a Matlab script, to get the actual properties of the material. The following graphs show the curve σ-ϵ and ϵ_{long}-ϵ_{tras} of the samples.

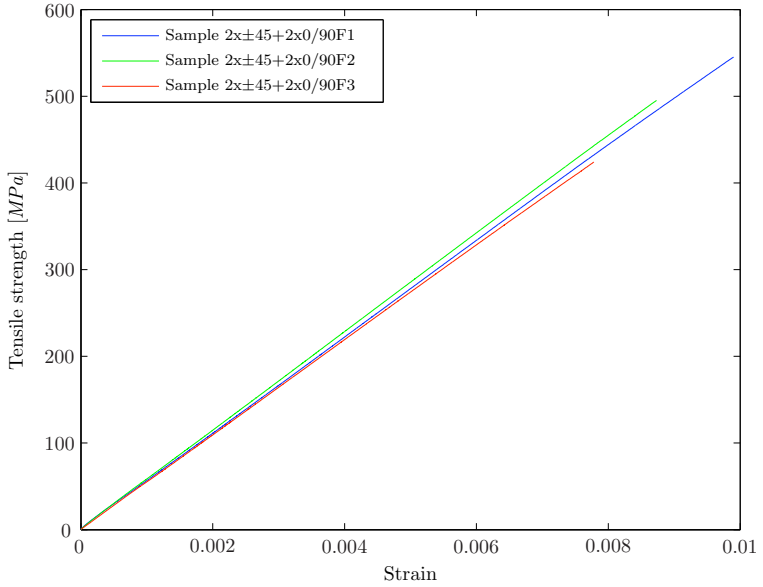

Figure 4.8 – *Matlab plot of the stress and strain curve for the three specimens* $[\pm 45/090]_2$ *TW200GSM/Ampreg21.*

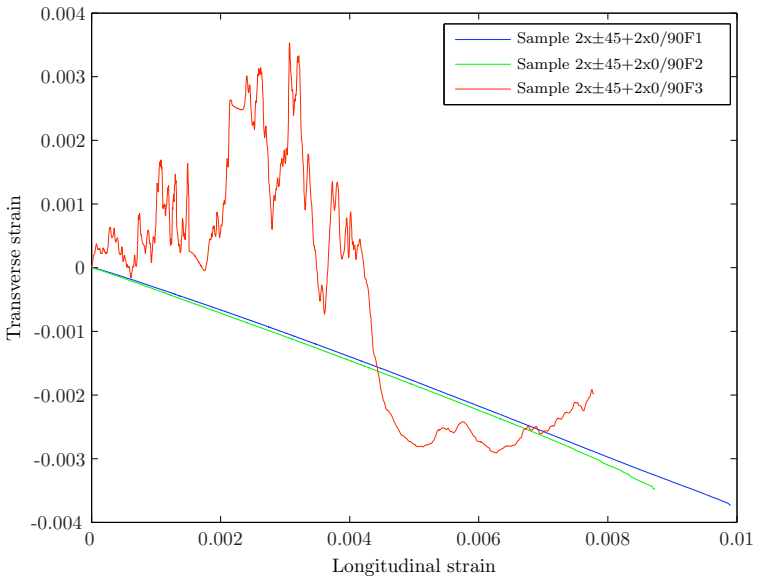

Figure 4.9 – *Matlab plot of the longitudinal strain and transversal strain curve for the three specimens [±45/090]$_2$ TW200GSM/Ampreg21.*

The calculation of the Young's modulus and Poisson's coefficient were done following the *ASTM-D3039-00* using the average gradient of the curves in the range between 1000 $\mu\epsilon$ and 3000 $\mu\epsilon$. One of these tests was affected by an electronic problem at the strain gauge and didn't provide useful data, as seen by the red curve of the previous figure.

LAMINATE [±45/090]$_2$TW200GSM/AMPREG21 PROPERTIES		
Tensile strength $[MPa]$	σ_{max}	492.19
Young's modulus $[GPa]$	E_x	54.42
Young's modulus $[GPa]$	E_y	54.42
Poisson's ratio	ν_{yx}	0.36
Poisson's ratio	ν_{xy}	0.36
Shear modulus $[GPa]$	G_{xy}	20.47

Table 4.5 – *Average mechanical properties resulting from three pull tests at 0° of the specimens [±45/090]$_2$ TW200GSM/Ampreg21.*

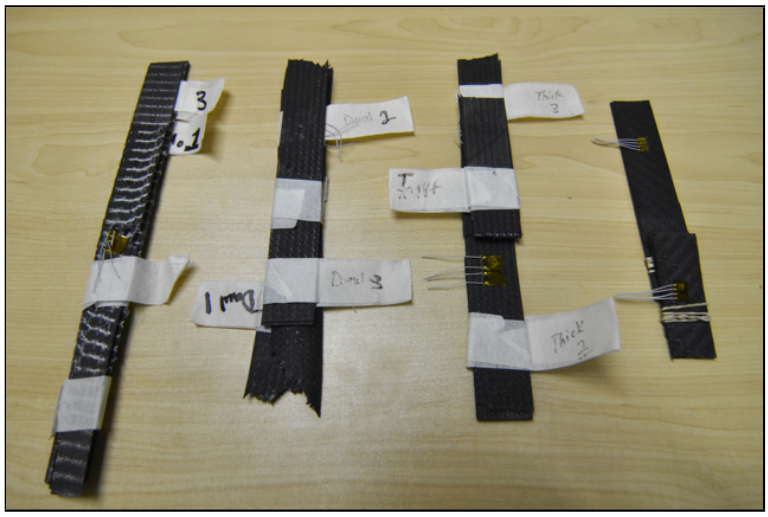

Figure 4.10 – *Specimens made for the tensile tests.*

Chapter 5

Structural design of a new wing for the Modular UAS

5.1 Design overview of the new wing structure

General guidelines on the structural design of the new wing were given by John Monk, in particular for the junction of the wing with the fuselage and the central wing. Which, for the purpose of the Modular UAS concept, must be the same as the original configuration. This sets a limit to the design of the structure because use of a rear spar cannot be considered. Due to the fact that the interface holes in the fuselage must remain the same, only the main spar can pass through the junction. Thus the classic torque box cannot be designed. For this reason, in order to develop an optimised composite lay-up scheme for the new wing that is structurally capable of withstanding the predicted distributed loads, a consideration on the different elements that constitute the structure is needed [16]. The spar is designed to resist the bending moment of the wing and to increase the critical load of the skin caused by buckling phenomena. The ribs are necessary to maintain the shape of the airfoil and to distribute the distributed and concentrated loads (i.e. the aileron and flap hinge forces). The skin is necessary to resist to the shear force and the torque moment (as in a torque box) [16]. This consideration will be helpful to identify a best composite configuration to optimize the structure to be as light as possible.

5.2 Single components design and manufacturing overview

5.2.1 The spar

Several kinds of spar sections could be selected, i.e., circular, rectangular or C-shape. The circular one was excluded to avoid bonding problems with the ribs and the skin. Even though the torque stiffness of this kind of spar is very high because of the circular shape, the torque moment can't be transfered safely from the ribs to the spar considering that the bonding line has to carry all the torque load. Modifying the spar in order to eliminate this rotation, makes the structural design excessively complex. A torque box is necessary, and without a rear spar also the C-section spar cannot be considered, even if it is a light and efficient solution. Thus, to close a stiff torque box in the wing section a rectangular spar, with two separate elements, i.e. the spar caps and the spar webs, was considered. Due to its high maximum tensile strength and elastic modulus the unidirectional 300 GSM carbon fiber was chosen for the top and bottom surfaces of the rectangular spar, being able to absorb the normal stress given by the bending moment applied on the wing structure.

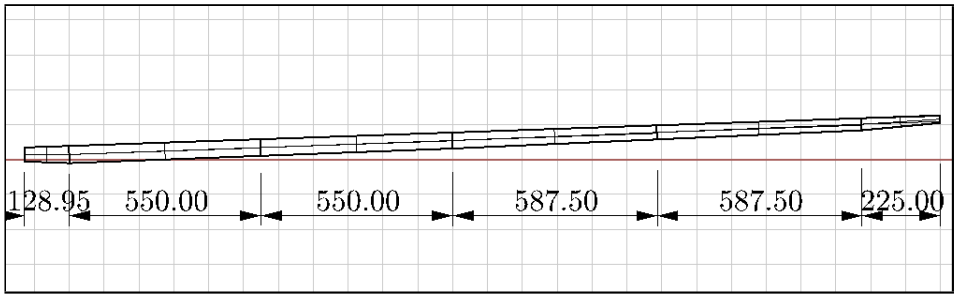

Figure 5.1 – *Modular UAS's spar front view generated with Rhinoceros 4.0 (dimensions in millimeters).*

Because the bending moment is not constant along the wing span, it is desirable not to waste materials and add additional weight where not necessary. In this case, referring to Figure , the idea is to reduce the layers of the spar caps from 5 to 1 along the span, decreasing from the root to the tip one layer of UD 300 GSM at each rib. On the other hand, for the spar webs it is not possible to consider a size reduction along the wing span because the shear flow is not expected to be very high and just one single

carbon fiber braided sleeve has been considered as a possible structural solution for the torque box, working together with the D-box of the leading edge of the wing. A foam mold can be used to layup the carbon fiber UD 300 GSM strips as spar caps, and the single carbon fiber braided sleeve $\pm 45°$ as spar webs. The ASC's workshop has a foam cutting machine that can be used for this purpose, which cuts pieces of maximum 60 *cm* length. This distance can be considered as limit for the spar mold pieces length (to bond together afterwards). Thus, the idea is to cut the spar mold foam in pieces as long as the ribs distance, then bond them together using a scale 1:1 CAD printout as angle reference.

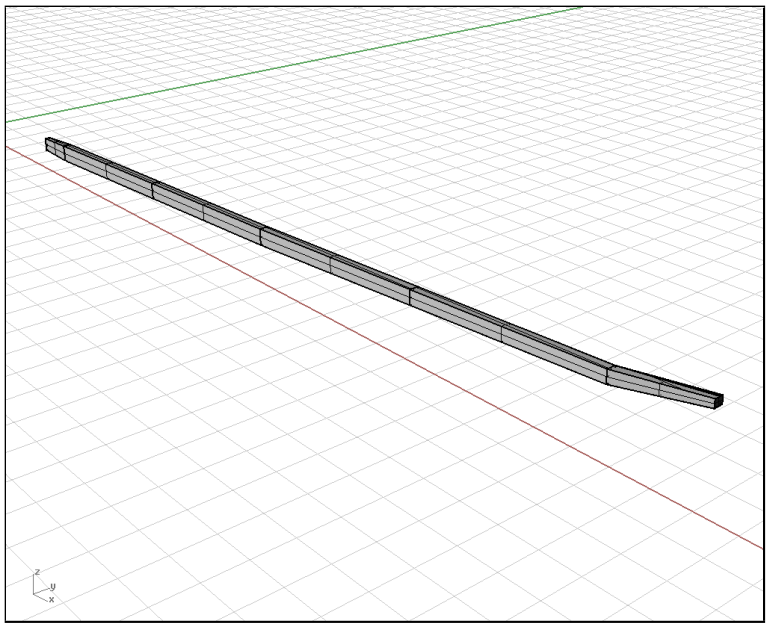

Figure 5.2 – *Modular UAS's spar view generated with Rhinoceros 4.0.*

5.2.2 The ribs

To have characteristics of stiffness and lightness, carbon fiber ribs were designed. Due to the aspected low shear flow, it is not useful to have thick ribs.

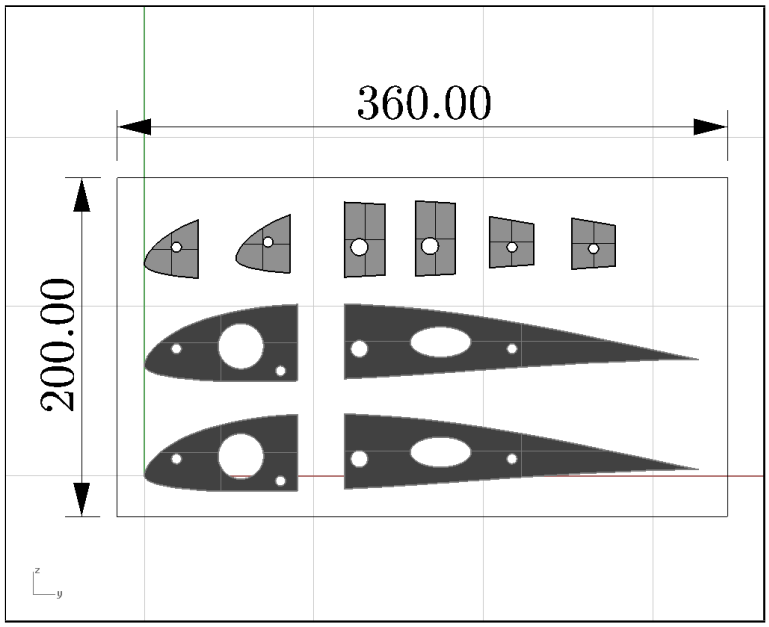

Figure 5.3 – *Modular UAS's fiber glass root rib and pin supports view generated with Rhinoceros 4.0 (dimensions in millimeters).*

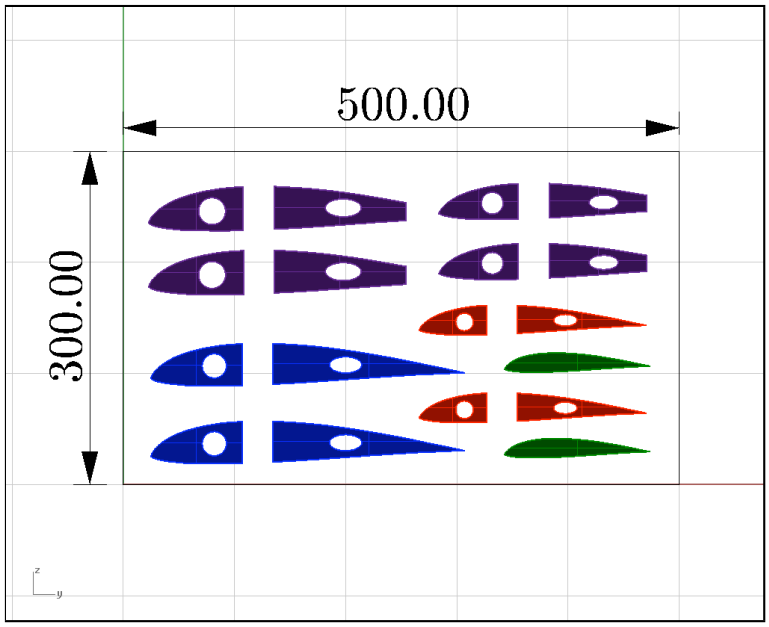

Figure 5.4 – *Modular UAS's carbon fibers ribs view generated with Rhinoceros 4.0.*

The bonding line with the skin plays an important role on the structure, thus, to increase the thickness of the ribs to guarantee sufficient bonding surface without increasing the weight, a composite sandwich solution with two layers of carbon fiber fabric ±45° per side and a foam sandwich core of 2 *mm* was considered. This permits to have at least a 3 *mm* wide of bonding surface for the ribs, being the thickness of the carbon fiber fabric dry more or less 0.22 *mm* plus 2 *mm* of foam [21]. The layup configuration was done looking at the highest possible shear modulus G_{xy}. The exception was the root rib, which needs to host the pins of the fuselage junction. Firstly because of the galvanic corrosion which affects carbon fiber joined with steel, and secondly because of dangerous crack generated by the sharp edges of the head of the screws placed directly on the rib, a full 3 *mm* fiber glass rib plus small pin supports around the holes were used (thus the head of the screws touched the supports, not straight the rib). Every rib needs holes to provide passages for the servo wires.

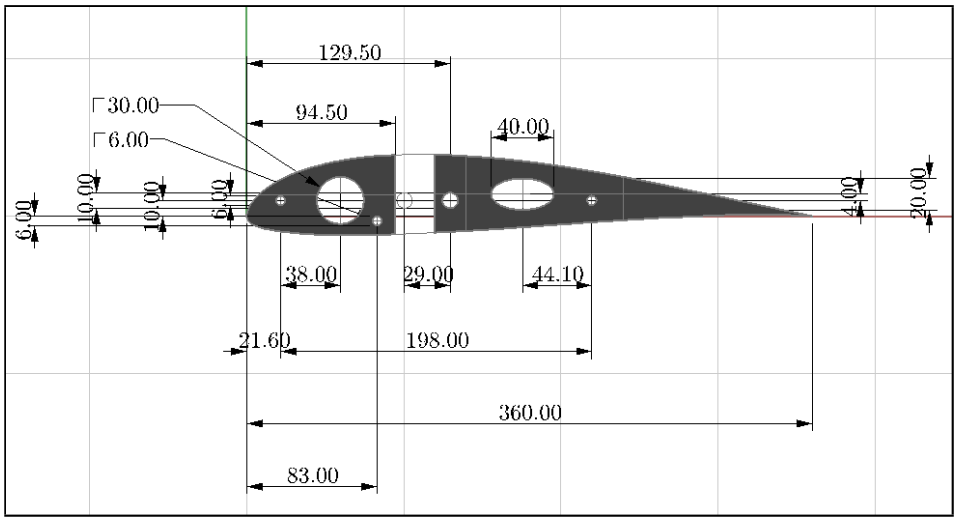

Figure 5.5 – *Modular UAS's root rib lateral view generated with Rhinoceros 4.0 (dimensions in millimeters).*

A minimal configuration, was considered:

- the root rib (y=0 *mm*), which also closes the inner cutting line of the flap;
- a half rib in the middle of flap length (y=550 *mm*) to guarantee enough stiffness at the skin where the hinge and the servo of the flap are placed;

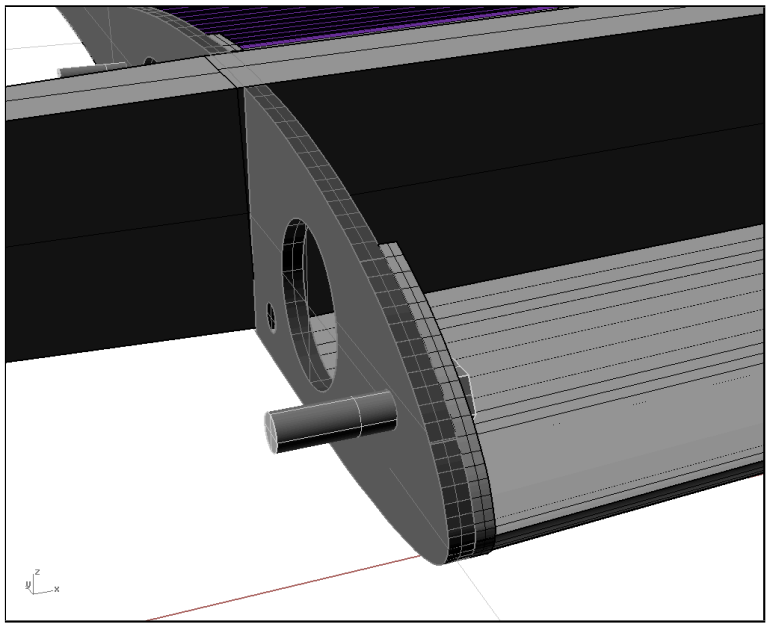

Figure 5.6 – *Modular UAS's root rib view generated with Rhinoceros 4.0.*

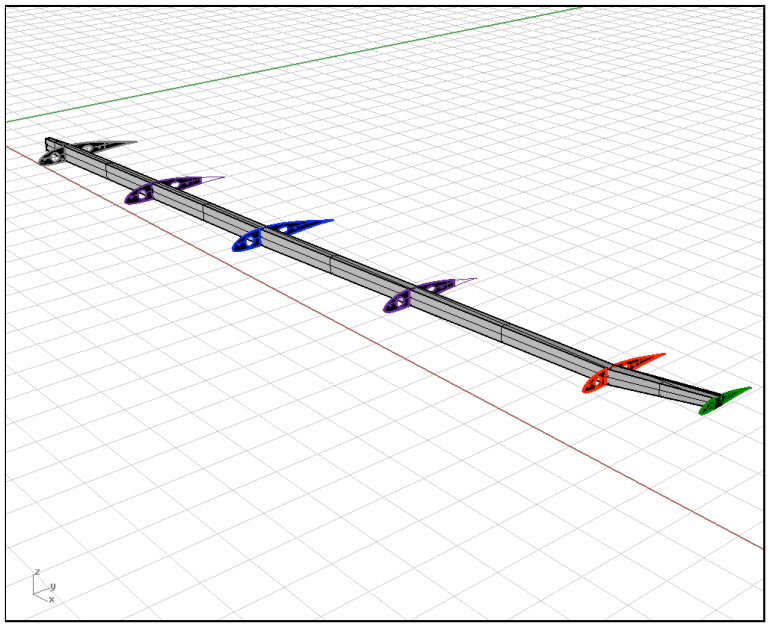

Figure 5.7 – *Modular UAS's main structure view generated with Rhinoceros 4.0.*

- one rib where the wing section changes (y=1100 mm), which also closes the outer cutting line line of the flap and the inner cutting line of the aileron;
- a half rib in the middle of aileron length (y=1687.5 mm) to guarantee enough stiffness at the skin where the hinge and the servo of the aileron are placed;
- one rib where the wing section changes (y=2275 mm), which also closes the outer cutting line line of the aileron;
- one rib at the tip (y=2500 mm).

In the next chapter the stress condition resulting from the loads applied on each rib will be verified. The actual manufacture of the ribs was ordered from Lightweight Structure Technology L.t.d. based in Pretoria (South Africa). This because they can also provide NC mechanical cutting, and the CAD used to manufacture the rib are shown in Figure 5.3 and 5.4.

5.2.3 The skin

Following the suggestion of John Monk, the skin of the new wing must be stiff not just because of the external loads but also to prevent damage during handling and transportation of the wing, being a prototype demonstrative solution for the Modular UAS. Thus, a sandwich solution was considered. In particular, one possible optimized layup can be made with two plies of carbon fiber fabric $\pm 45°$ per side and a foam sandwich core of 2 mm, for a total thickness of 3 mm. This provides a big increase of the local bending stiffness of the skin, keeping the structure working in an optimized way for both shear force and torque moment [16]. One additional small layer of carbon fiber fabric, placed at $0°/90°$, was designed for the areas where the two holes for the control surfaces servos are located. This permits a better redistribution of the stresses around the hole itself [9]. To obtain a good finish quality of the surface, a single thin ply of fiber glass 20 g/m^2 was used. The foam core was stopped near the leading and trailing edges, with its cutting edge sanded to at least 45° to ensure a smooth path for the carbon fabrics. It was also stopped where the spar is placed, getting all the carbon plies cured together along the spar width. The same consideration was done for the aileron and flap cutting lines. All the layup was done using an open mold, manufactured by Lightweight Structure Technology L.t.d., curing everything for at least 5 hours in a vacuum bag and 24 hours at ambient conditions.

5.2.4 The joining with the Modular UAS

The original junction with the fuselage and the central wing is composed by: one steal pin 10 *mm* diameter inserted into the main spar, which goes into a hole located on the central wing root rib; a similar steal pin coming from the main spar of the central wing which goes into a hole located on the half wing root rib; two steal screws 6 *mm* diameter bonded on the root rib of the wing which are screwed to the fuselage with nuts. As the RGL John Monk suggests, this kind of junction must be the same for the new wing design, considering the modular concept of the aircraft.

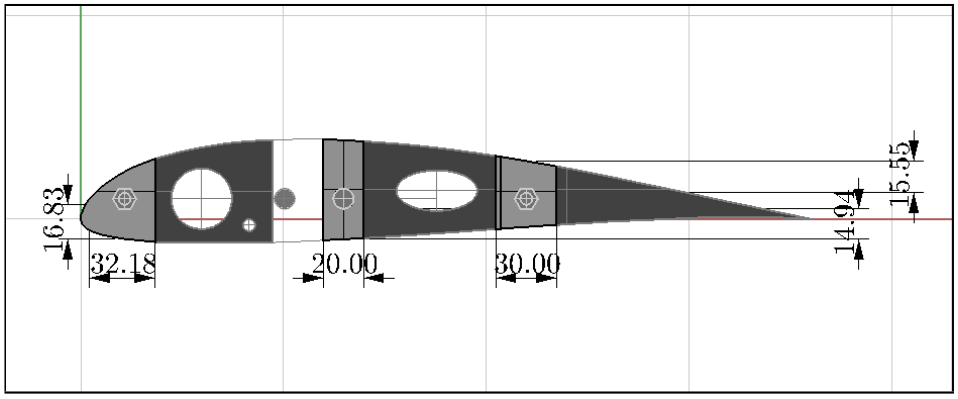

Figure 5.8 – *Modular UAS's root rib supports lateral view generated with Rhinoceros 4.0 (dimensions in millimeters).*

Thus, the purpose of this work is to design the means by which the junction can withstand the loads applied to the wing. With regards to the M6 screws, they were designed to carry the shear force and the torque moment seen at the root, and the M10 pins the bending moment. Due to this, the root rib needs small fiberglass pin supports around the M6 holes, supposedly 3 *mm* thick, this also seems to prevent small cracks generation at the root rib. The same consideration is done for the M10 pin going into the root rib hole, which experiences high shear load. A fiber glass or tufnol piece was considered to be bonded in the inner face of the root rib (Figure 5.3). With regards to the M10 pin bonded into the main spar, a full tufnol block (for the last 60 *mm* of the spar length) was needed, instead of the foam spar mold, to transfer the bending moment of the spar experienced at the root to the central wing root rib with the 10 *mm* pin itself.

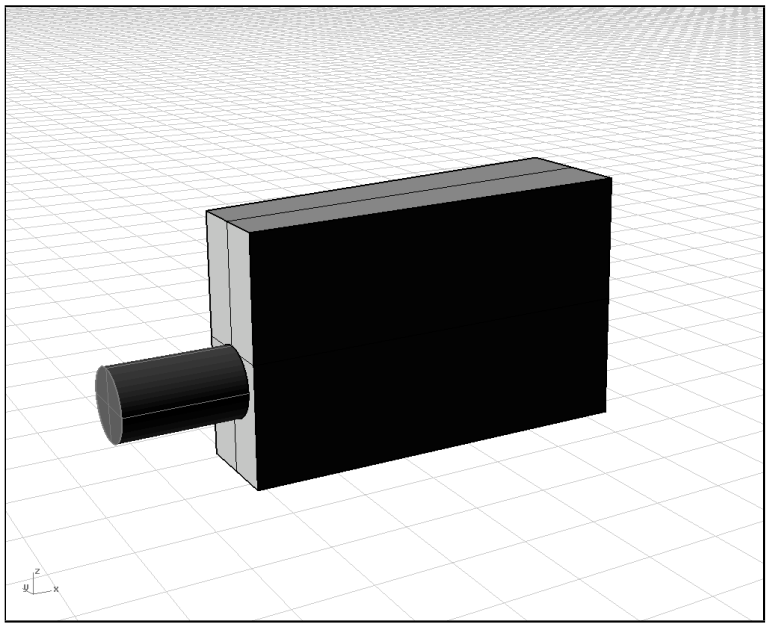

Figure 5.9 – *Spar tufnol component view generated with Rhinoceros 4.0.*

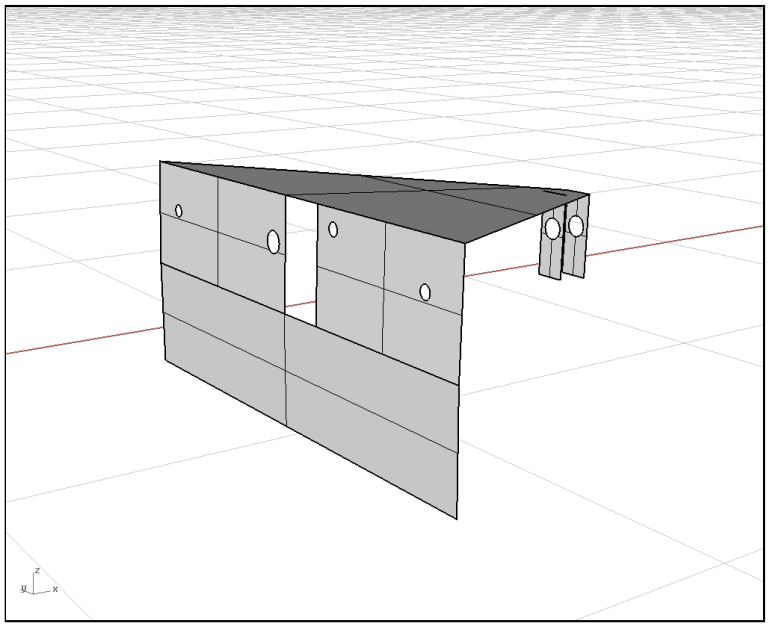

Figure 5.10 – *Alignment metal support view generated with Rhinoceros 4.0.*

Transfer the bending is impossible while keeping the foam (i.e. the spar mold) as structural component. This tufnol support (Figure 5.9) was ordered from Lightweight Structure Technology L.d.t. with the other fiber glass holes supports as seen in Figure 5.3. Because of the dihedral of the new wing, the alignment of the components at the root is essential to obtain a good product. To solve this a metal support was designed, which has the proper angle to align the root rib, the spar and the pin at the same time. As shown in Figure 7.13, the four holes are necessary to screw the root rib at the support with the proper angle, the big rectangular section hole is used to align the spar and the small rectangular plates used to place the 10 *mm* pin in its position. This component was ordered from the technicians of the CSIR's Building 12c.

5.2.5 Complete wing CAD design

In the following figures the resulting complete CAD, made with Rhinoceros 4.0 and including all the components mentioned before, is shown. This CAD was used to order all the commissioned parts and to estimate the quantity and type of materials necessary for the layup of the complete wing structure.

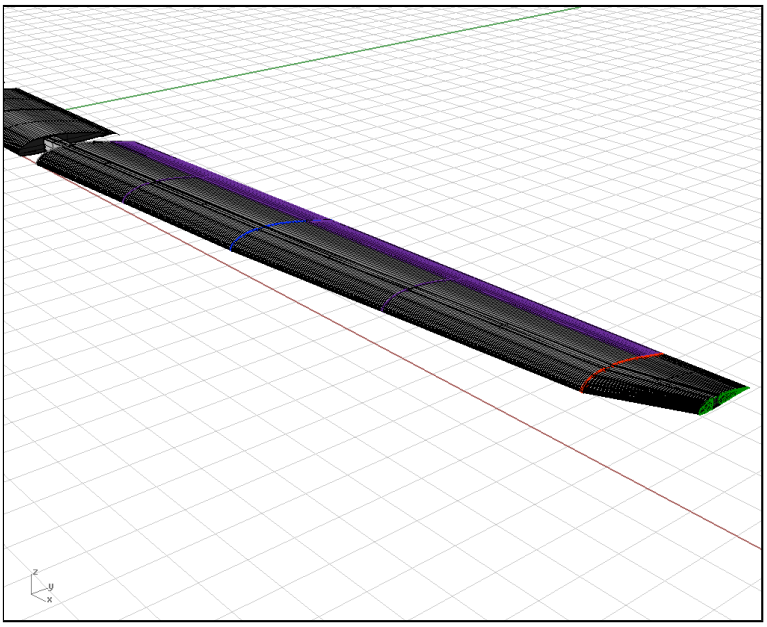

Figure 5.11 – *Modular UAS's complete wing view generated with Rhinoceros 4.0.*

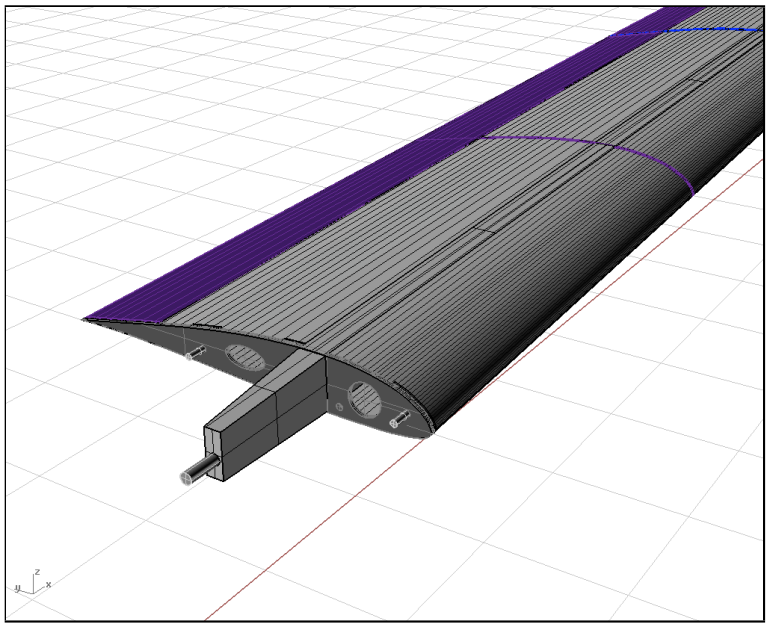

Figure 5.12 – *Modular UAS's complete wing view generated with Rhinoceros 4.0.*

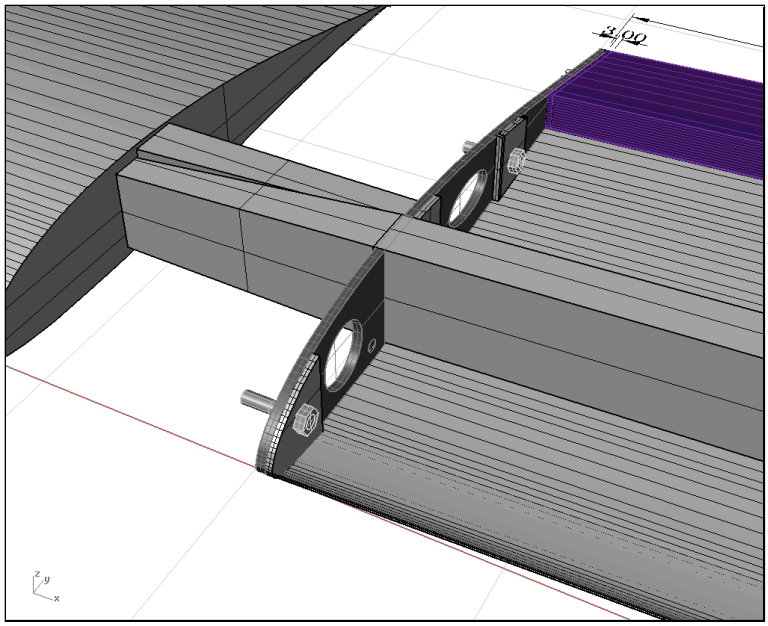

Figure 5.13 – *Modular UAS's complete wing and central wing view generated with Rhinoceros 4.0 (particular of the junction, without the top skin).*

Chapter 6

Structural analysis of the new wing solution

6.1 Semi-monocoque analysis

6.1.1 Introduction

Semi-monocoque are structures with stiffening members which support normal stress and panels which support shear flow. This is a more efficient type of construction that permits much thinner covering shell, and is the usual kind of construction implemented in aeronautical applications. As mentioned in the previous chapter, some assumptions have to be made, depending on the structural component considered.
The spar [16]:

- resists bending and axial loads;
- forms the wing box for torsional resistance.

The ribs and frames [16]:

- introduce external loads, distributed as well as concentrated, in the main structure;
- keep the aerodynamic profile of the wing.

The skin [16]:

- resists torsion and shear loads;

- transmits aerodynamic forces to the longitudinal and transverse supporting members;
- acts with the longitudinal members in resisting the applied bending and axial loads;
- acts with the transverse members in reacting the load due to pressurization.

The stiffener or stringers [16]:

- resist bending and axial loads;
- divide the skin into small panels and thereby increase its buckling and failing stresses;
- act with the skin in resisting axial loads caused by pressurization.

These considerations are necessary to do the simplifications that semi-monocoque theory uses. Thus, the behavior of these structural elements is often idealized to simplify the analysis of the assembled components as following:

- the longitudinal elements carry only axial stress;
- the webs (skin and spar webs) carry only shearing stresses;
- the transverse frames and ribs are rigid within their own planes, so that the cross section is unchanged during loading.

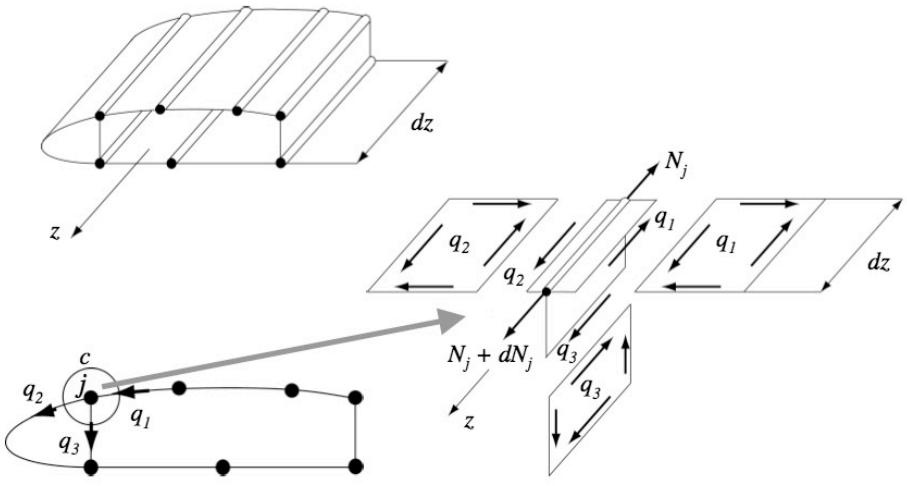

Figure 6.1 – *Application of the semi-monocoque theory to a wing section [16].*

6.1.2 Analysis of the root wing section (2.5 m from the tip)

The first semi-monocoque analysis was done at the root wing section, to verify the stress condition in the section which has the highest internal applied load, using the results from the Chapter 3. All these calculations were done with Matlab (see Appendix A.3.2).

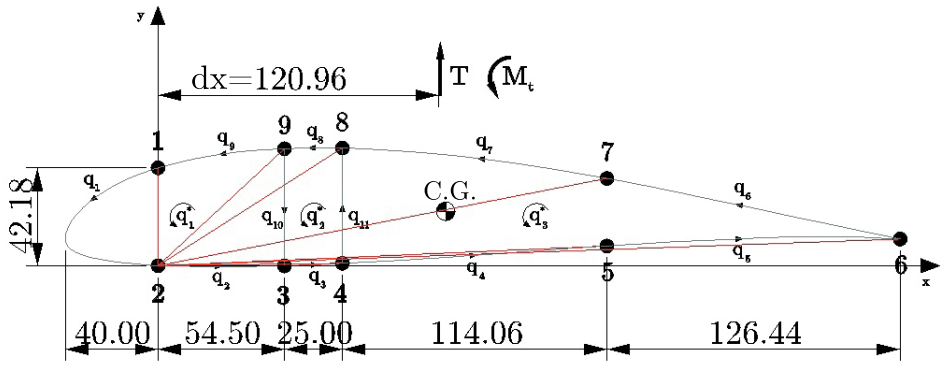

Figure 6.2 – *Semimonocoque discretization for the root wing section.*

The distribution of normal stress in the panels has an important effect on shear stress distribution. In fact, according to the shear flow equation, if a panel carries normal stresses, the shear flow varies along the panel [16]. As far as the normal stress is concerned, the area of the panels can be considered concentrated at lumped stations. Such stations can coincide with existing stringers (stringer area is increased) or dummy stringers can be introduced [17]. Thus, the reduction of a section to a semi-monocoque analysis is not unique: the assumption that the area of the panels is concentrated in the neighboring stiffeners is expressed by [16]:

$$A_i = A_{S_i} + \sum_{i=1}^{n} \frac{l_{p_i} t_{p_i}}{2} \alpha_i \tag{6.1}$$

where A_{S_i} is the stiffener area, l_p is the length of the panel, t_p is the thickness of the panel and α_i is a coefficient that is equal to zero when the panel is not linked to the stiffener, and is equal to one when it is. For a given section

the center of gravity coordinates must be calculated as follows [16]:

$$X_{CG} = \frac{S_y}{A_{tot}} = \frac{\sum_{j=1}^{n} A_j X_j}{\sum_{j=1}^{n} A_j} = 124.560 \ mm \tag{6.2}$$

$$Y_{CG} = \frac{S_x}{A_{tot}} = \frac{\sum_{j=1}^{n} A_j Y_j}{\sum_{j=1}^{n} A_j} = 22.316 \ mm \tag{6.3}$$

where X_j and Y_j represent respectively the x and y stringer j concentrated area coordinates referred to the original frame of reference (placed on stiffener number 2 in Figure 6.2). Second moments of area and the product of inertia (calculated respect to the center of gravity coordinates) of the discretized section are [16]:

$$I_x = \sum_{j=1}^{n} A_j y_j^2 = 394950 \ mm^4 \tag{6.4}$$

$$I_y = \sum_{j=1}^{n} A_j x_j^2 = 9724400 \ mm^4 \tag{6.5}$$

$$I_{xy} = \sum_{j=1}^{n} A_j x_i y_j = -307610 \ mm^4 \tag{6.6}$$

$$\alpha = \frac{1}{2} \arctan\left(\frac{2I_{xy}}{I_y - I_x}\right) = -0.0329 \ rad \tag{6.7}$$

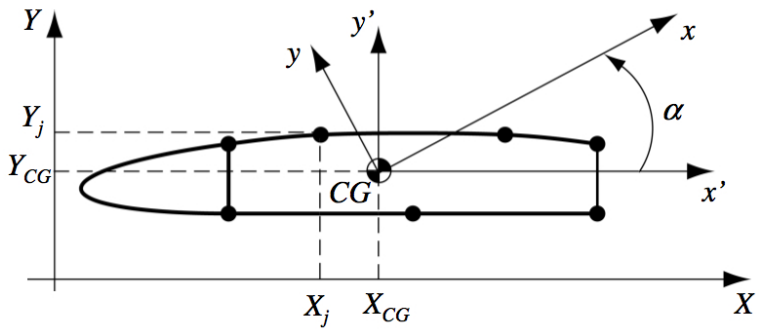

Figure 6.3 – *Frames of reference [16].*

which means that for this section the centroidal axes can be approximated to the frame of reference centered in the center of gravity. The general bending stress equation for elastic, homogeneous beams is [16]:

$$\sigma_j = \frac{N}{\sum_{j=1}^{n} A_j} + \frac{M_x}{I_x} y_j - \frac{M_y}{I_y} x_j \tag{6.8}$$

where M_x and M_y are respectively the bending moments about the x and y centroidal axes. I_x and I_y are respectively the second moments of area calculated as before, about the x and y axes, and I_{xy} is the product of inertia. Using this equation it is possible to calculate the bending stress at any point on the beam cross section regardless of moment orientation or cross-sectional shape. Note that I_x, I_y, and I_{xy} are all unique for a given section along the length of the beam. In other words, they will not change from one point to another on the cross section (if the cross section does not vary). However, the x and y variables shown in the equation correspond to the coordinates of a point on the cross section at which the stress is to be determined. The stiffeners carry the entire bending-induced normal stresses, while the webs carry the entire shear flow and corresponding shear stresses. Thus, a web does not change the shear flow between two adjacent stiffeners and as such would be in the state of constant shear flow which means that if a closed contour is considered, which does not encompass a stringer (real or dummy) the neat shear flow must be zero: in-flow and out-flow must be equal and q is constant along the panel. The equation that

describes the shear flow, for an open shell, is [17]:

$$\Delta q_j = -\frac{T_y}{I_x} S_{x_j} - \frac{T_x}{I_y} S_{y_j} \tag{6.9}$$

Moreover, shear flow equation can not completely describe the shear flow in a closed section where a circular shear flow can exist. Such circular shear flow cannot be taken into account by the shear flow equation, because for each closed boundary the ingoing flow will be equal to the outgoing one. The contribution of a circular shear flow in the shear flow equation is always zero. The two previous considerations allows the definition of a solution procedure for closed sections. According to the balance of equations and unknowns, an equation is missing. Such an equation is clearly the equivalence of the moment that is generated by the flow system with the moment of the internal forces, which are applied to the section.

$$\begin{gathered} M_o = \sum_{i=1}^{m} 2\Omega_{i,o} q_i \beta_{i,o} = \sum_{k=1}^{N} 2\Omega_k q_k^* \beta_{k,o} + \sum_{i=1}^{m} 2\Omega_{i,o} q_i' \beta_{i,o} \\ i = 1, \ldots, m \\ k = 1, \ldots, N \\ \beta_{i,o} = \pm 1 \\ \beta_{k,o} = \pm 1 \end{gathered} \tag{6.10}$$

where shear flows in the section can be considered the superposition of a circular flow plus a dummy solution [17]:

$$\begin{gathered} q_i = q_i' + \sum_{k=1}^{N} q_k^* \alpha_{ik} \\ i = 1, \ldots, m \\ k = 1, \ldots, N \end{gathered} \tag{6.11}$$

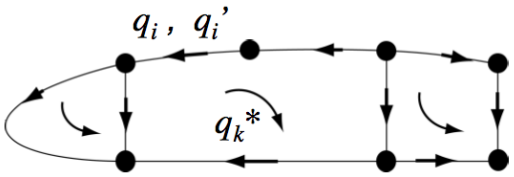

Figure 6.4 – *Shear flow contribution consists of the circular flow and the dummy solution [16].*

For a closed multi-connected section, the compatibility of twist needs to be introduced; the imposed compatibility refers to the constraint represented by the frame. In fact the section does not undergo distortion. Each loop must rotate by the same quantity [17]. This set of equations closes the mathematical solution of the problem.

$$\begin{gathered}\frac{d\theta_k}{dz} = \frac{1}{2\Omega_k}\sum_{i\in k}\frac{q_i l_i}{G_i t_i}\beta ik \\ i = 1,\ldots,m \\ k = 1,\ldots,N\end{gathered} \tag{6.12}$$

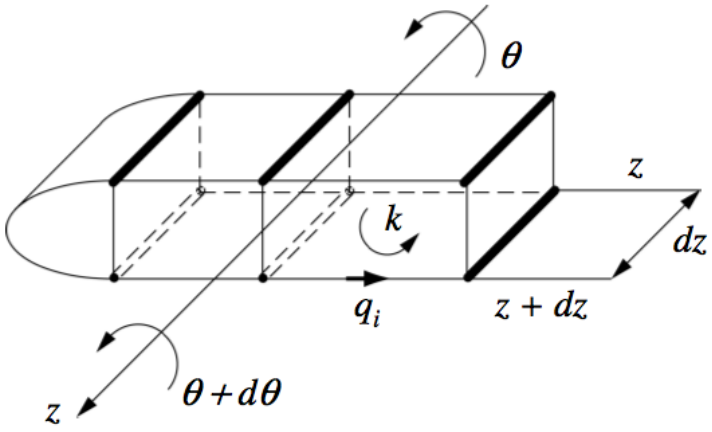

Figure 6.5 – *Imposed compatibility of the torsion angle of the cells [16].*

A multi-connected section will have a shear center, whose definition is

identical to the case of single-cell sections; if the line of action of the force passes through the *shear center* of the beam section, then the beam will only bend without any twist. Otherwise, twist will accompany bending. The shear center is in fact the centroid of the internal shear force system. Depending on the beam's cross-sectional shape along its length, the location of shear center may vary from section to section. A line connecting all the shear centers is called the *elastic axis* of the beam. When a beam is under the action of a more general lateral load system, than to prevent the beam from twisting, the load must be centered along the elastic axis of the beam. This is important for defining where the the shear force must be applied not to generate an unexpected torque moment in the analysis and in the structural test. The coordinates of the shear center does not depend on the value of the forces. Hence, calculations can be performed considering a unit shear force [16]. The procedure for the evaluation of the shear center in a multi-connected section is to apply a unit shear in the vertical (for x_{sc}) or horizontal (for y_{sc}) direction at an unknown distance from axes origin, then evaluate the shear flows in the open-walk section. With the moment equivalence and the expression of the torsions for all the closed loops equal to zero, it is possible to solve the system and get the shear center distance of the section, i.e. in this case [16]:

$$\begin{aligned} \frac{d\theta_k}{dz} = \frac{1}{2\Omega_k} \sum_{i \in k} \frac{q_i l_i}{G_i t_i} \beta ik = 0 \\ i = 1, \ldots, m \\ k = 1, \ldots, N \end{aligned} \tag{6.13}$$

and

$$\begin{aligned} x_{sc} = \sum_{k=1}^{N} 2\Omega_k q_k^* \beta_{k,o} + \sum_{i=1}^{m} 2\Omega_{i,o} q_i' \beta_{i,o} = 120.965 \ mm \\ i = 1, \ldots, m \\ k = 1, \ldots, N \end{aligned} \tag{6.14}$$

and with an analogous system, the evaluation of y_{sc} equals to 30.08 mm. Thus, the position of the shear center along the chord of the wing section can be considered at 44.71% of the chord length from the leading edge. Implementing the previous equations using all the geometric data from CAD, one can obtain the normal stress in the stiffeners (dummy or real) and

the shear stress in the panels. The results from the semimonocoque discretization made for this wing section are shown in the next table with the corresponding margin of safety:

NORMAL STRESS [MPa]	**MARGIN OF SAFETY**
$\sigma_1 = -113.871$	$MS_{\sigma_1} = 75.47\%$
$\sigma_2 = 127.924$	$MS_{\sigma_2} = 95.24\%$
$\sigma_3 = 128.383$	$MS_{\sigma_3} = 736.09\%$
$\sigma_4 = 121.848$	$MS_{\sigma_4} = 780.93\%$
$\sigma_5 = 79.141$	$MS_{\sigma_5} = 215.59\%$
$\sigma_6 = 62.001$	$MS_{\sigma_6} = 302.84\%$
$\sigma_7 = -87.788$	$MS_{\sigma_7} = 127.61\%$
$\sigma_8 = -162.941$	$MS_{\sigma_8} = 427.01\%$
$\sigma_9 = -160.935$	$MS_{\sigma_9} = 433.58\%$

Table 6.1 – *Normal stress in the stiffeners at the root wing section and corresponding margin of safety. The loads include safety factors.*

SHEAR STRESS [MPa]	**MARGIN OF SAFETY**
$\tau_1 = -16.124$	$MS_{\tau_1} = 674.48\%$
$\tau_2 = -7.744$	$MS_{\tau_2} = 1512.60\%$
$\tau_3 = -6.866$	$MS_{\tau_3} = 1718.90\%$
$\tau_4 = -10.161$	$MS_{\tau_4} = 1129.10\%$
$\tau_5 = -1.896$	$MS_{\tau_5} = 6487.30\%$
$\tau_6 = 4.977$	$MS_{\tau_6} = 2409.20\%$
$\tau_7 = -4.311$	$MS_{\tau_7} = 2796.80\%$
$\tau_8 = -5.843$	$MS_{\tau_8} = 2037.20\%$
$\tau_9 = -8.627$	$MS_{\tau_9} = 1347.60\%$
$\tau_{10} = -21.625$	$MS_{\tau_{10}} = 477.48\%$
$\tau_{11} = 19.247$	$MS_{\tau_{11}} = 548.82\%$

Table 6.2 – *Shear stress in the panels at the root wing section and corresponding margin of safety. The loads include safety factors.*

where the shear stress is obtained from the shear flow in the panel di-

vided by the thickness of the panel itself [16]:

$$\tau_i = \frac{q_i}{t_i} \tag{6.15}$$

and the margin of safety was calculated as:

$$\begin{aligned} MS_{\%_j} &= \left(\frac{\sigma_{max}}{\sigma_j} - 1\right)100 \\ MS_{\%_i} &= \left(\frac{\tau_{max}}{\tau_i} - 1\right)100 \end{aligned} \tag{6.16}$$

All the resulting stresses include safety factors applied previously to the loads evaluated in Chapter 3; a reduction factor of 0.8 was considered in the case of compression for the normal stresses. It is possible to see from these tables, especially for the shear stresses, that the margins of safety are very high. This is due to two reasons: firstly because there is a technological limit in the composite structure, for which the thickness cannot be lower than a certain limit. Using for example only one ply, during the cutting phase and the layup, the fibers could move and create empty spaces between them, or even leave pockets with not enough resin. Secondly because the RGL John Monk asked for a prototype wing, stiff enough to be carried and handled without the possibility of causing critical damage to itself; This explains why two plies for each side of the sandwich skin where used, which results in an oversized structure.

6.1.3 Analysis of the root rib (2.5 m from the tip)

The distributed loads are introduced in the beam structure by ribs, even if they act on panels that belong to the semi-monocoque structure and this means that a continuous load distribution is actually introduced as discrete, concentrated forces, at rib locations. The knowledge of the semi-monocoque scheme of the section, which is reinforced by the rib, allows the evaluation of the equilibrating shear flow distribution, thus a self-equilibrating system acting on the rib can be evaluated. The evaluation of the equilibrating flow can be done considering the resultant of the external force systems: this can be done because the transversal element (rib) is considered infinitely rigid in its plane and the load redistribution only depends on semi-monocoque section properties [17]. The rib is formed by two parts, one in front and the

other at the rear of the spar at which they are bonded. The angles β_1 and β_2, shown in the following figure, indicate the local tangent to the profile of the rib at the front spar web position.

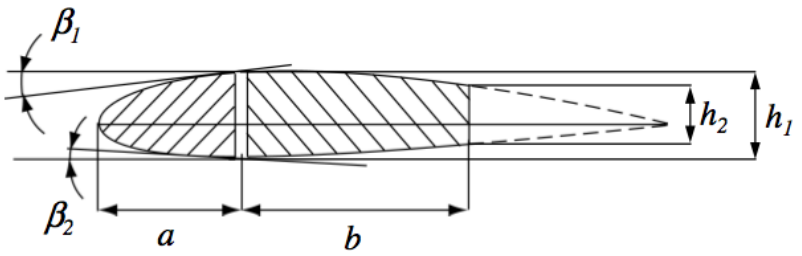

Figure 6.6 – *Rib simplification scheme [16].*

With the semi-monocoque analysis of the wing section the equivalent shear flows in the panels was determined. To obtain the balancing shear flows, which are the flows actually acting on the rib, the shear flow on the wing section needs to be changed in direction, maintaining unchanged the value. The resulting internal loads such as shear force, normal force and moment up to a the distance a from the leading edge were calculated in order to obtain the force acting on the stiffeners of the rib:

$$\begin{aligned} P_{1_x} &= \frac{M}{h_1} + \frac{N}{2} \\ P_{2_x} &= \frac{M}{h_1} - \frac{N}{2} \end{aligned} \tag{6.17}$$

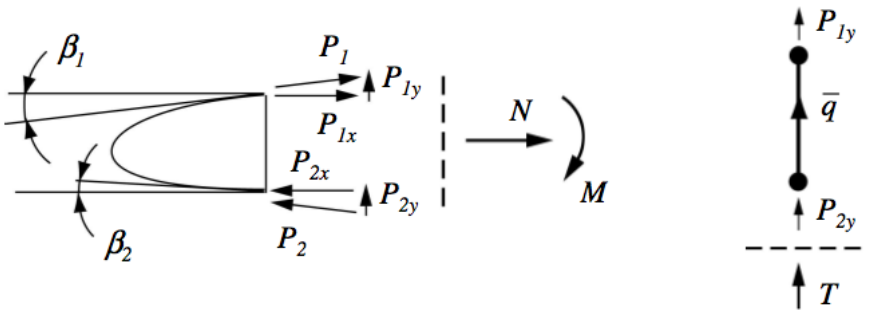

Figure 6.7 – *Rib study variables and schemes [16].*

The relationship between the components of P_j is given by:

$$P_{j_y} = P_{j_x} \tan\left(\beta_j\right) \tag{6.18}$$

Thus, the shear flow is spread between the stiffener and the panel (web) of the rib [16]:

$$T = qh_1 + P_{1_y} + P_{2_y} \implies q = \frac{T - P_{1_y} - P_{2_y}}{h_1} \tag{6.19}$$

Thus, considering Equations 6.8 and 6.15, it is possible to get the internal stress with the relative margin of safety for the sections of the rib just before and after the spar webs (section at distance a and b in Figure 6.6, resulted the two most critical sections of the rib):

NORMAL STRESS [*MPa*]	**MARGIN OF SAFETY**
$\sigma_{3_{rib}} = 10.559$	$MS_{\sigma_{3_{rib}}} = 1036.04\%$
$\sigma_{4_{rib}} = 23.081$	$MS_{\sigma_{4_{rib}}} = 419.93\%$
$\sigma_{8_{rib}} = -23.062$	$MS_{\sigma_{8_{rib}}} = 316.29\%$
$\sigma_{9_{rib}} = -10.571$	$MS_{\sigma_{9_{rib}}} = 808.19\%$

Table 6.3 – *Normal stress in the stiffeners of the root rib and corresponding margin of safety.*

SHEAR STRESS [*MPa*]	**MARGIN OF SAFETY**
$\tau_{a_{rib}} = 14.161$	$MS_{\tau_{a_{rib}}} = 163.64\%$
$\tau_{b_{rib}} = 9.52$	$MS_{\tau_{b_{rib}}} = 77.24\%$

Table 6.4 – *Shear stress in the web of the root rib and corresponding margin of safety.*

6.1.4 Analysis of the flap midpoint wing section (1.95 *m* from the tip)

The second semi-monocoque analysis was done at the flap midpoint wing section, in order to verify the stress condition in the section which has also the hinge force, produced by the flap servo, applied, using the results from the Chapter 3. All this calculations were done with Matlab.

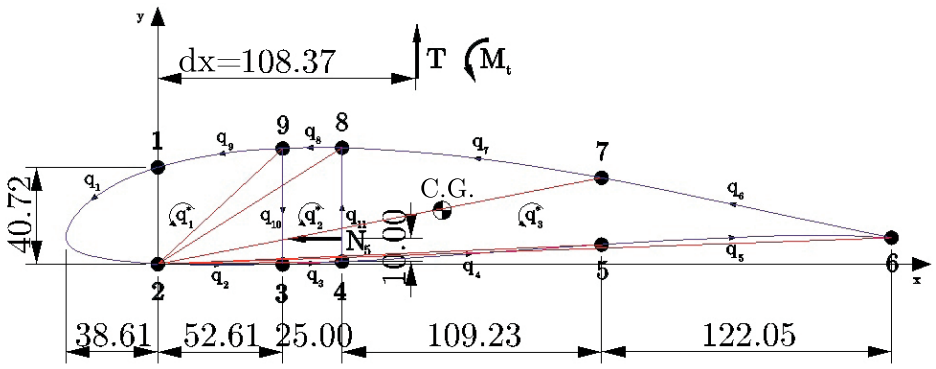

Figure 6.8 – *Semimonocoque discretization for the flap midpoint wing section.*

For the given section the center of gravity coordinates must be calculated as follows [16]:

$$X_{CG} = \frac{S_y}{A_{tot}} = \frac{\sum_{j=1}^{n} A_j X_j}{\sum_{j=1}^{n} A_j} = 121.002 \ mm \tag{6.20}$$

$$Y_{CG} = \frac{S_x}{A_{tot}} = \frac{\sum_{j=1}^{n} A_j Y_j}{\sum_{j=1}^{n} A_j} = 21.475 \ mm \tag{6.21}$$

where X_j and Y_j represent respectively the x and y stringer j concentrated area coordinate referred to the original frame of reference (placed on stiffener number 2 in Figure 6.8). Second moments of area and the product of inertia

of the discretized section are [16]:

$$I_x = \sum_{j=1}^{n} A_j y_j^2 = 344800 \ mm^4 \tag{6.22}$$

$$I_y = \sum_{j=1}^{n} A_j x_j^2 = 8666200 \ mm^4 \tag{6.23}$$

$$I_{xy} = \sum_{j=1}^{n} A_j x_i y_j = -272110 \ mm^4 \tag{6.24}$$

$$\alpha = \frac{1}{2} \arctan\left(\frac{2I_{xy}}{I_y - I_x}\right) = -0.0327 \ rad \tag{6.25}$$

which means that for this section the centroidal axes can be approximated to the frame of reference centered in the center of gravity. Applying all the previous equations to calculate the normal and shear stresses, the results for this section are:

NORMAL STRESS [*MPa*]	**MARGIN OF SAFETY**
$\sigma_1 = -73.709$	$MS_{\sigma_1} = 171.08\%$
$\sigma_2 = 82.256$	$MS_{\sigma_2} = 203.64\%$
$\sigma_3 = 82.562$	$MS_{\sigma_3} = 1200.10\%$
$\sigma_4 = 78.196$	$MS_{\sigma_4} = 1272.70\%$
$\sigma_5 = 50.618$	$MS_{\sigma_5} = 393.42\%$
$\sigma_6 = 39.741$	$MS_{\sigma_6} = 528.48\%$
$\sigma_7 = -57.048$	$MS_{\sigma_7} = 250.25\%$
$\sigma_8 = -104.236$	$MS_{\sigma_8} = 723.82\%$
$\sigma_9 = -104.314$	$MS_{\sigma_9} = 723.21\%$

Table 6.5 – *Normal stress in the stiffeners at the flap midpoint wing section and corresponding margin of safety. The loads include safety factors.*

SHEAR STRESS [MPa]	MARGIN OF SAFETY
$\tau_1 = -12.921$	$MS_{\tau_1} = 866.53\%$
$\tau_2 = -6.278$	$MS_{\tau_2} = 1889.00\%$
$\tau_3 = -5.623$	$MS_{\tau_3} = 2120.80\%$
$\tau_4 = -8.419$	$MS_{\tau_4} = 1383.30\%$
$\tau_5 = -1.858$	$MS_{\tau_5} = 6620.30\%$
$\tau_6 = 3.703$	$MS_{\tau_6} = 3272.50\%$
$\tau_7 = -3.718$	$MS_{\tau_7} = 3258.90\%$
$\tau_8 = -4.709$	$MS_{\tau_8} = 2551.90\%$
$\tau_9 = -6.866$	$MS_{\tau_9} = 1718.90\%$
$\tau_{10} = -16.898$	$MS_{\tau_{10}} = 639.08\%$
$\tau_{11} = 14.842$	$MS_{\tau_{11}} = 741.38\%$

Table 6.6 – *Shear stress in the panels at the flap midpoint wing section and corresponding margin of safety. The loads include safety factors.*

All the resulting stresses include safety factors applied previously to the loads evaluated in Chapter 3; a reduction factor of 0.8 was considered in the case of compression for the normal stresses. It is possible to see from these tables, especially for the shear stresses, that the margins of safety are very high.

6.1.5 Analysis of the flap midpoint rib (1.95 m from the tip)

Considering Equations 6.8 and 6.15, it is possible to get the internal stress with the relative margin of safety for the sections of the rib just before and after the spar webs (section at distance a and b in Figure 6.6, resulted the two most critical sections of the rib), as for the root rib:

NORMAL STRESS [MPa]	MARGIN OF SAFETY
$\sigma_{3_{rib}} = 25.383$	$MS_{\sigma_{3_{rib}}} = 883.96\%$
$\sigma_{4_{rib}} = 44.591$	$MS_{\sigma_{4_{rib}}} = 460.13\%$
$\sigma_{8_{rib}} = -44.616$	$MS_{\sigma_{8_{rib}}} = 347.81\%$
$\sigma_{9_{rib}} = -25.408$	$MS_{\sigma_{9_{rib}}} = 686.39\%$

Table 6.7 – *Normal stress in the stiffeners of the flap midpoint rib and corresponding margin of safety.*

SHEAR STRESS [MPa]	MARGIN OF SAFETY
$\tau_{a_{rib}} = 22.623$	$MS_{\tau_{a_{rib}}} = 452.01\%$
$\tau_{b_{rib}} = 32.991$	$MS_{\tau_{b_{rib}}} = 278.52\%$

Table 6.8 – *Shear stress in the web of the flap midpoint rib and corresponding margin of safety.*

6.1.6 Analysis of the aileron midpoint wing section (0.8125 m from the tip)

The third and last semi-monocoque analysis was done at the aileron midpoint wing section, in order to verify the stress condition in the section which has also the hinge force, produced by the aileron servo, applied, using applicable results from the Chapter 3. All these calculations were done with Matlab.

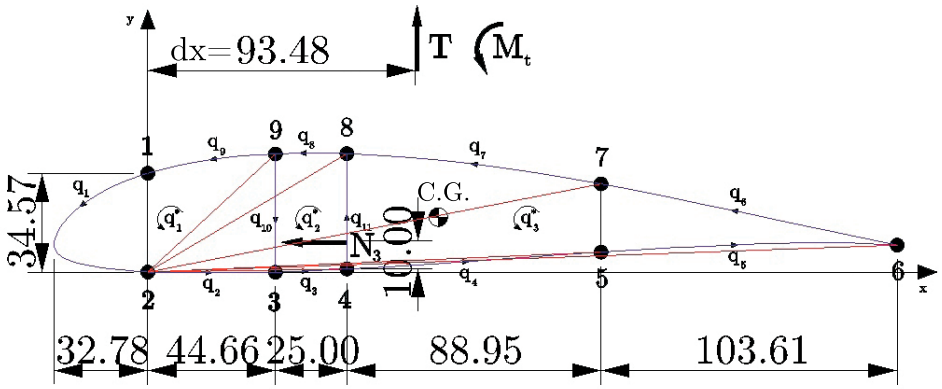

Figure 6.9 – *Semimonocoque discretization for the aileron midpoint wing section.*

For the given section the center of gravity coordinates must be calculated

as follows [16]:

$$X_{CG} = \frac{S_y}{A_{tot}} = \frac{\sum_{j=1}^{n} A_j X_j}{\sum_{j=1}^{n} A_j} = 104.824 \ mm \tag{6.26}$$

$$Y_{CG} = \frac{S_x}{A_{tot}} = \frac{\sum_{j=1}^{n} A_j Y_j}{\sum_{j=1}^{n} A_j} = 18.172 \ mm \tag{6.27}$$

where X_j and Y_j represent respectively the x and y stringer j concentrated area coordinate referred to the original frame of reference (placed on stiffener number 2 in Figure 6.9). Second moments of area and the product of inertia of the discretized section are [16]:

$$I_x = \sum_{j=1}^{n} A_j y_j^2 = 201650 \ mm^4 \tag{6.28}$$

$$I_y = \sum_{j=1}^{n} A_j x_j^2 = 520560 \ mm^4 \tag{6.29}$$

$$I_{xy} = \sum_{j=1}^{n} A_j x_i y_j = -163270 \ mm^4 \tag{6.30}$$

$$\alpha = \frac{1}{2} \arctan\left(\frac{2I_{xy}}{I_y - I_x}\right) = -0.0326 \ rad \tag{6.31}$$

which means that for this section the centroidal axes can be approximated to the frame of reference centered in the center of gravity. Applying all the previous equations to calculate the normal and shear stresses, the results for this section are:

NORMAL STRESS [MPa]	MARGIN OF SAFETY
$\sigma_1 = -16.491$	$MS_{\sigma_1} = 1111.60\%$
$\sigma_2 = 18.275$	$MS_{\sigma_2} = 1266.70\%$
$\sigma_3 = 18.346$	$MS_{\sigma_3} = 5750.90\%$
$\sigma_4 = 17.179$	$MS_{\sigma_4} = 6148.20\%$
$\sigma_5 = 11.266$	$MS_{\sigma_5} = 2117.00\%$
$\sigma_6 = 8.802$	$MS_{\sigma_6} = 2737.60\%$
$\sigma_7 = -12.741$	$MS_{\sigma_7} = 1468.30\%$
$\sigma_8 = -23.391$	$MS_{\sigma_8} = 3571.20\%$
$\sigma_9 = -23.249$	$MS_{\sigma_9} = 3593.50\%$

Table 6.9 – *Normal stress in the stiffeners at the aileron midpoint wing section and corresponding margin of safety. The loads include safety factors.*

SHEAR STRESS [MPa]	MARGIN OF SAFETY
$\tau_1 = -6.004$	$MS_{\tau_1} = 1979.90\%$
$\tau_2 = -3.327$	$MS_{\tau_2} = 3653.20\%$
$\tau_3 = -2.899$	$MS_{\tau_3} = 4206.40\%$
$\tau_4 = -4.294$	$MS_{\tau_4} = 2808.00\%$
$\tau_5 = -1.454$	$MS_{\tau_5} = 8487.20\%$
$\tau_6 = 1.242$	$MS_{\tau_6} = 9952.30\%$
$\tau_7 = -1.748$	$MS_{\tau_7} = 7044.80\%$
$\tau_8 = -2.249$	$MS_{\tau_8} = 5451.90\%$
$\tau_9 = -3.283$	$MS_{\tau_9} = 3704.00\%$
$\tau_{10} = -6.988$	$MS_{\tau_{10}} = 1687.10\%$
$\tau_{11} = 5.514$	$MS_{\tau_{11}} = 2164.60\%$

Table 6.10 – *Shear stress in the panels at the aileron midpoint wing section and corresponding margin of safety. The loads include safety factors.*

All the resulting stresses include safety factors applied previously to the loads evaluated in Chapter 3; a reduction factor of 0.8 was considered in the case of compression for the normal stresses. It is possible to see from these tables, especially for the shear stresses, that the margins of safety are very high.

6.1.7 Analysis of the aileron midpoint rib (0.8125 m from the tip)

Considering Equations 6.8 and 6.15, it is possible to get the internal stress with the relative margin of safety for the sections of the rib just before and after the spar webs (section at distance a and b in Figure 6.6, resulted the two most critical sections of the rib), as for the flap midpoint rib:

NORMAL STRESS [MPa]	MARGIN OF SAFETY
$\sigma_{3_{rib}} = 11.822$	$MS_{\sigma_{3_{rib}}} = 2012.70\%$
$\sigma_{4_{rib}} = 20.579$	$MS_{\sigma_{4_{rib}}} = 1113.60\%$
$\sigma_{8_{rib}} = -20.866$	$MS_{\sigma_{8_{rib}}} = 857.58\%$
$\sigma_{9_{rib}} = -11.834$	$MS_{\sigma_{9_{rib}}} = 1588.50\%$

Table 6.11 – *Normal stress in the stiffeners of the aileron midpoint rib and corresponding margin of safety.*

SHEAR STRESS [MPa]	MARGIN OF SAFETY
$\tau_{a_{rib}} = 10.011$	$MS_{\tau_{a_{rib}}} = 1147.50\%$
$\tau_{b_{rib}} = 8.031$	$MS_{\tau_{b_{rib}}} = 1445.00\%$

Table 6.12 – *Shear stress in the web of the aileron midpoint rib and corresponding margin of safety.*

6.2 The junction wing-fuselage analysis

6.2.1 Introduction

The use of mechanical fasteners to assemble airframe structures is a mature technology. Composites are not an exception. Failure modes for advanced composite mechanical joints are similar to those for conventional

metallic mechanically fastened joints. But the behavior of composite joints differs significantly from those of metallic joints and deserves special attention for a number of reasons [9]:

- relative brittleness of material, which results in high stress concentrations athole edges;

- laminate failure is a function of stacking sequence, fiber volume, porosity, etc.

When fasteners are required, composites present special design considerations. Composite materials derive their properties from both the fibers and the matrix, and are nothomogeneous. They do not respond to fasteners in the same way as metals. Therefore, it is not possible to design fasteners that are general applicable to all composites. Composites possess different characteristics than their metallic counterparts: even though they are very strong, they can be very delicate if not treated properly. Therefore, the selection of the correct fastened joint is critical. A safety factor, called *fitting factor*, must be considered: typically, it goes from 1.15 to 1.2 depending if for military or civil aircraft.

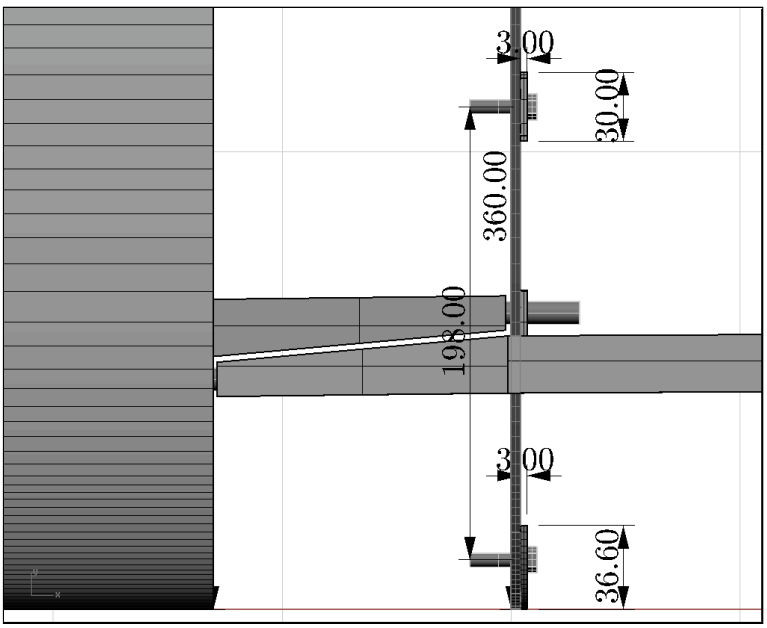

Figure 6.10 – *Modular UAS's junctions pins top view generated with Rhinoceros 4.0 (dimensions in millimeters).*

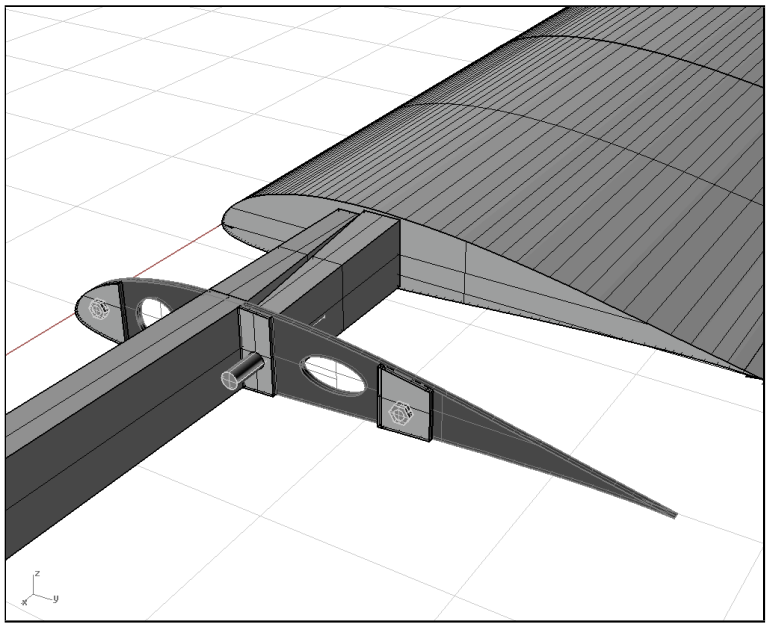

Figure 6.11 – *Modular UAS's junction pins view generated with Rhinoceros 4.0.*

The following figure shows the Modular UAS junction between the wing and the fuselage. As said previously, it must the the same of the original wing, in order to maintain the modular concept of the aircraft. The materials properties needed for the junction analysis are listed in the following table (taken from [16] and Gary Cordeley (CSIR researcher):

MATERIAL	**MAXIMUM STRESS [*MPa*]**
Steel	$\tau_{max} = 517$
Interglass 92149/Epoxy	$\sigma_{max} = 120$
Interglass 92149/Epoxy	$\tau_{max} = 25.1$
Tufnol Kite Brand	$\sigma_{max} = 200$
Tufnol Kite Brand	$\tau_{max} = 105$

Table 6.13 – *Materials properties needed for the junction analysis.*

where the Interglass 92149/Epoxy is the material used for the M6 pins support (thickness 3.3 mm) and the Tufnol Kite Brand is the one used for the M10 pin support (thickness 15 mm).

6.2.2 Analysis of the 10 *mm* pin

The 10 *mm* pin is bonded into the spar, which goes into the hole of the root rib of the central wing. A similar pin, is placed into the spar of the central wing, and it goes into the root rib of the wing. Figure 6.10 explains graphically how exactly is the joining with these two spar pins. Thus, the two spar pins work together as constrains to absorb the bending moment, consequently the following force acts on them [John Monk]:

$$P_{M10} = f_f \frac{M_{b_{root}}}{d_{roots}} = 20899 \ N \tag{6.32}$$

where $M_{b_{root}}$ is the bending moment at the root, which includes safety factors, taken from Chapter 3, f_f is the fitting factor equal to 1.2 and d_{roots} is the distance between the wing root and the central wing root, which is basically the fuselage width where the junction is considered. First of all the maximum shear stress on the pin section needs to be compared with the maximum allowable shear, considering τ_{max} of the steel equal to 517 *MPa* [16]:

$$\tau_{M10} = \frac{4}{3} \frac{P_{M10}}{\pi \frac{d^2}{4}} = 177.39 \ MPa \tag{6.33}$$

where d is the diameter of the pin and $\frac{4}{3}$ is a factor which considers the parabolic distribution of the shear stress in the pin section. Using Equation 6.16, this result guarantees a margin of safety equals to 191.44%. The hole in the Tufnol Kite Brand support needs to be analyzed for the failure in tension as shown in the following figure (all the geometric data are taken from CAD and are available in Appendix A.3.3):

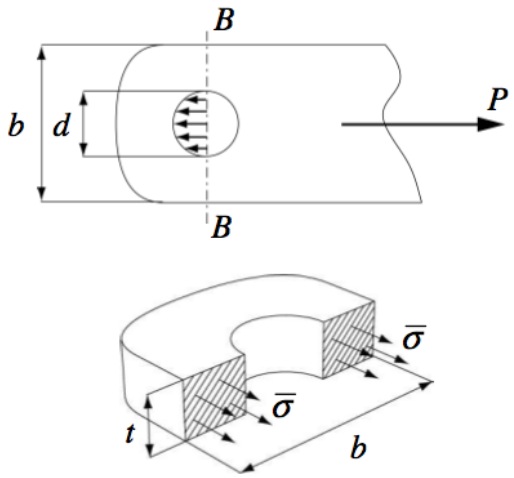

Figure 6.12 – *Failure in tension analysis [16].*

$$\sigma_{M10} = \frac{P_{M10}}{(b-d)t} = 121.15\ MPa \tag{6.34}$$

with a margin of safety equals to 65.08% calculated using Equation 6.16.

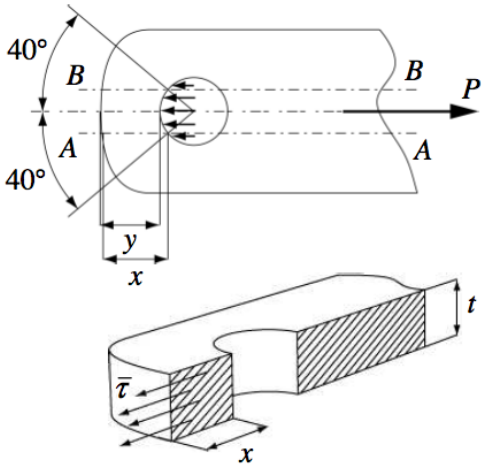

Figure 6.13 – *Failure by shear tear out [16].*

$$\tau_{M10} = \frac{P_{M10}}{2xt} = 68.43 \ MPa \tag{6.35}$$

It needs also to be analyzed for the shear out failure as shown in the previous figure. It results with a margin of safety equals to 53.44% calculated using Equation 6.16.

6.2.3 Analysis of the 6 *mm* pins

The 6 *mm* pins are bonded into the root rib, and go into the holes of fuselage. Figure 6.10 explains graphically how exactly is the joining with these pins. They transfer the shear force and the torque moment acting at the root as follows [John Monk]:

$$\begin{aligned} P_{M6_1} &= -f_f \frac{M_{t_{root}}}{d_{pins}} + T_{root} = 2752.6 \ N \\ P_{M6_2} &= f_f \frac{M_{t_{root}}}{d_{pins}} + T_{root} = 1173.6 \ N \end{aligned} \tag{6.36}$$

where the $M_{t_{root}}$ is the torque moment at the root and T_{root} is the shear force at the root, which includes safety factors, taken from Chapter 3, f_f is the fitting factor equal to 1.2 and d_{pins} is the distance between the two M6 pins bonded in the root rib (pin 1 is close to the leading edge, pin 2 is close to the trailing edge). First of all the maximum shear stress on the pin section needs to be compared with the maximum allowable shear, considering τ_{max} of the steel equal to 517 *MPa* [16]:

$$\begin{aligned} \tau_{M6_1} &= \frac{4}{3} \frac{P_{M6_1}}{\pi \frac{d^2}{4}} = 64.91 \ MPa \\ \tau_{M6_2} &= \frac{4}{3} \frac{P_{M6_2}}{\pi \frac{d^2}{4}} = 27.67 \ MPa \end{aligned} \tag{6.37}$$

where d is the diameter of the pins and $\frac{4}{3}$ is a factor which considers the parabolic distribution of shear stress in the pin section. Using Equation 6.16, this results guarantee a margin of safety equal to 696.58% and 1768.4% respectively. Using the same procedure of the previous paragraph for the

holes, the results listed in the following table are obtained (all the geometric data are taken from CAD and are available in Appendix A.3.3):

STRESS [*MPa*]	**MARGIN OF SAFETY**
$\sigma_{M6_1} = 31.86$	$MS_{\sigma_{M6_1}} = 276.63\%$
$\tau_{M6_1} = 24.72$	$MS_{\sigma_{M6_1}} = 1.53\%$
$\sigma_{M6_2} = 14.82$	$MS_{\sigma_{M6_2}} = 709.84\%$
$\tau_{M6_2} = 11.44$	$MS_{\sigma_{M6_2}} = 109.50\%$

Table 6.14 – *Stress in the root holes and corresponding margin of safety.*

6.3 FEM analysis with MSC Patran/Nastran2010

6.3.1 Loads used for the FEM analysis

The first step to carry out the analysis in Patran/Nastran2010 of the new wing structure is to define the discrete loads their location to reproduce the real flight condition. The distributed loads (lift and mass force) are considered applied on the ribs as follows [16]:

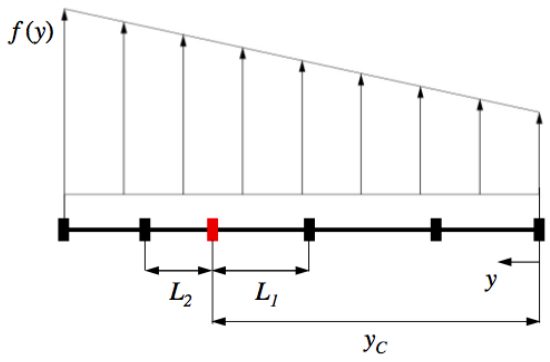

Figure 6.14 – *Application of the distributed loads as discrete to the ribs of the wing [16].*

The equation that gives the resulting discrete force which must be applied to a given rib is [16]:

$$R = \int_{y_c - L_1/2}^{y_c + L_2/2} f(y)\, dy \tag{6.38}$$

where y_c is the rib position and $f(y)$ is the distributed load. In the following figure the positions along the wing span are shown:

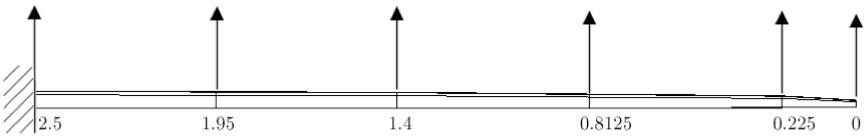

Figure 6.15 – *Application point along the wing span of the discrete loads to the ribs of the wing [16].*

The Matlab script available in Appendix A.3.1 reports all the calculations needed to get the following results:

RIB POSITION [m]	**LOAD [N]**
0.0000	$R_1 = 29.0681$
0.2250	$R_2 = 146.0438$
0.8125	$R_3 = 243.7066$
1.4000	$R_4 = 264.9968$
1.9500	$R_5 = 268.7540$
2.5000	$R_6 = 138.0023$

Table 6.15 – *Position of the ribs along the wing span and corresponding discrete load.*

To confirm the results, the equivalent shear force and bending moment at the root must be calculated. In this case the results are:

$$T_{root} = \sum_{j=1}^{N} R_j = 1090.6\ N \tag{6.39}$$

$$M_{b_{root}} = \sum_{j=1}^{N} -R_j(y_j - 2.5) = 1255.07\ Nm \tag{6.40}$$

Comparing this result with the data from Chapter 3 (internal loads not including safety factors), it is possible to see that the shear force and the bending moment at the root are the same. With regards to the torque moment (thus, looking at the rib section), the loads must be shifted from the shear center of the wing section (44.71% of the chord length from the leading edge as results from the semi-monocoque analysis) by a distance for which the resulting torque moment is the same of the analysis in Chapter 3.

S.C. [*mm*]	**APPLICATION POINT [*mm*]**	**M_t [*Nm*]**
71.6	71.6	−0.00
114.1	100.6	−1.98
132.0	58.9	−17.83
149.9	62.0	−23.31
155.5	104.9	−13.60
161.4	47.7	−15.65

Table 6.16 – *Application point on the rib and corresponding discrete torque moments.*

To confirm the results, the equivalent torque moment at the root must be calculated. In this case the result is:

$$M_{t_{root}} = \sum_{j=1}^{N} M_{t_j} = -72.37\ Nm \tag{6.41}$$

which is the same torque moment seen in Chapter 3 (not including safety factors). Hence, applying the discrete loads listed in Table 6.15 at the proper position, the wing sees at each rib station the same internal load of the critical flight condition. It must be said that these results are the same provided to John Monk and Neall Moore in order to design the whiffle tree necessary to test the wing.

6.3.2 Import of the CAD and creation of the mesh

The CAD was generated with Rhinoceros 4.0 and the wing FEM was modeled in Patran2010 with the help of Pieter Rossouw as follow:

- wing is fixed like a cantilever beam at the root;
- loads applied at the ribs (see Table 6.16);
- whole wing is modelled as surfaces;
- skins, ribs and spar surfaces must have common edges at edges adjacent to each other.

Modifying the surfaces and importing it into Patran required a few iterations to obtain a final optimized wing which helped in an effective meshing of the wing surfaces. The wing thus consists out of several separate surfaces which were meshed individually. The node points on adjacent edges must be equal and coincident so that all the surfaces can be joined together to form an integrated structure.

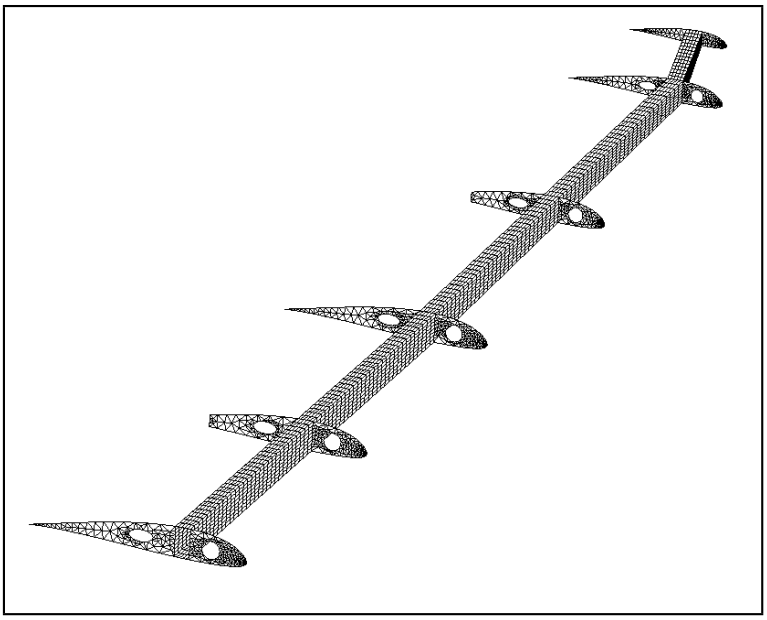

Figure 6.16 – *Meshed structure (ribs and spar) of the wing generated in Patran2010.*

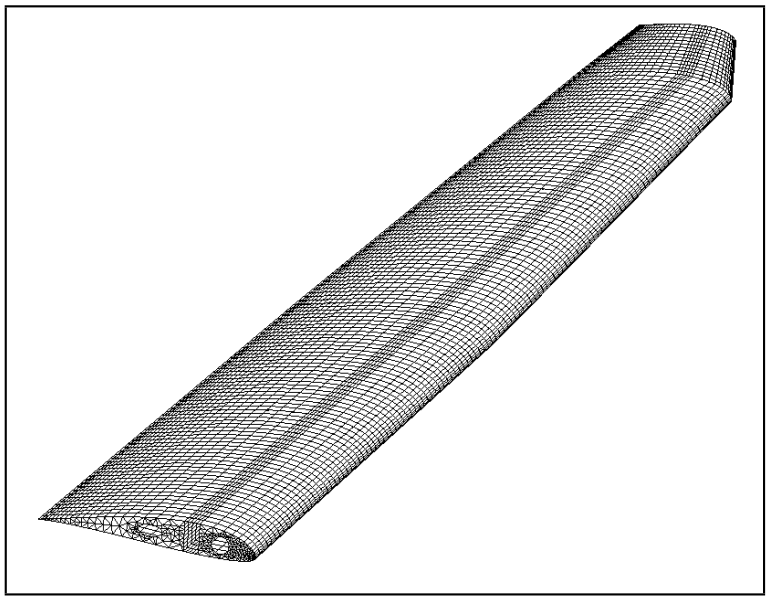

Figure 6.17 – *Complete meshed wing generated in Patran2010.*

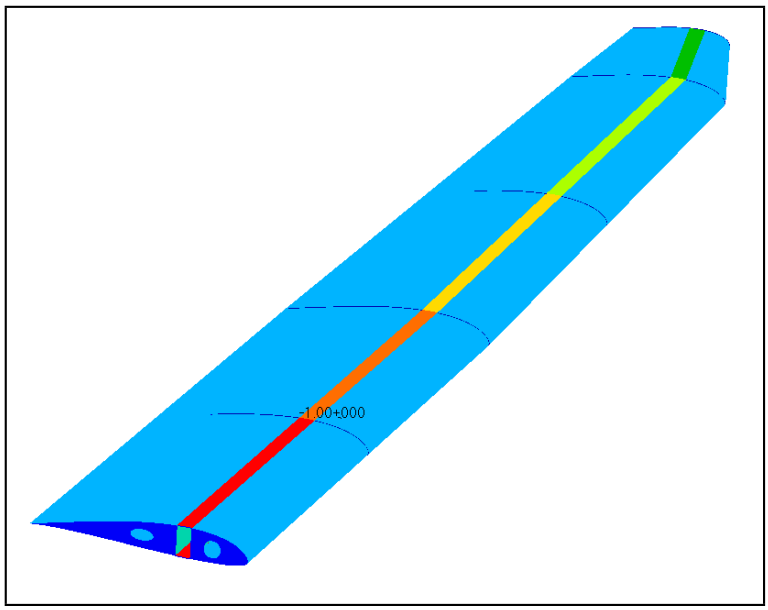

Figure 6.18 – *Properties-plot of different surfaces of the wing generated in Patran2010.*

Several surfaces also aid in applying different material properties and thicknesses to the various parts of the wing. These informations were taken respectively from Chapter 4 and Chapter 5.

6.3.3 Result of the FEM analysis

Once the mesh is ready, and the properties of the materials are given, the loads can be applied and the simulation in Nastran2010 can run. From Figures 6.19 and Figure 6.20 it is possible to see the resulting Von Mises stresses in the structure. To compare them with the semi-monocoque analysis the resulting normal stress is also shown in Figure 6.21. As could be aspected, the root section is the most critical area of the wing. In Figure 6.22 and Figure the displacements due to the application of the loads are shown; these results will be compared with the real displacement of the structure during the test with the whiffle tree at the CSIR test rig. The maximum displacement is at the tip, and is equal to 195 *mm*.

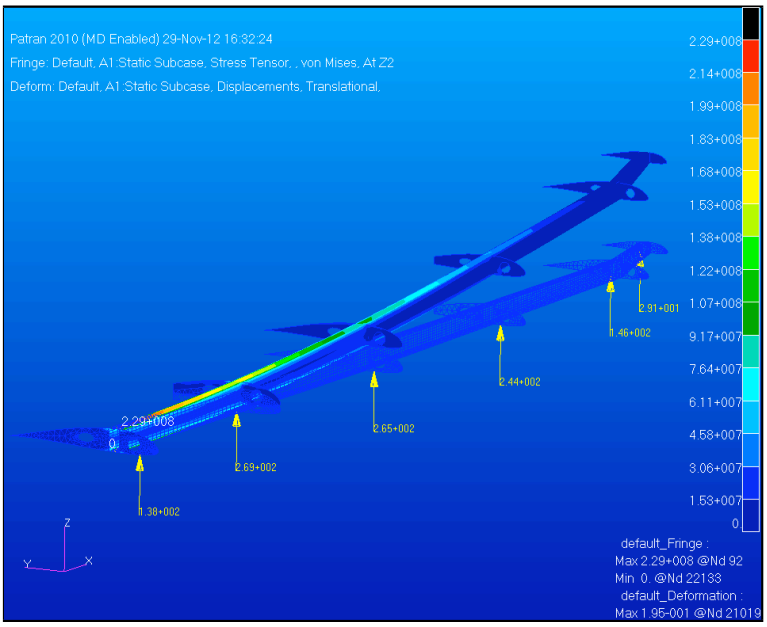

Figure 6.19 – *Equivalent Von Mises stress condition of the wing generated with Nastran2010.*

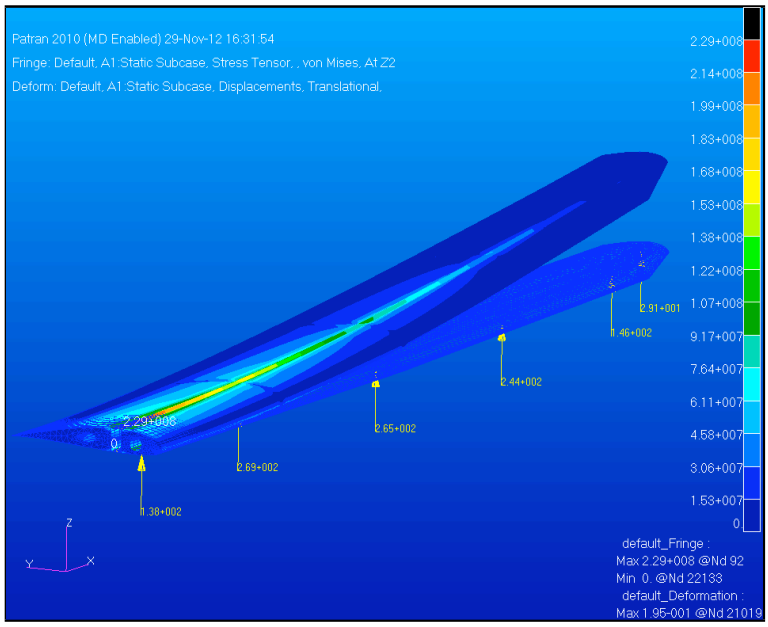

Figure 6.20 – *Equivalent Von Mises stress condition generated with Nastran2010.*

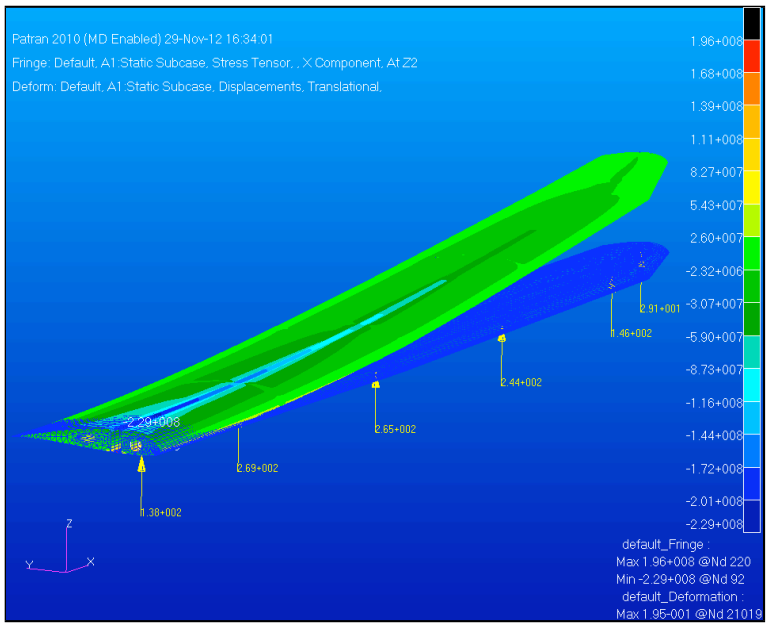

Figure 6.21 – *Normal stress in the wing generated in Nastran2010.*

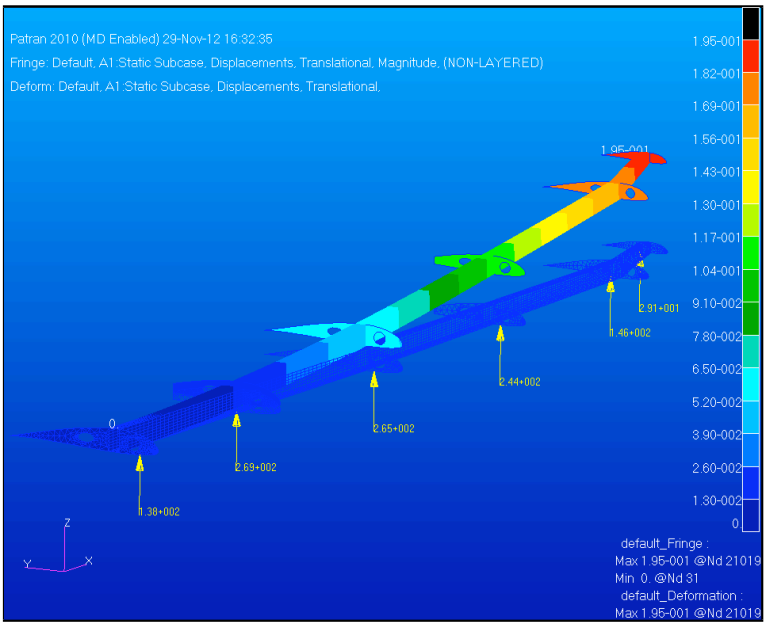

Figure 6.22 – *Displacement of the wing structure generated in Patran2010.*

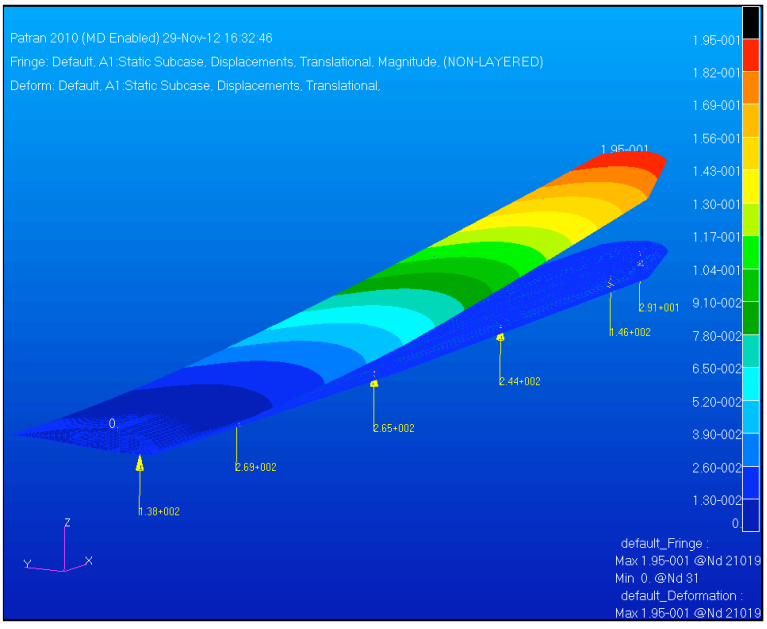

Figure 6.23 – *Displacement of the wing generated in Patran2010.*

It is now possible to show the resulting maximum equivalent Von Mises stress, for each component of the root section. The margin of safety was obtained with Equation 6.16 comparing the actual stress with the maximum allowable stress of the component (available in Chapter 4).

COMPONENT	**VON MISES STRESS [*MPa*]**	**MS$_{\%}$**
Spar caps	229.0	274.9%
Spar webs	61.1	408.8%
Root rib	61.1	196.4%
Skin	122.1	63.6%

Table 6.17 – *Equivalent Von Mises stress for each root component of the wing structure and corresponding margin of safety.*

These results show also that the semi-monocoque discretization chosen for this wing section gives undervalue for the stress in the panels of the wing. Thus, this semi-monocoque analysis can be used as a first approach study, but it is not enough accurate. This is due to the semi-monocoque model chosen, which can be more accurate if the number of dummy stiffener is increased.

Chapter 7

Manufacturing of the new wing

7.1 Equipment and lab

The CSIR DPSS ASC has the UAV Lab situated in Building 12. This lab is divided in several areas, and for the purpose of this work the Workshop, equipped with usual tool and foam cutting machines and the Composite Room, used for the preparation processes for composite material manufacturing and layup, were used. Both had available materials and tools needed for the several manufacturing steps of the wing. According to the type of work to be done, it was followed all the safety rules and precautions in place by the UAV Lab regulation (i.e. safety glasses, gloves and coat).

7.2 Spar

A rectangular spar, with two separate elements, i.e. the spar caps and the spar webs, was considered. Due to its high maximum tensile strength and elastic modulus the unidirectional 300 GSM carbon fiber was chosen for the top and bottom surfaces of the rectangular spar, being able to absorb the normal stress given by the bending moment applied on the wing structure. The idea was to reduce the layers of the spar caps from 5 to 1 along the span, decreasing from the root to the tip one layer of UD 300 GSM at each rib. For the spar webs, one single carbon fiber braided sleeve has been considered as a possible structural solution for the torque box, working together with the D-box of the leading edge of the wing. A foam mold was used to layup the carbon fiber UD 300 GSM strips as spar caps, and the single carbon fiber

braided sleeve $\pm 45^\circ$ as spar webs. A full tufnol block (for the last 60 mm of the spar length) was needed, instead of the foam spar mold, to transfer the bending moment of the spar at the root to the central wing root rib with a 10 mm pin. Thus, the materials needed to manufacture the two spars (one for each half wing) are:

- 40 linear meters of UD 300 GSM 25 mm width;
- 6 linear meters of carbon fiber braided sleeve $\pm 45^\circ$ 50 mm width;
- 1 linear meters of carbon fiber wire;
- foam 32 kg/m^3 to be cut as spar molds;
- 2 Tufnol Kite Brand full block, 60 mm length with the hole for the 10 mm pin;
- 2 steel pins, diameter 10 mm and length 64 mm;
- epoxy glue fast curing;
- epoxy resin Ampreg21 with standard hardener;
- curing process consumables materials, i.e., peel ply, perforated ply, breather, vacuum bag, tacky tape, scissors, cups.

7.2.1 Spar foam mold

The ASC's workshop has a foam cutting machine (Figure 7.1) that can be used for this purpose, which cuts pieces of maximum 60 cm length. This distance can be considered as a limit for the spar mold pieces length (to be bonded together afterwards). Thus, the idea is to cut the spar mold foam in pieces long as the ribs distance, then bond them together using a scale 1:1 CAD printout as angle reference.

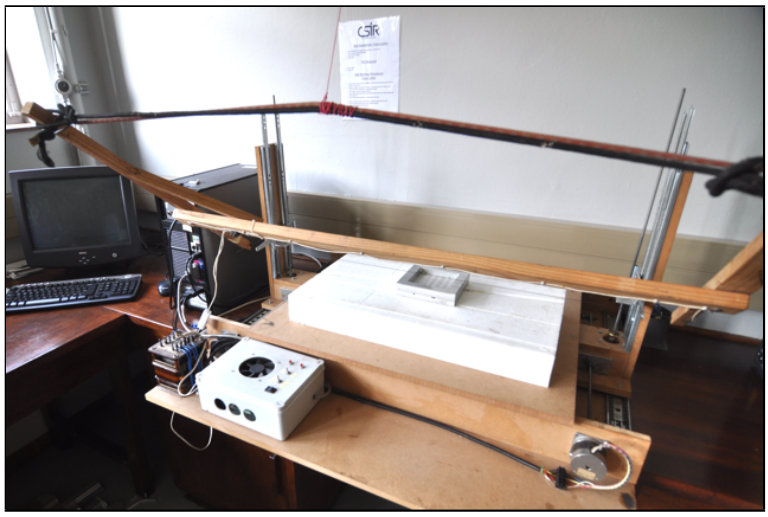

Figure 7.1 – *CSIR DPSS ASC's workshop foam cutting machine.*

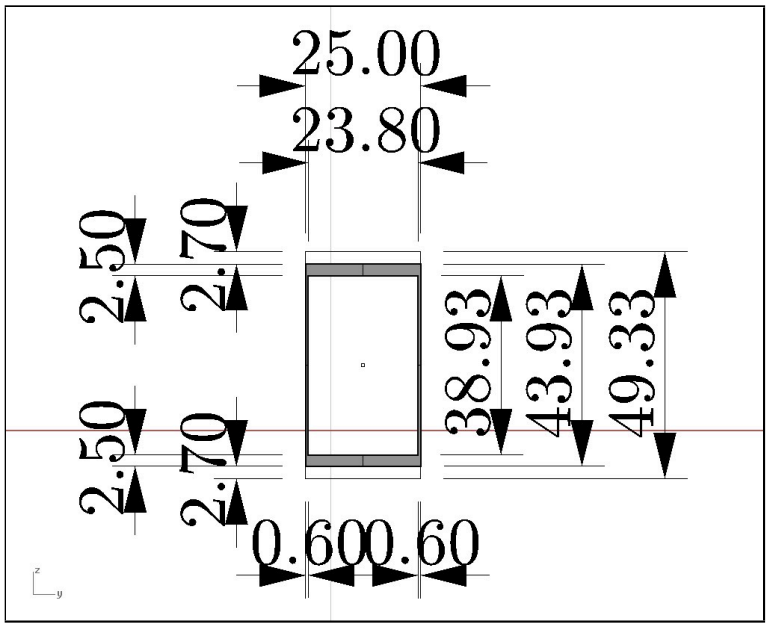

Figure 7.2 – *Spar mold section at the root. The internal white area is the actual foam mold section.*

The foam mold manufacturing started with the import of the *.dat* file of the several pieces of the spar mold (the two external sections of each piece)

in the software JediCut. Every part had rectangular section according to the resulting spar needed. In Figure 7.2 the root spar section is shown as an example. The gray area represents the aspected spar structure thickness, and the white area is the actual foam mold section. According to the CAD, the two external faces of the foam piece, the length, and the offset were set up.

Figure 7.3 – *Resulting spar foam mold.*

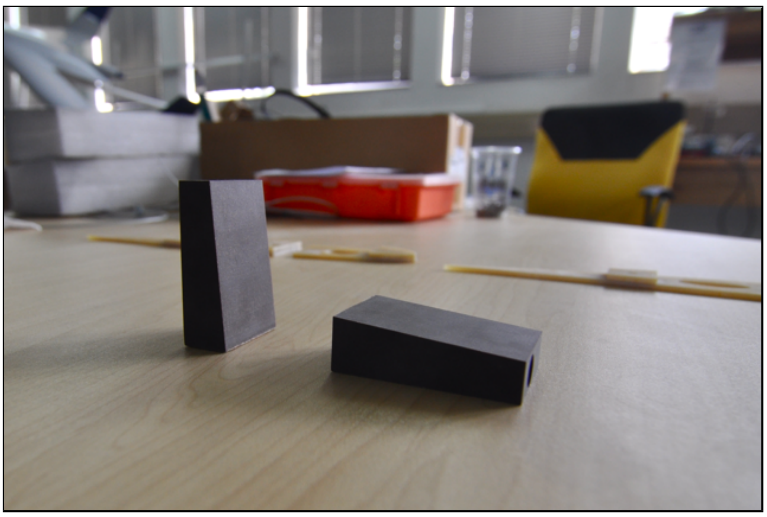

Figure 7.4 – *Tufnol Kite Brand blocks (manufactured by L.S.T. L.d.t.).*

In the following table the dimensions of each piece of foam are shown, where w_r is the width of the section facing the root, h_r is the height of the section facing the root, w_t is the width of the section facing the tip, h_t is the width of the section facing the root, l is the length of the piece and o the offset between the extreme faces of the piece.

$\mathbf{w}_r$ $[mm]$	$\mathbf{h}_r$ $[mm]$	$\mathbf{w}_t$ $[mm]$	$\mathbf{h}_t$ $[mm]$	$\mathbf{l}$ $[mm]$	$\mathbf{o}$ $[mm]$
18.30	36.58	23.80	38.73	69.98	1.00
23.80	38.73	23.80	36.97	550.00	4.26
23.80	37.77	23.80	36.02	550.00	4.26
23.80	36.82	23.80	31.19	587.50	15.87
23.80	31.99	23.80	26.37	587.50	15.87
23.80	27.17	23.80	13.77	222.00	53.09

Table 7.1 – *Application point on the rib and corresponding discrete torque moments.*

Once the six foam molds (for each spar, which were specular) were cut, they were bonded together using epoxy glue fast curing (with the help of Duncan Higgs, CSIR researcher). On every bonding face the reduction of the layers of the spar caps from 5 to 1 along the span (0.4 mm for each step) was considered, in order to maintain the straight resulting top surface of the spar. The alignment was made:

- for the top surface taping the UD 300 GSM (according to the design) and putting the spar upside down, hence using the table as a straight reference;
- for the lateral surfaces using a scale 1:1 CAD printout as angle reference.

As last, the Tufnol Kite Brand pieces were bonded measuring the angle. These pieces were made by Lightweight Structure Technology L.t.d. with a NC cutting machine.

7.2.2 Layup and curing process of the spar

The layup process started by cutting all the carbon fiber pieces. For each spar:

- 2 pieces of UD 300 GSM length 680 mm;

- 2 pieces of UD 300 GSM length 1230 mm;
- 2 pieces of UD 300 GSM length 1817.5 mm;
- 2 pieces of UD 300 GSM length 2405 mm;
- 2 pieces of UD 300 GSM length 2630 mm;
- 1 piece of carbon fiber braided sleeve $\pm 45°$ length 2630 mm;

were prepared. The layup was made in the Composite Room of the UAV Lab with the collaboration of Alan Sutherland and Tim King (CSIR researchers). In the following order, breather, perforated ply and peel ply were placed on the table. The process began laying up on the foam mold the top surface of the spar (i.e. spar caps) starting from the root, and once it was ready, the spar and its foam mold were put upside down on the table, laying up the bottom surface (i.e. spar caps). The curing process was made for at least 5 hours in a vacuum bag (previously prepared) and 24 hours at ambient conditions. The carbon fiber braided sleeve was cured separately, in order to not move the UD 300 GSM during the placement of the carbon braided sleeve, with an other curing cycle of 5 hours in a vacuum bag and 24 hours at ambient conditions. Once ready, the spars were unpacked and the last curing cycle (without vacuum bag) was made lo layup the carbon fiber wire, wrapped around the last 60 mm of the spar, where the tufnol block was placed. The last step was to sand all around the spar to improve the characteristic of bonding.

7.3 Ribs and pins supports

As mentioned in Chapter 5, the actual manufacture of the ribs was ordered at Lightweight Structure Technology L.t.d. based in Pretoria (South Africa). This because they can also provide NC mechanical cutting. Specifically:

- 2 fiberglass $\pm 45°$ root ribs, thickness 3.3 mm;
- 4 fiberglass $\pm 45°$ pin supports (to bond around the holes where the M6 pins go), thickness 3.3 mm;
- 2 Tufnol Kite Brand pin support (to bond around the hole where the M10 pin goes) thickness 15 mm;

- 10 carbon fiber ribs, composed by two layers of fabric ±45° per side and a foam sandwich core of 2 *mm*.

were ordered. The following Figure 7.5 shows these pieces. The only procedure made in the Workshop regard the ribs was sanding where the bonding was supposed to be, thus, all around the edges and the surfaces where the pin supports were bonded on the root rib.

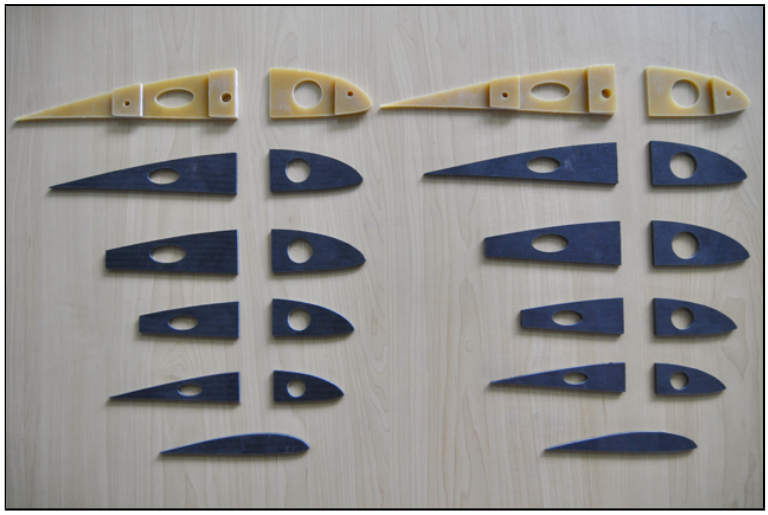

Figure 7.5 – *Fiberglass root ribs and other carbon fiber sandwich ribs.*

7.4 Skin

The layup was designed with two plies of carbon fiber fabric ±45° per side and a foam sandwich core of 2 *mm*, for a total thickness of 3 *mm*. This provides a big increase of the local bending stiffness of the skin, keeping the structure working in an optimized way for both shear force and torque moment [16]. One additional small layer of carbon fiber fabric, placed at 0°/90°, was designed for the areas where the two holes for the control surfaces servos are located. This permits a better redistribution of the stresses around the hole itself [9]. To obtain a good finish quality of the surface, a single thin ply of fiber glass 20 g/m^2 was used. Thus, the materials needed to manufacture the four skins (two for each half wing) are:

- 20 linear meters of carbon fiber fabric ±45° 200 GSM 1000 *mm* width;
- 6 linear meters of fiberglass fabric ±45° 20 GSM 1000 *mm* width;
- 6 linear meters of foam 1000 *mm* width;
- epoxy resin Ampreg21 with standard hardener;
- curing process consumables materials, i.e., peel ply, perforated ply, breather, vacuum bag, tacky tape, scissors, cups.

7.4.1 Skin open mold

The open mold used to layup the top and bottom skins of the wing was manufactured by Lightweight Structure Technology L.d.t. and delivered to the ASC UAV Lab. Figure 7.6 shows the top skin mold already waxed and ready for the layup. Additional fiberglass plates were prepared to be screwed to the leading edge of the mold, in order to obtain a 8 *mm* portion of fabric reentrant (respect to the leading edge). This flat reentrant surface is needed to have large and flat bonding surface at the leading edge of the top and bottom skins once ready.

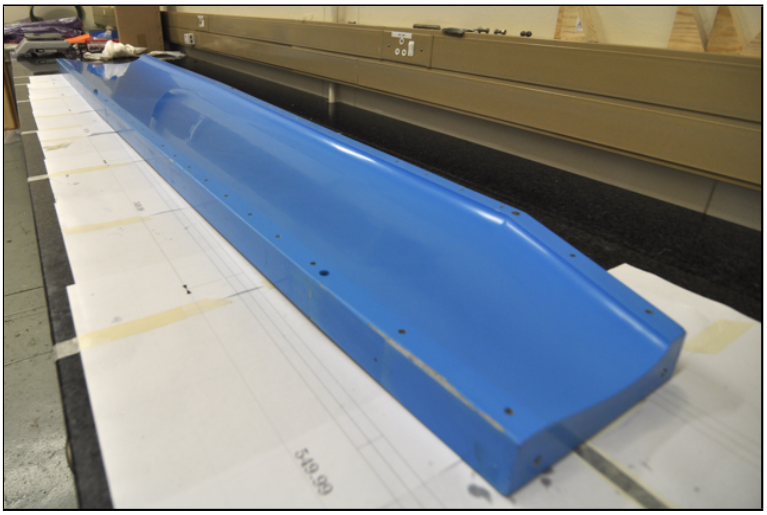

Figure 7.6 – *Top skin mold already waxed and ready for the layup (manufactured by Lightweight Structure Technology L.d.t.).*

7.4.2 Layup and curing process of the skin

The layup process started cutting all the fabric and foam pieces. For each skin:

- a paper template of the skin;
- fiberglass fabric ±45° 20 GSM cut with the template (Figure 7.7);
- carbon fiber fabric ±45° 200 GSM cut with the template (Figure 7.8);;
- foam 2 *mm* thick cut considering the spar position, the hinges of flap and aileron and the hinge line of them (Figure 7.9);
- cotton flocs and resin as filler for the leading edge.

were prepared. Then, the layup of the top skin was made in the Composite Room of the UAV Lab with the collaboration of Duncan Higgs and Hudivhamudzimu Ravele (South African Air Force). In the following order, breather, perforated ply and peel ply were placed on the table. The process began laying up on the open mold the fiberglass, then two layers of carbon fiber. After that, the foam was placed and subsequently the last two layers of carbon fiber. In the following order were placed peel ply, perforated ply and breather on the laminate. The curing process was made for at least 5 hours in a vacuum bag (previously prepared) and 24 hours at ambient conditions.

Figure 7.7 – *Cutting phase of the fiberglass fabric 20 g/m^2.*

The layup of the bottom skin was made in the Composite Room of the UAV Lab as well with the collaboration of Alan Sutherland, Tim King and Pieter Rossouw then the laminate was cured for at least 5 hours in a vacuum bag (previously prepared) and 24 hours at ambient conditions.

Figure 7.8 – *Cutting phase of the carbon fiber fabric 200 g/m^2 with the paper template as reference*

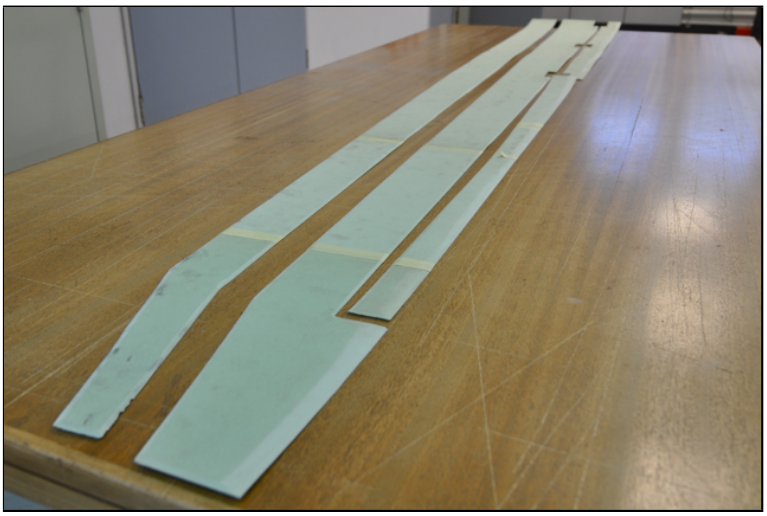

Figure 7.9 – *Sandwich core 2 mm thick ready for the layup of the bottom skin of the wing.*

Once ready, the skins were took out from the mold, and cleaned at the tip, root and leading edge with driller and sanding paper in the UAV Lab Workshop as is shown in Figure 7.12.

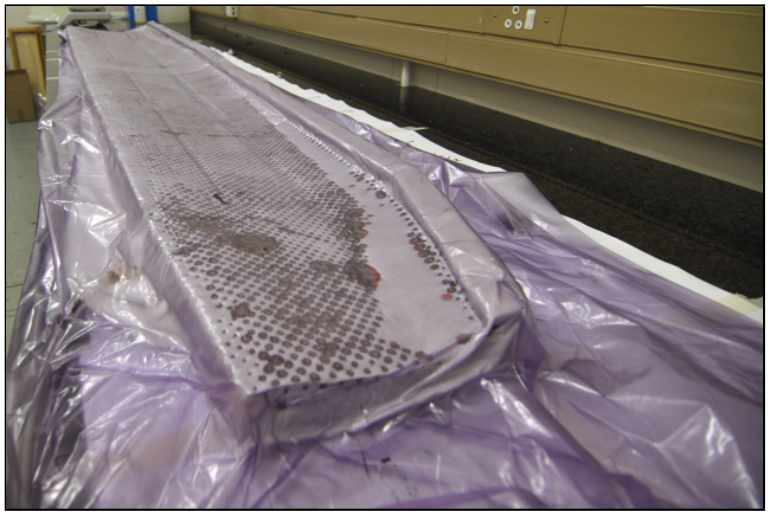

Figure 7.10 – *Bottom skin of the wing during the vacuum bag curing process.*

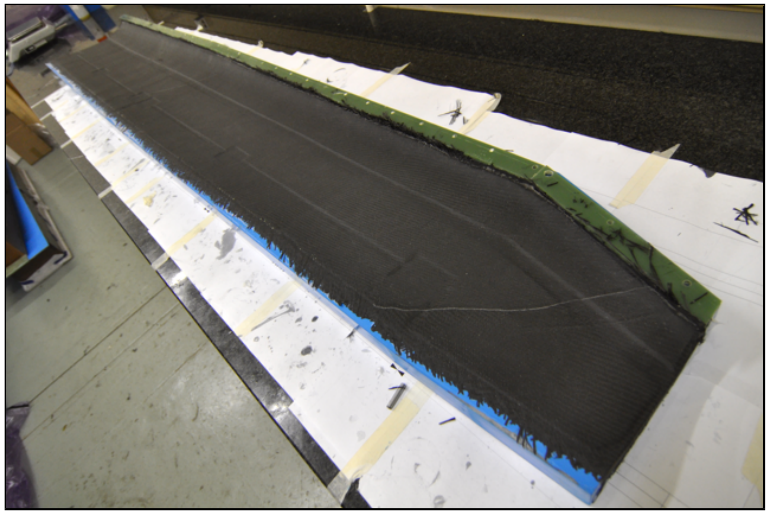

Figure 7.11 – *Bottom skin of the wing unpacked in the Composite Room.*

Figure 7.12 – *Bottom skin of the wing during the sanding process in the Workshop.*

7.5 Assembling

7.5.1 Preparation process

The assembling is one of the critical phases during the manufacturing of composite structures. Due to this reason, particular attention was paid and the process was made in collaboration with Alan Sutherland, Tim King, Pieter Rossouw and John Morgan (CSIR researcher). Once the ribs and the skins were sanded properly, the cotton flocs and resin were prepared. Because of the dihedral of the new wing, the alignment of the components at the root is essential to obtain a good product. To solve this a metal support was designed (Chapter 5), which has the proper angle to align the root rib, the spar and the pin at the same time. As shown in Figure 7.13, the four holes are necessary to screw the root rib at the support with the proper angle, the big rectangular section hole is used to align the spar and the small rectangular plates used to place the 10 *mm* pin in its position. The assembling started bonding the spar on the top skin. Once the resin under the spar was solid enough, the assembling of the ribs started from the root. This was a critical phase due to the necessity of accuracy for

the fuselage-wing joining. Thus, the root rib was screwed on the metal support (previously waxed) and than clamped at the mold (having so a perpendicular surface as reference for the dihedral, Figure 7.13).

Figure 7.13 – *Bonding phase simultaneously at the alignment of the pins using the metal support previously designed.*

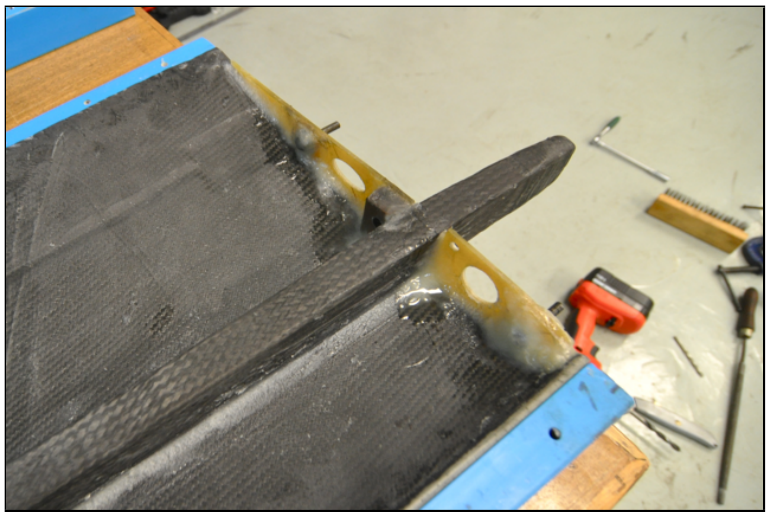

Figure 7.14 – *Particular of the root rib and pin supports bonded with cotton flocs and resin Ampreg21.*

Finally the two M6 screws were bonded (with the help of the metal support) to the rib following the junction design, as is shown in Figure 7.14.

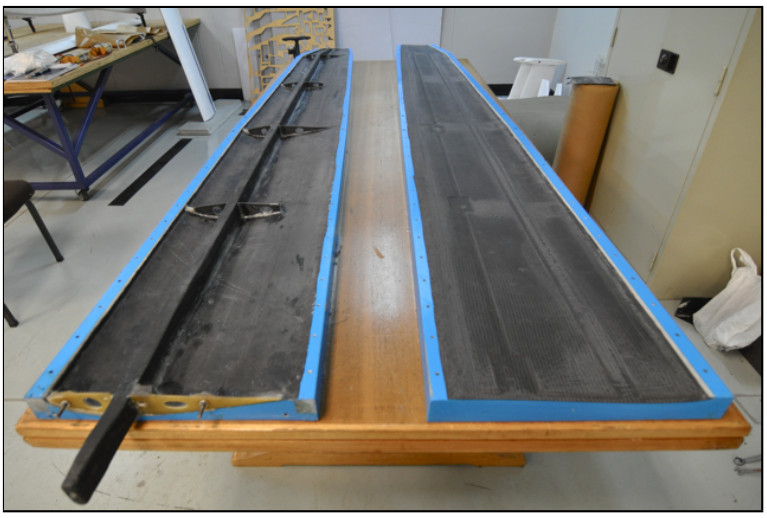

Figure 7.15 – *Wing skins ready to be bonded together.*

7.5.2 Final assembling

For the final assembling, some pieces of plasticine were placed on the spar and the ribs (Figure 7.16) in order to know the gap to fill up with the bonding line made of cotton flocs and resin. Obviously, the imperfection of a complete handmade manufacturing couldn't guarantee the certainty that the gap to fill up was the same for all the parts. After that the cotton flocs and resin were prepared and with the collaboration of Alan Sutherland and Pieter Rossouw they were placed all along the spar, the ribs, the leading and trailing edges. The mold was closed and the two half parts screwed together as is shown in Figure **??**. After 24 hours of curing the mold was opened and the wing cleaned. Than, in the Workshop of the UAV Lab, the trailing edge of the complete wing was cut and sanded with the help of Steve Haselum (CSIR researcher). The last step was the bonding of the M10 pin into the spar. This was made leaving enough play in the hole, thus the pin (critical for the dihedral of the wing) was bonded with the wing already on the aircraft Modular UAS, keeping the right dihedral by lifting

the wing tip by 2° (88° shown in Figure 7.19 because the reference was at 90°). Then it was left curing for 24 hours and the wing was ready to be tested.

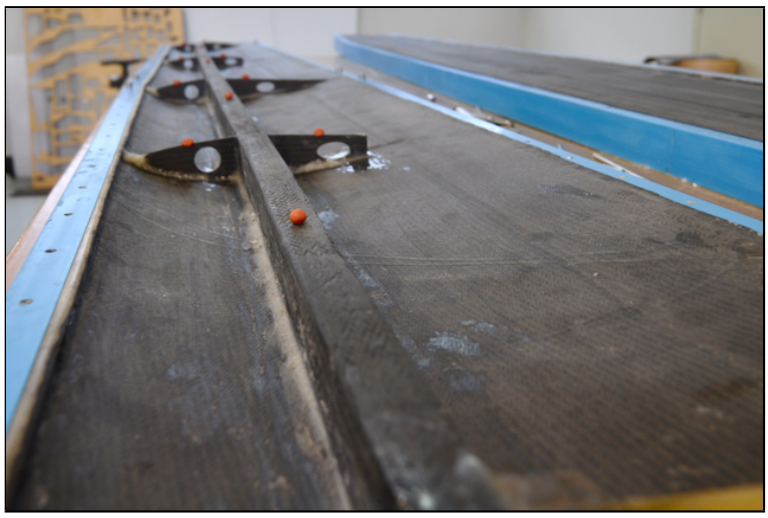

Figure 7.16 – *The plasticine was placed in order to know the actual gap between the several components to bond once the mold was closed.*

Figure 7.17 – *Molds closed together in order to bond the two skins in the right position.*

Figure 7.18 – *The new wing taken out of the mold. From the left: John Morgan, Steve Haselum, Francesco Perini, Alan Sutherland, Pieter Rossouw, a.k.a. The HammerTeam.*

Figure 7.19 – *Measuring the dihedral angle of the wing placed on the Modular UAS.*

Chapter 8

Static tests of the new wing

8.1 The whiffletree test rig and the preparation of the tests

The whiffletree for the static test was designed by John Monk and Neall Moore and it is situated in the UAV Lab of the Building 12. It's basically a hydraulic jack for which a group of several leverages was designed in order to reproduce the aspected flight loads.

Figure 8.1 – *Wing during tightening on the whiffletree before the first test.*

For the test of the new Modular UAS's wing, the loads and the application points were the same of Chapter 6, which were used for the MSC Patran/Nastran2010 simulation.

Figure 8.2 – *Wing ready for the test.*

The whiffletree has the two holes for the M6 pins fixed to its structure and the 10 *mm* hole and the dummy spar with pin (the one that should reproduce the spar pin coming from the central wing of the Modular UAS) floating on a leverage system. This system was designed by John Monk in order to transfer from the spar pin just bending moment, and not the shear force of the wing. The shear force and the torque moment were supposed to be transfered from the wing root to the fuselage by the M6 pins. Alan Sutherland and Pieter Rossouw calibrated the hydraulic jack with an electronic system to check the loads applied during the tests. To prevent damage to the wing, the loads application points were covered using pieces of cut foam around the wing section where the loads were supposed to be applied (see Figure 8.2).

8.2 Result of the Test 1

The first test was stopped at the 5 g flight condition due to the instability of the tip load application point. The foam around the tip was moving thus the test couldn't go ahead. The displacements of the wing tip are shown in the following table:

FLIGHT CONDITION	DISPLACEMENT [mm]
0.0 g	0.0
2.1 g	50.0
3.5 g	110.0
5.0 g	180.0

Table 8.1 – *Test 1 flight conditions and corresponding displacements at the wing tip.*

8.3 Result of the Test 2

The second test was stopped at 6.7 g flight condition due to the crack generation at the root rib bonding line. The root rib was touching the whiffletree during the bending of the wing, which had generated a compression of the rib itself against the whiffletree joining point. Apparently, the whiffletree load condition was different from the flight condition of the Modular UAS, due to the way of working of the floating system. The floating leverage, which host the dummy spar and the 10 mm hole, had an unbalanced condition of normal forces due to asymmetry. The displacements of the wing tip for this test are shown in Table 8.2. Unluckily it wasn't possible to register the displacement at the 6.7 g flight condition because just immediately before the crack generation the pressure in the hydraulic jack was preventively decreased. It is possible to see, instead, the displacement from the camera shots in Figure 8.3 for each of the flight condition listed in Table 8.2. The crack on the bonding line was more or less from the leading edge to the front spar web, at the top surface side of the root rib. It was repaired cutting the bonding line, sanding the area and making a new bonding line with enough smooth overlap on the old bonding line (see Figure 8.4). Epoxy fast curing was used to fill the gap and create the new bonding line.

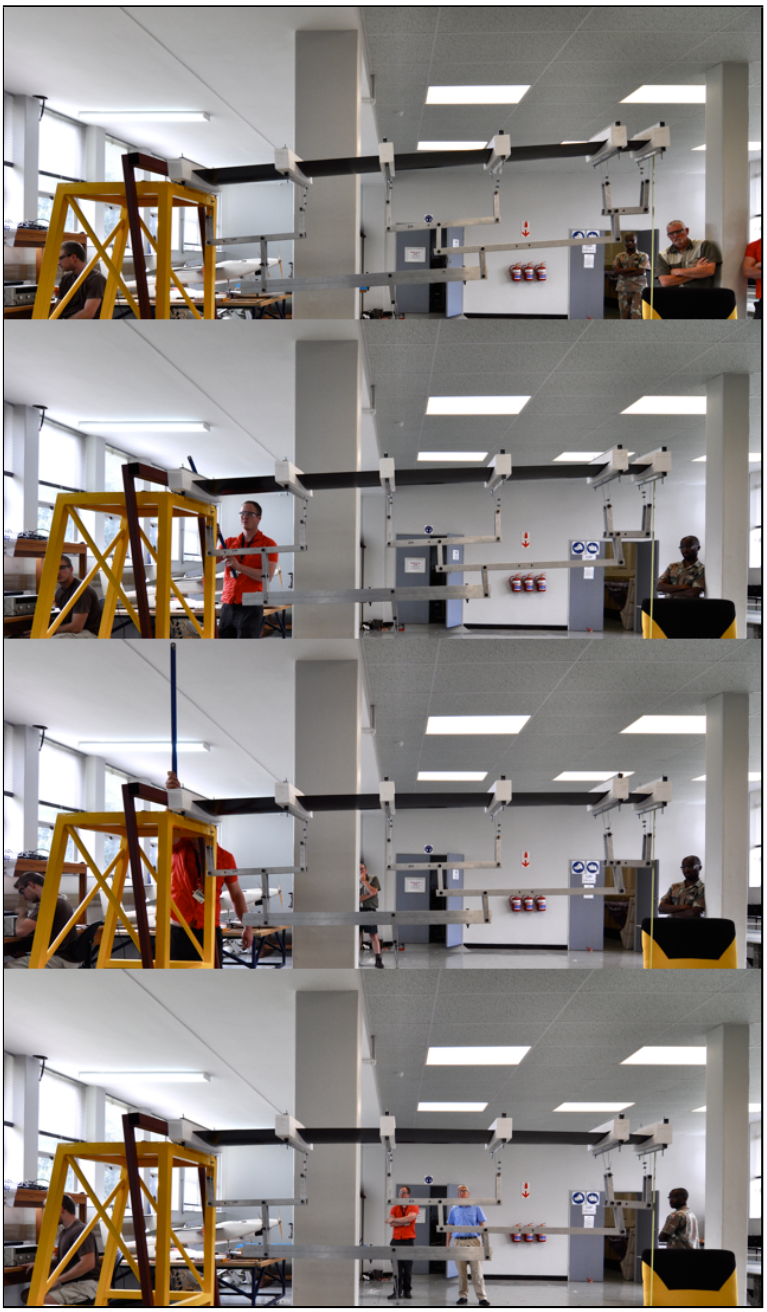

Figure 8.3 – *Test 2 camera shots for each flight condition listed in Table 8.2.*

FLIGHT CONDITION	DISPLACEMENT [mm]
0.0 g	0.0
2.1 g	50.0
3.5 g	113.0
5.0 g	187.0
6.7 g	/

Table 8.2 – *Test 2 flight conditions and corresponding displacements at the wing tip.*

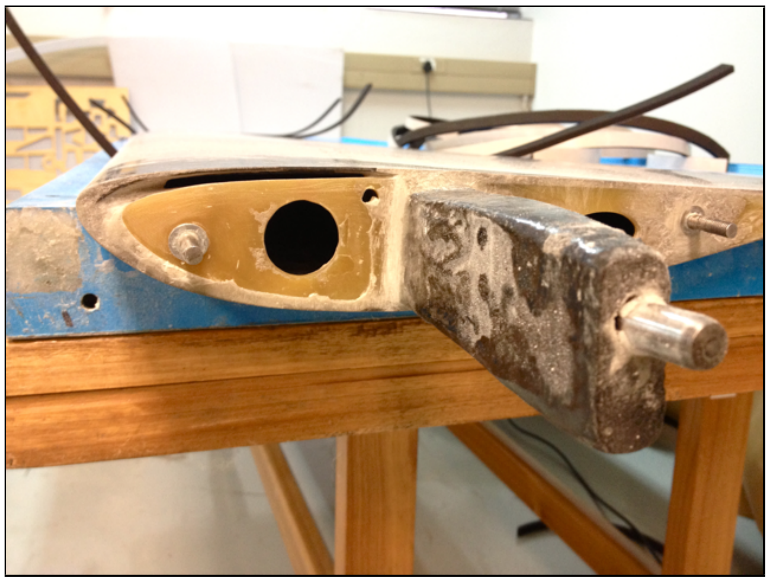

Figure 8.4 – *Repairing the damage at the bonding line of the root rib after Test 2.*

8.4 Result of the Test 3

To try to solve the issue, two spherical bearings M6 were putted into the 6 mm holes of the whiffletree junction. This permitted to not transfer bending moment by the M6 pins and to have enough clearance between the root rib and the whiffletree structure. Also, it was tried to reduce

the floating of the whiffletree in order to have less unbalanced (and not supposed) normal forces. Unfortunately, the third and last test was again stopped at the 6.7 g flight condition for the same problem of Test 2. The unbalanced condition of normal forces generated a bending moment around the vertical axes, hence the structure, in particular the root rib and the spar, worked in an unreal condition. This generated a crack along the bonding line of the root rib and a typical "x" crack on the spar web located in the area from the root rib to the external spar pin. This kind of crack is typical in a structure under compression.

FLIGHT CONDITION	**DISPLACEMENT [mm]**
0.0 g	0.0
3.5 g	114.0
6.7 g	/

Table 8.3 – *Test 3 flight conditions and corresponding displacements at the wing tip.*

Figure 8.5 – *Test 3 camera shots for the ghost 0 g condition and the 6.7 g condition.*

Figure 8.6 – *Damage at the bonding line of the root rib and at the front spar web out of the wing after Test 3.*

Thus, the bending moment around the vertical axes (not supposed to exist in the real) generated a compression on the front face of the spar web, as can be seen in Figure 8.6. Again it wasn't possible to register the displacement at the 6.7 g flight condition because just immediately the crack generation the pressure in the hydraulic jack was decreased.

FLIGHT CONDITION	DISPLACEMENT [mm]
0.0 g	0.0
2.1 g	56.0
3.5 g	97.3
5.0 g	139.0
6.7 g	190.0

Table 8.4 – *Nastran2010 simulation resulting displacements (from Chapter 6).*

It is possible to see, instead, the displacement from the camera shots in Figure 8.5 where the ghost 0 g condition and the 6.7 g condition are shown. This figure permits to see properly how big the deflection of the wing was. The registered displacements of the wing tip are shown in Table 8.3. As a comparison of the results obtained, the Nastran2010 simulation resulting

displacements are shown in Table 8.4. These results are not so far from the real ones, but still 20% different and apparently this is due to the floating system of the whiffletree, which affected the deflection, and consequently the measurement, of the wing during the tests.

Chapter 9

Conclusions

9.1 Conclusions

Starting from the study of several flight conditions of the CSIR's Modular UAS, this project got to the new wing structure concept and its relative mathematical and FEM analysis. The structure is still a little oversized as it is possible to see from the results of Chapter 6, and some optimization can be done in order to reduce the weight once the project gets to the actual delivery of the Modular UAS to the Department of Defense. Being still a prototype, the suggestions of John Monk was to have it stiffer to prevent damage during handling and transportation of the wing itself, and this should justify the over sizing of the wing structure. The manufacturing showed few difficulties, especially due to the dimension of the wing span (thus, handling of some parts and curing time of the resin too fast), to the correct angle of the spar needed and to the critical junction fuselage-wing alignment to get the designed dihedral. With regards to the handling of the parts, attention must be paid to the cutting of the structural fabrics: it is easy to lose the alignment of the fibers and consequently to have some imperfection during the layup. In the case of an optimized structure, it can be dangerous where there are stress deviations not expected or pockets without resin. Pre-pregs fabrics could be considered to have safer properties of the materials. Looking at the curing process, autoclave with vacuum bag could be considered to bring to higher properties of the materials instead. Even so, the wing has been delivered with an excellent finish surface, with a working junction with the aircraft and with no evidence of defects. The weight of each wing component is shown in the following Table 9.1.

COMPONENT	WEIGHT [kg]
Spar	0.772
Ribs	0.103
Skin	2.830
Bonding	0.500

Table 9.1 – *Weight of each wing component.*

for a total weight of the wing equals to 4.205 kg, which is below the first estimated weight of 4.5 kg made at the beginning of all this work. Costs of the development for the new Modular UAS's wing remained below the budget arranged beforehand. The wing has been successfully tested to 6.7 g flight condition even if the testing goal was 7 g; this was due to the damage caused by the whiffletree. My personal suggestion is that CSIR DPSS ASC's whiffletree must be corrected immediately to not occur the same issues with other wings to test. Firstly because with these unbalanced normal forces, it doesn't reproduce exactly the flight load case as it is supposed to be, and secondly, but not less important, because it risks to damage the wing where the different whiffletree load case is not aspected. Eventually, the ASC Research Group Leader John Monk was glad to fly the wing in the short term. This wing provides to carry, on the CSIR's Modular UAS, 10 kg more fuel (petrol, diesel or fuel cells) in order to recharge the batteries with two small combustion engines during the flight and to have an higher aerodynamic efficiency E. This was necessary to extended endurance version of the Modular UAS to 8 hours operating for boarders safety guarding.

Appendix A

Appendix

A.1 Matlab script for the complete V-n diagram

```
clear all
clc
set(0,'defaulttextinterpreter','none')


% DATA %

rho=1.225
rho_imp=0.05
m=50
W=m*9.81
S=1.911
b=6
mgc=0.33
Clmax=1.6757
Clmin=0.4
nmax=6 % FAR 23.335 for acrobatic airplanes
nmin=-3 % FAR 23.335 for acrobatic airplanes
Wing_loading=W/S
Wing_loading_BI=(2.2*m)/(10.7*S)
AR=(b^2)/S
e=0.97
Clalpha=(2*pi*AR)/(2+sqrt((AR^2/e^2)+4))
Vc=(33*sqrt(Wing_loading_BI))*0.514 % Vc in knots=0.514 m/s
Vd=1.55*Vc % FAR 23.335 for acrobatic airplanes


% LOAD FACTOR DIAGRAM %

Vstp=sqrt((2*W)/(rho*S*Clmax))
```

```
Vstn=sqrt((2*W)/(rho*S*Clmin))

Va=sqrt((nmax*2*W)/(rho*S*Clmax))
Vg=sqrt(((-1*nmin)*2*W)/(rho*S*Clmin))
V1=[Vstp:0.1:Vd]
n1=(0.5*rho*S*Clmax*(V1.^2))/(W)
set(0,'defaultlinelinewidth',0.8)
plot(V1,n1,'k')
axis([0,80,-4,9])
xlabel('Velocity [\textit{m/s}]')
ylabel('Load factor')
set(gca,'YTick',[-5 -4 -3 -2 -1 0 1 2 3 4 5 6 7 8 9 10])
hold on

x1=[Va Vd]
y1=[nmax nmax]
line(x1,y1,'Color','k')
hold on

plot([Vd;Vd],[nmin;nmax],'k')
hold on

plot([Vd;Vd],[nmin;nmax],'b','LineWidth',1.1)
hold on

V2=[0:0.1:Vstn]
n2=-(0.5*rho*S*Clmin*(V2.^2))/(W);
plot(V2,n2,'k--')
hold on

V3=[0:0.1:Vstp]
n3=(0.5*rho*S*Clmax*(V3.^2))/(W)
plot(V3,n3,'k--')
hold on

V41=[Vstn:0.1:Vg]
n41=-(0.5*rho*S*Clmin*(V41.^2))/(W)
plot(V41,n41,'k')
hold on

V4=[Vstn:0.1:Vg]
n4=-(0.5*rho*S*Clmin*(V4.^2))/(W)
plot(V4,n4,'b','LineWidth',1.1)
hold on

plot([Vg;Vd],[nmin,nmin],'k')
hold on

plot([Vg;Vd],[nmin,nmin],'b','LineWidth',1.1)
hold on
```

```
81
82  plot([Vstp;Vstp],[0;1],'k')
83  hold on
84
85  plot([Vstp;Vstp],[0;1],'b','LineWidth',1.1)
86  hold on
87
88  plot([Vstn;Vstn],[0;-1],'k')
89  hold on
90
91  plot([Vstn;Vstn],[0;-1],'b','LineWidth',1.1)
92  hold on
93
94  plot([Va;Va],[0,nmax],'k--')
95  hold on
96
97  plot([Vg;Vg],[0,nmin],'k--')
98  hold on
99
100 grid on
101
102 text(16.31,0.3,'$V_{st+}$')
103 text(32.87,-0.3,'$V_{st-}$')
104 text(34.73,0.3,'$V_A$')
105 text(56.56,-0.3,'$V_G$')
106
107 text(61.47,0.3,'$V_D$')
108
109 text(2,6,'$n_{max}$')
110 text(2,-3,'$n_{min}$')
111
112
113 % WIND GUST DIAGRAM %
114
115 mug=(2*Wing_loading)/(rho*mgc*Clalpha*9.81) % mass ratio
116 kg=(0.88*mug)/(5.3+mug) % gust alleviation factor
117 Vgc=50*0.3048 % FAR 23.335 for common airplanes in m/s
118 Vgd=25*0.3048 % FAR 23.335 for common airplanes in m/s
119
120 V5=[0:0.1:Vd]
121 n5=1+(V5.*kg*rho*S*Clalpha*Vgc)/(2*W)
122 h5=plot(V5,n5,'k--')
123 hold on
124
125 V6=[0:0.1:Vd]
126 n6=1-(V6.*kg*rho*S*Clalpha*Vgc)/(2*W)
127 plot(V6,n6,'k--')
128 hold on
129
130 V7=[0:0.1:Vd]
```

```
n7=1+(V7.*kg*rho*S*Clalpha*Vgd)/(2*W)
h7=plot(V7,n7,'k--')
hold on

V8=[0:0.1:Vd]
n8=1-(V8.*kg*rho*S*Clalpha*Vgd)/(2*W)
plot(V8,n8,'k--')
hold on

[xi,yi]=polyxpoly(V1,n1,V5,n5) % intersection of the curves
mapshow(xi,yi,'DisplayType','point','Marker','o')
hold on
plot([0;80],[0,0],'k')
hold on


% FLIGHT ENVELOPE DIAGRAM %

yii=1+(Vd*kg*rho*S*Clalpha*Vgd)/(2*W)
% mapshow(Vd,yii,'DisplayType','point','Marker','o')

x7=[xi Vd]
y7=[yi yii]
h7=line(x7,y7,'Color','k')
hold on

[xiii,yiii]=polyxpoly(x1,y1,x7,y7)
hold on


x11=[xiii Vd]
y11=[nmax nmax]
line(x11,y11,'LineWidth',1.1)
hold on

V11=[Vstp:0.1:xi]
n11=(0.5*rho*S*Clmax*(V11.^2))/(W)
plot(V11,n11,'b','LineWidth',1.1)
hold on

x8=[xi xiii]
y8=[yi yiii]
h8=line(x8,y8,'Color','b','LineWidth',1.1)
hold on

plot([xi;xi],[0,yi],'k--')
text(42.39,0.3,'$V_C$')
hold on

hleg=legend([h8],'Flight envelope','Location','NorthWest')
```

```
181
182 %laprint
```

A.2 Matlab scritps for the internal loads

A.2.1 Matlab script for distributed load, shear force and bending moment at the 41.89 m/s - 7.02 g condition

```
1  clear all
2  clc
3  set(0,'defaulttextinterpreter','none')
4
5  % DATA %
6
7  m=50
8  mw=11
9  rho=1.225
10 S=1.91
11 Sc=0.36
12 Slr=0.775
13 Vc=41.89
14 nmax=7.02
15 Clmax=1.676
16
17 yp=[0 0.225 1.4 2.5]
18 cp=[0.160 0.255 0.335 0.360]
19
20 b1=yp(2)-yp(1)
21 h1=cp(2)-cp(1)
22
23 b2=yp(3)-yp(2)
24 h2=cp(3)-cp(2)
25
26 b3=yp(4)-yp(3)
27 h3=cp(4)-cp(3)
28
29 m1=h1/b1
30 m2=h2/b2
31 m3=h3/b3
32
33 q1=0.160
34 q2=cp(2)-m2*yp(2)
```

```
q3=cp(3)-m3*yp(3)


y1=[yp(1):0.001:yp(2)]
c1=m1*y1+q1

y2=[yp(2):0.001:yp(3)]
c2=m2*y2+q2

y3=[yp(3):0.001:yp(4)]
c3=m3*y3+q3


% DISTRIBUTED LOAD &

L=0.5*rho*S*(Vc)^2*Clmax
W=m*9.81
Wing_loading=L/S
Mass_loading=((-nmax*mw)*9.81)/S
Wing_loading_mass=(nmax*(m-mw)*9.81)/S


p1=c1*Wing_loading_mass

p2=c2*Wing_loading_mass

p3=c3*Wing_loading_mass

mass1=c1*Mass_loading

mass2=c2*Mass_loading

mass3=c3*Mass_loading


% SHEAR %

T1=Wing_loading_mass*((m1/2)*(y1.^2)+q1*y1)

Tp1=Wing_loading_mass*((m1/2)*(yp(2)^2)+q1*yp(2))
Tp12=Wing_loading_mass*((m2/2)*(yp(2)^2)+q2*yp(2))
Tc12=Tp1-Tp12

T2=Wing_loading_mass*((m2/2)*(y2.^2)+q2*y2)+Tc12

Tp2=Wing_loading_mass*((m2/2)*(yp(3)^2)+q2*yp(3))+Tc12
Tp23=Wing_loading_mass*((m3/2)*(yp(3)^2)+q3*yp(3))
Tc23=Tp2-Tp23

T3=Wing_loading_mass*((m3/2)*(y3.^2)+q3*y3)+Tc23
```

```
85
86  Tr1=Wing_loading_mass*((m3/2)*(yp(1)^2)+q3*yp(1))
87  Tr2=Wing_loading_mass*((m3/2)*(yp(2)^2)+q3*yp(2))+Tc23
88  Tr3=Wing_loading_mass*((m3/2)*(0.8125^2)+q3*0.8125)+Tc23
89  Tr4=Wing_loading_mass*((m3/2)*(yp(3)^2)+q3*yp(3))+Tc23
90  Tr5=Wing_loading_mass*((m3/2)*(1.950^2)+q3*1.950)+Tc23
91  Tr6=Wing_loading_mass*((m3/2)*(yp(4)^2)+q3*yp(4))+Tc23
92
93
94  % BENDING MOMENT %
95
96  M1=Wing_loading_mass*((m1/6)*(y1.^3)+(q1/2)*(y1.^2))
97  plot(y1,M1,'k')
98  xlabel('Wing semi-span [\textit{m}]')
99  ylabel('Bending moment [\textit{Nm}]')
100 hold on
101
102 Mp1=Wing_loading_mass*((m1/6)*(yp(2)^3)+(q1/2)*(yp(2)^2))
103 Mp12=Wing_loading_mass*((m2/6)*(yp(2)^3)+(q2/2)*(yp(2)^2))...
104     +Tc12*yp(2)
105 Mc12=Mp1-Mp12
106
107 M2=Wing_loading_mass*((m2/6)*(y2.^3)+(q2/2)*(y2.^2))+...
108     (Tc12*y2)+Mc12
109 plot(y2,M2,'k')
110 hold on
111
112 Mp2=Wing_loading_mass*((m2/6)*(yp(3)^3)+(q2/2)*(yp(3)^2))...
113     +(Tc12*yp(3))+Mc12
114 Mp23=Wing_loading_mass*((m3/6)*(yp(3)^3)+(q3/2)*(yp(3)^2))...
115     +Tc23*yp(3)
116 Mc23=Mp2-Mp23
117
118 M3=Wing_loading_mass*((m3/6)*(y3.^3)+(q3/2)*(y3.^2))+...
119     Tc23*y3+Mc23
120 plot3=plot(y3,M3,'k')
121 hold on
122
123 Mr1=Wing_loading_mass*((m3/6)*(yp(1)^3)+(q3/2)*(yp(1)^2))...
124     +Tc23*yp(1)
125 Mr2=Wing_loading_mass*((m3/6)*(yp(2)^3)+(q3/2)*(yp(2)^2))...
126     +Tc23*yp(2)+Mc23
127 Mr3=Wing_loading_mass*((m3/6)*(0.8125^3)+(q3/2)*(0.8125^2))...
128     +Tc23*0.8125+Mc23
129 Mr4=Wing_loading_mass*((m3/6)*(yp(3)^3)+(q3/2)*(yp(3)^2))...
130     +Tc23*yp(3)+Mc23
131 Mr5=Wing_loading_mass*((m3/6)*(1.950^3)+(q3/2)*(1.950^2))...
132     +Tc23*1.950+Mc23
133 Mr6=Wing_loading_mass*((m3/6)*(yp(4)^3)+(q3/2)*(yp(4)^2))...
134     +Tc23*yp(4)+Mc23
```

```
mapshow(yp(4),Mr6,'DisplayType','point','Marker','o')
hold on

grid on

hleg=legend([plot3],'Bending moment [\textit{Nm}]',...
'Location','NorthWest')

%laprint
```

A.2.2 Matlab script for torque moment at the 60.98 m/s - 6 g condition with 7° aileron deflection

```
clear all
clc
set(0,'defaulttextinterpreter','none')


% DATA %

m=50
mw=11
rho=1.225
S=1.91
Sc=0.36
Slr=0.775
Vapp=20.558
Vc=41.89
Vd=60.98
n=6

yspantr=[
-3.0000
-2.9776
-2.9626
-2.9476
-2.9326
-2.9176
-2.9026
-2.8876
-2.8727
-2.8577
-2.8428
-2.8279
-2.8131
-2.7985
-2.7852
```

```
-2.7359
-2.6575
-2.5792
-2.5009
-2.4226
-2.3442
-2.2659
-2.1876
-2.1093
-2.0310
-1.9527
-1.8744
-1.7961
-1.7180
-1.6408
-1.5634
-1.4900
-1.4167
-1.3434
-1.2701
-1.1967
-1.1234
-1.0501
-0.9768
-0.9034
-0.8301
-0.7568
-0.6835
-0.6102
-0.5372
-0.5000]

yspan=yspantr+3*ones(46,1)

Mt=[0
-0.058732121
-0.129319299
-0.211058093
-0.303767493
-0.407566588
-0.522895583
-0.650194647
-0.789347657
-0.943536237
-1.112248548
-1.298961662
-1.506212411
-1.738227396
-1.986470221
-3.173351706
```

```
-5.227981546
-7.400481419
-9.681585231
-12.06740210
-14.54948293
-17.13156874
-19.81131730
-22.59168633
-25.46643111
-28.43499591
-31.49220691
-34.62757248
-37.79709467
-40.87462345
-43.13136023
-45.12042801
-47.05535265
-48.97474145
-50.89487436
-52.82291434
-54.76422089
-56.71686522
-58.68488589
-60.66811462
-62.66833648
-64.68608094
-66.72064177
-68.77084790
-70.82916076
-72.37276172]


% TORQUE MOMENT AT VD AND N=6 WITH AILERON7 %

p=polyfit(yspan,Mt,6)
xx=linspace(yspan(1), yspan(46))
yy=polyval(p,xx)
plottorque=plot(yspan,Mt,'k')

xlabel('Wing semi-span [\textit{m}]')
ylabel('Torque moment [\textit{Nm}]')
hold on

Mtr1=Mt(1)
Mtr2=Mt(15)
Mtr3=Mt(23)
Mtr4=Mt(31)
Mtr5=Mt(38)
Mtr6=Mt(46)
mapshow(yspan(46),Mtr6,'DisplayType','point','Marker','o')
```

```
hold on

grid on

hleg=legend([plottorque],...
'$M_{t}$ at $V_{D}$ and $\delta=7^{\circ}$ [\textit{Nm}]',...
'Location','SouthWest')

%laprint
```

A.3 Matlab scritps for the stress conditions

A.3.1 Matlab script for the concentrated loads applied on the ribs of the wing

```
clear all
clc
set(0,'defaulttextinterpreter','none')


% DATA %

m=50
mw=11
rho=1.225
S=1.91
Sc=0.36
Slr=0.775
Vc=41.89
nmax=7.02
Clmax=1.676

yp=[0 0.225 1.4 2.5]
cp=[0.160 0.255 0.335 0.360]

b1=yp(2)-yp(1)
h1=cp(2)-cp(1)

b2=yp(3)-yp(2)
h2=cp(3)-cp(2)

b3=yp(4)-yp(3)
```

```
h3=cp(4)-cp(3)

m1=h1/b1
m2=h2/b2
m3=h3/b3

q1=0.160
q2=cp(2)-m2*yp(2)
q3=cp(3)-m3*yp(3)


y1=[yp(1):0.001:yp(2)]
c1=m1*y1+q1

y2=[yp(2):0.001:yp(3)]
c2=m2*y2+q2

y3=[yp(3):0.001:yp(4)]
c3=m3*y3+q3


% LOAD ON RIB 1 %

L=0.5*rho*S*(Vc)^2*Clmax
W=m*9.81
Wing_loading_mass=(nmax*(m-mw)*9.81)/S

p1=c1*Wing_loading_mass
half12=yp(2)/2
R1=((m1*Wing_loading_mass*half12^2)/2+q1*Wing_loading_mass*...
    half12)


% LOAD ON RIB 2 %

p2=c2*Wing_loading_mass
R2n=((m1*Wing_loading_mass*yp(2)^2)/2+q1*Wing_loading_mass*...
    yp(2))-((m1*Wing_loading_mass*half12^2)/2+q1*...
    Wing_loading_mass*half12)
half23=(yp(3)-yp(2))/4+yp(2)
R2p=((m2*Wing_loading_mass*half23^2)/2+q2*Wing_loading_mass*...
    half23)-((m2*Wing_loading_mass*yp(2)^2)/2+q2*...
    Wing_loading_mass*yp(2))
R2=R2n+R2p


% LOAD ON RIB 3 %

half34=(yp(3)-yp(2))*3/4+yp(2)
R3=((m2*Wing_loading_mass*half34^2)/2+q2*Wing_loading_mass*...
```

```
78      half34)-((m2*Wing_loading_mass*half23^2)/2+q2*...
79      Wing_loading_mass*half23)
80
81
82  % LOAD ON RIB 4 %
83
84  p3=c3*Wing_loading_mass
85  R4n=((m2*Wing_loading_mass*yp(3)^2)/2+q2*Wing_loading_mass*...
86      yp(3))-((m2*Wing_loading_mass*half34^2)/2+q2*...
87      Wing_loading_mass*half34)
88  half45=(yp(4)-yp(3))/4+yp(3)
89  R4p=((m3*Wing_loading_mass*half45^2)/2+q3*Wing_loading_mass*...
90      half45)-((m3*Wing_loading_mass*yp(3)^2)/2+q3*...
91      Wing_loading_mass*yp(3))
92  R4=R4n+R4p
93
94
95  % LOAD ON RIB 5 %
96
97  half56=(yp(4)-yp(3))*3/4+yp(3)
98  R5=((m3*Wing_loading_mass*half56^2)/2+q3*Wing_loading_mass*...
99      half56)-((m3*Wing_loading_mass*half45^2)/2+q3*...
100     Wing_loading_mass*half45)
101
102
103 % LOAD ON RIB 6 %
104
105 R6=((m3*Wing_loading_mass*yp(4)^2)/2+q3*Wing_loading_mass*...
106     yp(4))-((m3*Wing_loading_mass*half56^2)/2+q3*...
107     Wing_loading_mass*half56)
108
109
110 % CONFIRM OF THE RESULTS AND ULTIMATE LOADS %
111
112 Rtot=R1+R2+R3+R4+R5+R6
113
114 Scw=0.36
115 Ltotcw=0.5*rho*Scw*(Vc)^2*Clmax-(Scw/S)*mw*9.81*nmax
116 Ltot=Rtot*2+Ltotcw
117 deltaL=Ltot+(mw*9.81*nmax)-L
118
119 yp1=yp(1)
120 yp2=yp(2)
121 yp3=(yp(3)-yp(2))/2+yp(2)
122 yp4=yp(3)
123 yp5=(yp(4)-yp(3))/2+yp(3)
124 yp6=yp(4)
125
126 sf1=1.5
127 sf2=1.2
```

```

R1UL=R1*sf1*sf2
R2UL=R2*sf1*sf2
R3UL=R3*sf1*sf2
R4UL=R4*sf1*sf2
R5UL=R5*sf1*sf2
R6UL=R6*sf1*sf2
```

A.3.2 Matlab script for the shear center of the critical section at the root and semimonocoque study for shear and normal stress

```
clear all
clc
set(0,'defaulttextinterpreter','none')


% DATA %

Tx=1
Ty=1
Troot=1963.08
Mtroot=-130271
Mbroot=2264040
sigmamaxskin=249.763
sigmamaxspar=1073.4
taumaxskin=sigmamaxskin/2
sigmamaxrib6=120    % Interglass 92149/Epoxy %
taumaxrib6=25.1


L12=96.61
L23=54.5
L34=25.03
L45=114.31
L56=126.57
L67=129.12
L78=114.92
L89=25.01
L91=55.26
L93=50.47
L84=49.68

t12=1
t23=1
t34=1+0.6
t45=1
```

```
t56=1
t67=1
t78=1
t89=1+0.6
t91=1
t93=0.6
t84=0.6

Ac3=(2*25.03)/2
Ac4=(2*25.03)/2
Ac8=(2*25.03)/2
Ac9=(2*25.03)/2

A1=(t12*L12)/2+(t91*L91)/2
A2=(t12*L12)/2+(t23*L23)/2
A3=(t23*L23)/2+(t34*L34)/2+(t93*L93)/2+Ac3
A4=(t34*L34)/2+(t45*L45)/2+(t84*L84)/2+Ac4
A5=(t45*L45)/2+(t56*L56)/2
A6=(t56*L56)/2+(t67*L67)/2
A7=(t67*L67)/2+(t78*L78)/2
A8=(t78*L78)/2+(t89*L89)/2+(t84*L84)/2+Ac8
A9=(t89*L89)/2+(t91*L91)/2+(t93*L93)/2+Ac9


% SECTION CHARATERISTICS - SDR IN (2) %

x1=0
x2=0
x3=54.5
x4=54.5+25
x5=54.5+25+114.06
x6=54.5+25+114.06+126.44
x7=54.5+25+114.06
x8=54.5+25
x9=54.5

y1=42.18
y2=0
y3=-0.08
y4=1.06
y5=8.51
y6=11.50
y7=37.63
y8=50.74
y9=50.39

Atot=A1+A2+A3+A4+A5+A6+A7+A8+A9
xcg=(A1*x1+A2*x2+A3*x3+A4*x4+A5*x5+A6*x6+A7*x7+A8*x8+A9*x9)...
    /Atot
ycg=(A1*y1+A2*y2+A3*y3+A4*y4+A5*y5+A6*y6+A7*y7+A8*y8+A9*y9)...
```

```
86      /Atot
87
88  Ixx=A1*(y1-ycg)^2+A2*(y2-ycg)^2+A3*(y3-ycg)^2+A4*(y4-ycg)^2+...
89      A5*(y5-ycg)^2+A6*(y6-ycg)^2+A7*(y7-ycg)^2+A8*(y8-ycg)^2+...
90      A9*(y9-ycg)^2
91  Iyy=A1*(x1-xcg)^2+A2*(x2-xcg)^2+A3*(x3-xcg)^2+A4*(x4-xcg)^2+...
92      A5*(x5-xcg)^2+A6*(x6-xcg)^2+A7*(x7-xcg)^2+A8*(x8-xcg)^2+...
93      A9*(x9-xcg)^2
94  Ixy=A1*(y1-ycg)*(x1-xcg)+A2*(y2-ycg)*(x2-xcg)+A3*(y3-ycg)*...
95      (x3-xcg)+A4*(y4-ycg)*(x4-xcg)+A5*(y5-ycg)*(x5-xcg)+A6*...
96      (y6-ycg)*(x6-xcg)+A7*(y7-ycg)*(x7-xcg)+A8*(y8-ycg)*...
97      (x8-xcg)+A9*(y9-ycg)*(x9-xcg)
98
99  alpha=0.5*atan((2*Ixy)/(Iyy-Ixx))
100
101
102 % SHEAR CENTER X-COORDINATE (OPENING THE PANELS 12-93-84) %
103
104 q2openx=-(Ty/Ixx)*A2*(y2-ycg)
105 q3openx=q2openx-(Ty/Ixx)*A3*(y3-ycg)
106 q4openx=q3openx-(Ty/Ixx)*A4*(y4-ycg)
107 q5openx=q4openx-(Ty/Ixx)*A5*(y5-ycg)
108 q6openx=q5openx-(Ty/Ixx)*A6*(y6-ycg)
109 q7openx=q6openx-(Ty/Ixx)*A7*(y7-ycg)
110 q8openx=q7openx-(Ty/Ixx)*A8*(y8-ycg)
111 q9openx=q8openx-(Ty/Ixx)*A9*(y9-ycg)
112
113 Omega1=3784.29
114 Omega2=1256.31
115 Omega3=6127.43
116 Omega91=1213.36
117 Omega89=623.8
118 Omega78=3581.62
119 Omega67=4931.40
120 Omega56=409.06
121 Omega45=256.87
122
123
124 A=[((L12/t12)+(L23/t23)+(L93/t93)+(L91/t91)) (-L93/t93) 0;...
125     (-L93/t93) ((L93/t93)+(L34/t34)+(L84/t84)+(L89/t89)) ...
126     (-L84/t84);0 (-L84/t84) ((L84/t84)+(L45/t45)+(L56/t56)+...
127     (L67/t67)+(L78/t78))]
128
129 B=[(-q2openx*(L23/t23)-q9openx*(L91/t91)) (-q3openx*(L34/...
130     t34)-q8openx*(L89/t89)) (-q4openx*(L45/t45)-q5openx*...
131     (L56/t56)-q6openx*(L67/t67)-q7openx*(L78/t78))]
132
133 C=inv(A)
134 C=C'
135
```

```
136 Q=(B*C)
137
138 dx=(2*Omega1*Q(1)+2*Omega2*Q(2)+2*Omega3*Q(3)+2*Omega91*...
139     q9openx+2*Omega89*q8openx+2*Omega78*q7openx+2*Omega67*...
140     q6openx+2*Omega56*q5openx+2*Omega45*q4openx)/Ty
141
142
143 % SHEAR CENTER Y-COORDINATE (OPENING THE PANELS 12-93-84) %
144
145 q2openy=-(Tx/Iyy)*A2*(x2-xcg)
146 q3openy=q2openy-(Tx/Iyy)*A3*(x3-xcg)
147 q4openy=q3openy-(Tx/Iyy)*A4*(x4-xcg)
148 q5openy=q4openy-(Tx/Iyy)*A5*(x5-xcg)
149 q6openy=q5openy-(Tx/Iyy)*A6*(x6-xcg)
150 q7openy=q6openy-(Tx/Iyy)*A7*(x7-xcg)
151 q8openy=q7openy-(Tx/Iyy)*A8*(x8-xcg)
152 q9openy=q8openy-(Tx/Iyy)*A9*(x9-xcg)
153
154 A=[((L12/t12)+(L23/t23)+(L93/t93)+(L91/t91)) (-L93/t93) 0;...
155     (-L93/t93) ((L93/t93)+(L34/t34)+(L84/t84)+(L89/t89)) ...
156     (-L84/t84);0 (-L84/t84) ((L84/t84)+(L45/t45)+(L56/t56)+...
157     (L67/t67)+(L78/t78))]
158
159 B=[(-q2openy*(L23/t23)-q9openy*(L91/t91)) (-q3openy*(L34/...
160     t34)-q8openy*(L89/t89)) (-q4openy*(L45/t45)-q5openy*...
161     (L56/t56)-q6openy*(L67/t67)-q7openy*(L78/t78))]
162
163 C=inv(A)
164 C=C'
165
166 Q=(B*C)
167
168 dy=(2*Omega1*Q(1)+2*Omega2*Q(2)+2*Omega3*Q(3)+2*Omega91*...
169     q9openy+2*Omega89*q8openy+2*Omega78*q7openy+2*Omega67*...
170     q6openy+2*Omega56*q5openy+2*Omega45*q4openy)/(-Tx)
171
172
173 % SECTION 6 %
174
175 q2open=-(Troot/Ixx)*A2*(y2-ycg)
176 q3open=q2open-(Troot/Ixx)*A3*(y3-ycg)
177 q4open=q3open-(Troot/Ixx)*A4*(y4-ycg)
178 q5open=q4open-(Troot/Ixx)*A5*(y5-ycg)
179 q6open=q5open-(Troot/Ixx)*A6*(y6-ycg)
180 q7open=q6open-(Troot/Ixx)*A7*(y7-ycg)
181 q8open=q7open-(Troot/Ixx)*A8*(y8-ycg)
182 q9open=q8open-(Troot/Ixx)*A9*(y9-ycg)
183
184 A=[(2*Omega1) (2*Omega2) (2*Omega3);((L12/t12)+(L23/t23)+...
185     (L93/t93)+(L91/t91)+((L93*Omega1)/(t93*Omega2))) ((-L93/...
```

```
    t93)+((-L93*Omega1)/(t93*Omega2))+((-L34*Omega1)/(t34*...
    Omega2))+((-L84*Omega1)/(t84*Omega2))+((-L89*Omega1)/...
    (t89*Omega2))) ((L84*Omega1)/(t84*Omega2));(-L93/t93) ...
    ((L93/t93)+(L34/t34)+(L84/t84)+(L89/t89)+((L84*Omega2)/...
    (t84*Omega3))) ((-L84/t84)+((-L84*Omega2)/(t84*...
    Omega3))+((-L45*Omega2)/(t45*Omega3))+((-L56*...
    Omega2)/(t56*Omega3))+((-L67*Omega2)/(t67*Omega3))+...
    ((-L78*Omega2)/(t78*Omega3)))]

B=[((Troot*dx+Mtroot)-2*Omega91*q9open-2*Omega89*q8open-...
    2*Omega78*q7open-2*Omega67*q6open-2*Omega56*q5open-...
    2*Omega45*q4open) (-q2open*(L23/t23)-q9open*(L91/t91)+...
    q3open*((L34*Omega1)/(t34*Omega2))+q8open*((L89*Omega1)/...
    (t89*Omega2))) (-q3open*(L34/t34)-q8open*(L89/t89)+...
    q4open*((L45*Omega2)/(t45*Omega3))+q5open*((L56*Omega2)/...
    (t56*Omega3))+q6open*((L67*Omega2)/(t67*Omega3))+...
    q7open*((L78*Omega2)/(t78*Omega3)))]

C=inv(A)
C=C'

Q=(B*C)

q1=Q(1)
q2=q2open+Q(1)
q3=q3open+Q(2)
q4=q4open+Q(3)
q5=q5open+Q(3)
q6=q6open+Q(3)
q7=q7open+Q(3)
q8=q8open+Q(2)
q9=q9open+Q(1)
q10=Q(2)-Q(1)
q11=Q(2)-Q(3)

sigma1=-(Mbroot/Ixx)*(y1-ycg)
sigma2=-(Mbroot/Ixx)*(y2-ycg)
sigma3=-(Mbroot/Ixx)*(y3-ycg)
sigma4=-(Mbroot/Ixx)*(y4-ycg)
sigma5=-(Mbroot/Ixx)*(y5-ycg)
sigma6=-(Mbroot/Ixx)*(y6-ycg)
sigma7=-(Mbroot/Ixx)*(y7-ycg)
sigma8=-(Mbroot/Ixx)*(y8-ycg)
sigma9=-(Mbroot/Ixx)*(y9-ycg)

sigma=[sigma1 sigma2 sigma3 sigma4 sigma5 sigma6 sigma7 ...
    sigma8 sigma9]
sigmamax=max(abs(sigma))

tau1=abs(q1/t12)
```

```
tau2=abs(q2/t23)
tau3=abs(q3/t34)
tau4=abs(q4/t45)
tau5=abs(q5/t56)
tau6=abs(q6/t67)
tau7=abs(q7/t78)
tau8=abs(q8/t89)
tau9=abs(q9/t91)
tau10=abs(q10/t93)
tau11=abs(q11/t84)

tau=[tau1 tau2 tau3 tau4 tau5 tau6 tau7 tau8 tau9 tau10 ...
    tau11]
taumax=max(abs(tau))

MSsigma1=(((sigmamaxskin*0.8)/abs(sigma1))-1)*100
MSsigma2=((sigmamaxskin/sigma2)-1)*100
MSsigma3=((sigmamaxspar/sigma3)-1)*100
MSsigma4=((sigmamaxspar/sigma4)-1)*100
MSsigma5=((sigmamaxskin/sigma5)-1)*100
MSsigma6=((sigmamaxskin/sigma6)-1)*100
MSsigma7=(((sigmamaxskin*0.8)/abs(sigma7))-1)*100
MSsigma8=(((sigmamaxspar*0.8)/abs(sigma8))-1)*100
MSsigma9=(((sigmamaxspar*0.8)/abs(sigma9))-1)*100

MStau1=((taumaxskin/tau1)-1)*100
MStau2=((taumaxskin/tau2)-1)*100
MStau3=((taumaxskin/tau3)-1)*100
MStau4=((taumaxskin/tau4)-1)*100
MStau5=((taumaxskin/tau5)-1)*100
MStau6=((taumaxskin/tau6)-1)*100
MStau7=((taumaxskin/tau7)-1)*100
MStau8=((taumaxskin/tau8)-1)*100
MStau9=((taumaxskin/tau9)-1)*100
MStau10=((taumaxskin/tau10)-1)*100
MStau11=((taumaxskin/tau11)-1)*100


% RIB SECTION 6 %

trib=3
cm=360

Tan=q1*42.18+q9*8.20
Man=-q1*42.18*54.5-q9*8.20*(50.47-(8.20/2))

Tap=q1*42.18+q9*8.20+q10*L93
Map=-q1*42.18*54.5-q9*8.20*(50.47-(8.20/2))

Px9=Map/L93
```

```
286 Px3=Map/L93
287
288 beta9=2.56*pi/180
289 tb9=tan(beta9)
290 beta3=0
291 tb3=tan(beta3)
292
293 Py9=Px9*tb9
294 Py3=Px3*tb3
295
296 P9=sqrt(Px9^2+Py9^2)
297 P3=sqrt(Px3^2+Py3^2)
298
299 Ar9=(L93*trib)/2
300 Ar3=(L93*trib)/2
301
302 sigmar9=P9/Ar9
303 sigmar3=P3/Ar3
304 MSsigmar9=(((sigmamaxrib6*0.8)/abs(sigmar9))-1)*100
305 MSsigmar3=(((sigmamaxrib6)/abs(sigmar3))-1)*100
306
307 qan=(Tan-Py9-Py3)/L93
308 qap=(Tap-Py9-Py3)/L93
309
310 taua=max(abs(qan),abs(qap))/trib
311 MStaua=((taumaxrib6/taua)-1)*100
312
313 Tbn=q1*42.18+q9*8.20+q10*L93-q3*1.06
314 Mbn=-q1*42.18*(54.5+25)-q9*8.20*(50.47-(8.20/2))-q8*25*...
315     49.68-q10*50.47*25
316
317 Tbp=q1*42.18+q9*8.20+q10*L93-q3*1.06-q11*L84
318 Mbp=-q1*42.18*(54.5+25)-q9*8.20*(50.47-(8.20/2))-q8*25*...
319     49.68-q10*50.47*25
320
321 Px8=Mbp/L84
322 Px4=Mbp/L84
323
324 beta8=1.82*pi/180
325 tb8=tan(beta8)
326 beta4=2.94*pi/180
327 tb4=tan(beta4)
328
329 Py8=Px8*tb8
330 Py4=Px4*tb4
331
332 P8=sqrt(Px8^2+Py8^2)
333 P4=sqrt(Px4^2+Py4^2)
334
335 Ar8=(L84*trib)/2
```

```
Ar4=(L84*trib)/2

sigmar8=P8/Ar8
sigmar4=P4/Ar4
MSsigmar8=(((sigmamaxrib6*0.8)/abs(sigmar8))-1)*100
MSsigmar4=(((sigmamaxrib6)/abs(sigmar4))-1)*100

qbn=(Tbn-Py8-Py4)/L84
qbp=(Tbp-Py8-Py4)/L84

taub=max(abs(qbn),abs(qbp))/trib
MStaub=((taumaxrib6/taub)-1)*100
```

A.3.3 Matlab script for the verification of the junction of the wing

```
clear all
clc
set(0,'defaulttextinterpreter','none')


% DATA %

Troot=1963.08
Mbroot=2264040
Mtroot=-130271
ff=1.2
dpins=198
droots=130
PM61=((-ff*Mtroot)/dpins)+Troot
PM62=((ff*Mtroot)/dpins)+Troot
PM10=(ff*Mbroot/droots)

dM6=6
dM10=10
t=3.3
ttufnol=15
bM61=32.18
xM61=16.87
bM62=30
xM62=15.55
bM10=21.50
xM10=10.18

sigmamax=120   % Interglass 92149/Epoxy %
taumax=25.1   % Interglass 92149/Epoxy %
sigmamaxtufnol=200   % Tufnol Kite Brand %
```

```
taumaxtufnol=105   % Tufnol Kite Brand %
taumaxsteel=517

% STRESS ON THE PINS %

tauM61pin=16*PM61/(6*pi*dM6^2)
MStauM61pin=((taumaxsteel/tauM61pin)-1)*100
tauM62pin=16*PM62/(6*pi*dM6^2)
MStauM62pin=((taumaxsteel/tauM62pin)-1)*100

tauM10pin=16*PM10/(6*pi*dM10^2)
MStauM10pin=((taumaxsteel/tauM10pin)-1)*100


% STRESS ON THE HOLES %

sigmaM61=PM61/((bM61-dM6)*t)
tauM61=PM61/(2*xM61*t)
MSsigmaM61=((sigmamax/sigmaM61)-1)*100
MStauM61=((taumax/tauM61)-1)*100

sigmaM62=PM62/((bM62-dM6)*t)
tauM62=PM62/(2*xM62*t)
MSsigmaM62=((sigmamax/sigmaM62)-1)*100
MStauM62=((taumax/tauM62)-1)*100

sigmaM10=PM10/((bM10-dM10)*ttufnol)
tauM10=PM10/(2*xM10*ttufnol)
MSsigmaM10=((sigmamaxtufnol/sigmaM10)-1)*100
MStauM10=((taumaxtufnol/tauM10)-1)*100
```

Bibliography

[1] Federal Aviation Administration (FAA), *Federal Aviation Regulations (FAR) Part 23*, United States of America (1965).

[2] Ente Nazionale Aviazione Civile (ENAC), *Standard RAI-V.EL, Standard di aeronavigabilità per velivoli elementari*, Italia (1999).

[3] M. Sadraey, *Aircraft performance analysis*, VDM Verlag Dr. Mueller (2008).

[4] C.D. Perkins, R.E. Hage, *Airplane performance stability and control*, John Wiley & Sons, Inc. (1949).

[5] D.P. Raymer, *Aircraft design: a conceptual approach*, AIAA (1992).

[6] J. Roskam, E. Lan, *Airplane aerodynamics and performance 9th ed.*, DARcorporation (1997).

[7] McDonnell Douglas Corporation, *USAF stability and control DATCOM*, United States of America (1977).

[8] R.C. Hibbeler, *Mechanics of materials 5th ed.*, Prentice Hall (1996).

[9] M.C.Y. Niu, *Composite airframe structures*, Conmilit Press (1988).

[10] D. Gay, S.V. Hoa, S.W. Tsai, *Composite materials*, C.R.C. Press (1994).

[11] S. Timoshenko, S. Woinowsky-Krieger, *Theory of plates and shells 2th ed.*, McGraw-Hill (1959).

[12] T.G. Gutowski, *Advanced composite manufacturing*, John Wiley & Sons, Inc. (1997).

[13] D.H. Middleton, *Composite materials in aircraft structures*, Longman Scientific & Technical (1990).

[14] General Aviation Aircraft Meeting and Exposition, *Composites: design and manufacturing for general aviation aircraft*, Society of Automotive Engineers, Inc. (1985).

[15] G. Janszen, *Tecnologie delle costruzioni aeronautiche*, lecture notes from the course Tecnologia delle Costruzioni Aerospaziali L, University of Bologna (2008).

[16] F. Persiani, G.M. Saggiani, V. Rossi, *Dispense di progetto di aeromobili*, lecture notes from the course Costruzioni Aeronautiche L, University of Bologna (2008).

[17] A. Airoldi, *Space structures*, lecture notes from the course Space Structures L, Polytechnic of Milan (2011).

[18] G. Ciampaglia, *Tecnologia dei materiali compositi aeronautici*, I.B.N. Editore (1990).

[19] http://www.wikipedia.com

[20] http://www.csir.co.za

[21] http://www.amtcomposites.co.za

Acknowledgements

Well, this is probably the most difficult part for me. It is my third graduation thesis, and I used to thank just who was really involved in the project, so far. Actually I think I'll do the same now. The only difference is that several people must be thanked, and this can be possible only if I didn't understand anything about the work I've done, or, maybe much more probable, the bloody work has been truly quite wide. So, in a random order, I must thank prof. Enrico Troiani for all his help on the actual work and its respective report, and yet he still stands me, the CSIR RGL John Monk for all his great experience, patience, collaboration and weird side for which he has seen something to hire me for the project. Steve Haselum, Alan Sutherland, John Morgan, Tim King and Pieter Rossouw, because they've been more friends than colleagues. Even if, eventually they helped me also as colleagues. Or as friends. Well, I don't know the difference anymore. But this seems a good thing. Neall Moore, Duncan Higgs and Hudivhamudzimu Ravele for the collaboration and the helpful time spent together for the manufacturing and to find out solution to make it in time (sorry guys, I know that it wasn't your normal rhythm, but that's mine). Many other people could be thanked about my experience at the CSIR, or widely, about my experience in South Africa. But this is not about the work. For some reasons, all my african experience was quite hard sometimes. Ok, I'll have very cool stories to tell my nephews, but... Who will read this few words, can probably read himself if he is someone that must be thanked. So, if you're reading this, and you think that you did something good, well, thanks. Otherwise, rewind.
Last but not least, obviously, myself.

Outside the lines, I want to thanks my father and my mother. Because everything was a consequence of the freedom and the hope that they have left me in my life.